Air Force Institute of Technology

AFIT Scholar

10-29-2001

Modeling Axisymmetric Optical Precision Piezoelectric Membranes

James W. Rogers Jr.

Follow this and additional works at: https://scholar.afit.edu/etd

Part of the Optics Commons, and the Structures and Materials Commons

Recommended Citation

Rogers, James W. Jr., "Modeling Axisymmetric Optical Precision Piezoelectric Membranes" (2001).
Theses and Dissertations. 4531.
https://scholar.afit.edu/etd/4531

MODELING AXISYMMETRIC OPTICAL PRECISION
PIEZOELECTRIC MEMBRANES

DISSERTATION

James W. Rogers Jr., Captain, USAF

AFIT/DS/ENY/01-02

DEPARTMENT OF THE AIR FORCE

AIR UNIVERSITY

AIR FORCE INSTITUTE OF TECHNOLOGY

Wright-Patterson Air Force Base, Ohio

APPROVED FOR PUBLIC RELEASE; DISTRIBUTION UNLIMITED

The views expressed in this dissertation are those of the author and do not reflect the official policy or position of the Department of Defense or the United States Government.

AFIT/DS/ENY/01-02

MODELING AXISYMMETRIC OPTICAL PRECISION
PIEZOELECTRIC MEMBRANES

DISSERTATION

Presented to the Faculty of the School of Engineering and Management

of the Air Force Institute of Technology

Air University

In Partial Fulfillment of the

Requirements for the Degree of

Doctor of Philosophy
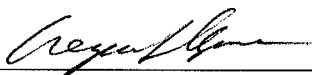
James W. Rogers Jr., B.S., M.E.

Captain, USAF

October 2001

MODELING AXISYMMETRIC OPTICAL PRECISION

PIEZOELECTRIC MEMBRANES
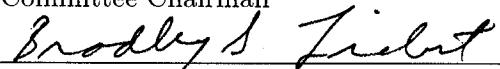
James W. Rogers Jr., B.S., M.E.

Captain, USAF

Approved:

_____   2 9 Oct 01

Major Gregory Agnes Ph.D.   Date
Committee Chairman
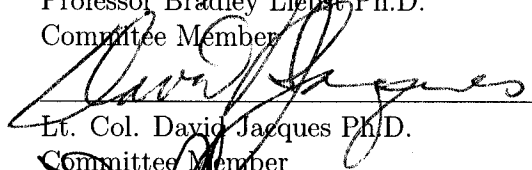
_____   29 OCT 01

Professor Bradley Liebst Ph.D.   Date
Committee Member
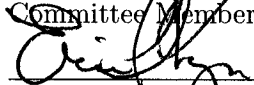
_____   29 OCT 01

Lt. Col. David Jacques Ph.D.   Date
Committee Member
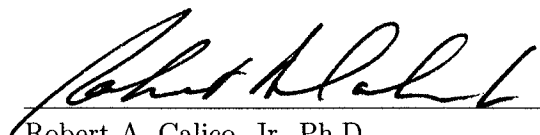
_____   29 OCT 01

Major Eric Magee Ph.D.   Date
Committee Member

Accepted:

_____   29 Oct 01

Robert A. Calico, Jr. Ph.D.   Date
Dean, Graduate School of Engineering and Management

Acknowledgements

James W. Rogers Jr.

Table of Contents

List of Figures

viii

List of Tables

AFIT/DS/ENY/01-02

Abstract

While inflatable technology is flight proven, the ability to control the shape of a flexible space structure to optical precision has yet to be demonstrated. A laminate of a piezoelectric polymeric material and a reflective structural material can deform a membrane optical surface; however, modeling of this system must be improved.

In this dissertation, the complete mechanics of laminated flexible beams and circular membranes are developed. Analytic solutions to the beam and axisymmetric membrane models are produced to provide insight into the behavior of these systems. Based on these results, a new mathematical methodology rooted in fundamental perturbation techniques was developed: The Method of Integral Multiple Scales (MIMS).

MIMS allows selectable precision when applied to the class of dynamic systems which can be represented through a Lagrangian. For illustration, this new method is first applied to a relatively simple linear beam. The method was able to integrate spatial and temporal multiple scales directly producing boundary layer results. Next, the method was fully realized through the finite element approach; the accuracy was shown to be three orders of magnitude greater than a standard finite element formulation. Finally, the finite element methodology was applied to the nonlinear beam and axisymmetric circular membrane and compared to analytical solutions. Various actuation patterns were analyzed to produce insight for future design decisions.

MODELING AXISYMMETRIC OPTICAL PRECISION PIEZOELECTRIC MEMBRANES

I. Introduction

Inflatable structures have been the focus of research and have proven themselves enabling technologies since the 1950's. In the past several years, research efforts in inflatable structures technology for space-based applications have increased (1). A substantial portion of these research efforts were and currently are directed at precision inflatable structures for use as primary support structure replacement or reflector/collector fabrication.

The first inflatable satellite was orbited in 1960 with the launch of NASA's ECHO I. Prior applications included inflatable truss structures, radar calibration spheres, and lenticular shaped reflectors (2). Due to weight and volume restrictions in the early space program, inflatables were considered an enabling solution. NASA's ECHO I and ECHO II provided early communications capabilities; Explorers IX and XIX were used for high altitude atmospheric studies, and PAGEOS I provided earth survey information. These inflatable structures ranged from 12 ft. in diameter and 34 lbs. (Explorer) to 135 ft. in diameter and 580 lbs. (ECHO II). The lack of industry experience, coupled with an overly conservative estimate of the meteoroid threat, resulted in inflatable space structures development all but vanishing (3).

Since the 1980's, a resurgence of inflatables technology occurred resulting in the deployment of the IN-STEP Inflatable Antenna Experiment (IAE) in 1996 (4). Although problems occurred during deployment, this experiment validated many technologies (5). The photographs in Figure 1.1 are of the IAE during deployment
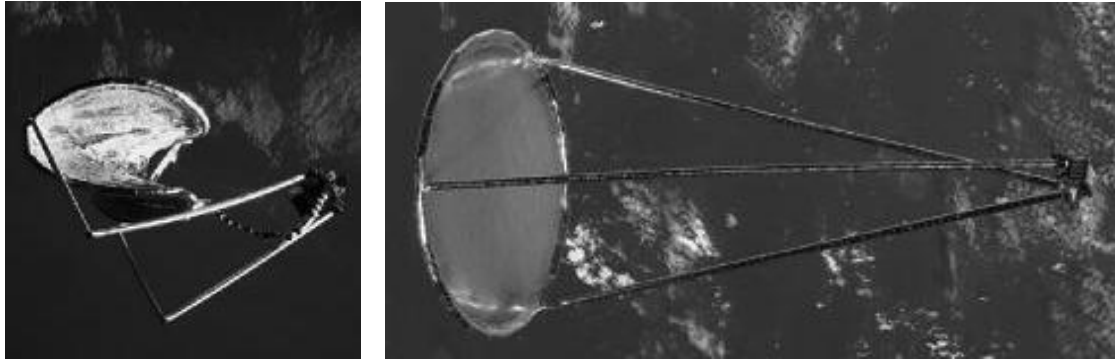
<div align="center">
(a)   (b)
</div>

Figure 1.1   The IN-STEP Spacecraft (a) Deployment (b) Fully Deployed

and in its final, fully deployed, configuration. Made of 7 micron thick Mylar[1] gores, the 14 meter inflatable reflector, including inflatable struts, was packaged inside an 80 in x 43 in x 21 in canister and deployed during the NASA space shuttle mission STS-77. The IAE was primarily a technical demonstration, but proved inflatable structures can be used as space structures.

Space inflatable applications can be organized into three general areas: 1. support structures, 2. reflectors/collectors, and 3. targets. Various organizations currently develop inflatable, deployable space structures (e.g., Aerospace Recovery Systems, Contraves, ILC Dover, L'Garde, SRS, Thiokol, and United Applied Technologies). As auxiliary structural supports, significant launch volume and weight can be saved.

Current designs for Synthetic Aperture Radar (SAR) (6, 7, 8) and deployable waveguides (7) use inflatable struts to provide the required shape. L'Garde's solution is to provide an inflatable frame using inflatable struts which provide the necessary geometry and tension for the membrane based devices. Figure 1.2 is an example of the SAR. An alternative solution selected for the MarS mission (7) is to encapsulate the planar radar array inside the inflatable structure (6). Its mission, to map the Martian surface, allows for non-rigidized struts. A similar mission to map the earth

---

[1]Trademark of E.I. duPont de Nemours & Co., Inc.

Figure 1.2   Synthetic Aperture Radar (L'Garde)

surface, LightSAR, has higher tolerances requiring rigidized struts. LightSAR uses an inflatable triangular truss structure, which contains both the radar antenna and the solar array.

Additional applications include interferometer and solar sail support structures. By creating a 50-100 meter class inflatable support structure, a system of 1 meter class apertures can be arranged for interferometric applications (8). Due to the necessary size imposed by solar sails, inflatables could provide the support structure making the mission tractable (7, 8). An inflatable structure provides an alternative to the mechanical sunshade, and is the preferred solution for the upcoming Next Generation Space Telescope (NGST) (2, 9).

Communications and surveillance missions seem to be natural candidates for inflatable structure given that a lenticular shape is easily attainable. Large-scale inflatable near-parabolic reflectors have been created to demonstrate various manufacturing capabilities (7, 10). The Advanced Radio Interferometry between Space and Earth (ARISE) project is currently in development (see Figure 1.3) (11, 12).
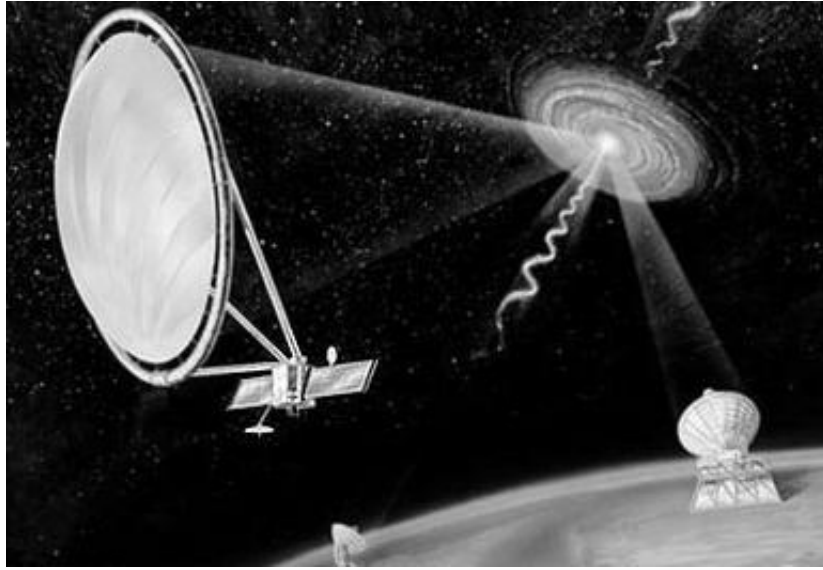
Figure 1.3   Advanced Radio Interferometry between Space and Earth (ARISE)

Using one or more 25 meter class radio telescopes in highly elliptical earth orbits, extremely high resolution of astronomical phenomena is possible. Optical wavelengths are also under consideration, but would require a significant increase in the accuracy of the parabolic reflector. An interesting combination uses the same reflector both as a solar concentrator as well as a communications antenna (7, 8). The current requirement for Radio-Isotope Thermal Generators (RTG) for outer solar system exploration missions could conceivably be satisfied by using large solar concentrators. The Power Antenna concept uses a lenticular shaped, parabolic inflatable reflector supported by an inflatable strut/torus structure. The solar energy is focused into an absorber for energy conversion. A beam splitter is used to separate the desired RF bands used for communications.

Current developments in advanced propulsion technologies also make use of inflatables. A flight experiment named Shooting Star (now cancelled) was designed around a Fresnel lens solar concentrator supported by an inflatable strut/torus structure (Figure 1.4) (13). Currently, the Solar Thermal Propulsion (STP) project is
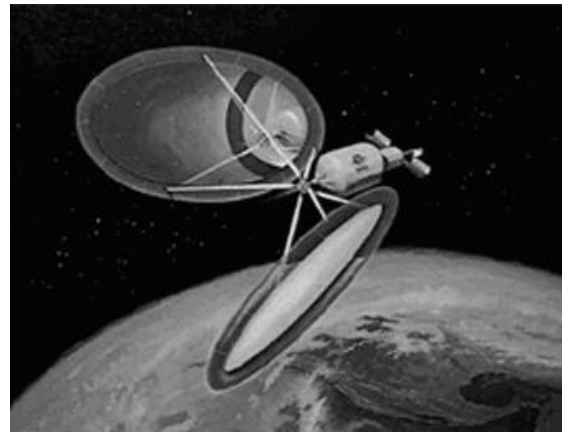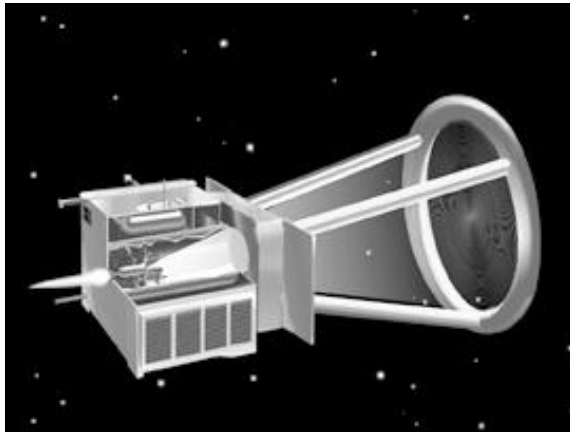
Figure 1.4   Shooting Star Spacecraft   Figure 1.5   Solar Orbit Transfer Vehicle

in development as a possible upper stage replacement. The Solar Orbit Transfer Vehicle (SOTV), shown in Figure 1.5, uses the developments of the STP program to provide economic benefit and provides support in all three reflector/concentrator categories (10). After using the reflectors during the orbital transfer phase as a high specific impulse propulsion source, the absorber is reconfigured for power generation and/or communications/surveillance support.

Space inflatable technology is also used for optical and RF targets. The Optical Calibration Sphere (OCSE) was designed, built, tested, and delivered in less than four months, illustrating the maturing of the technology (14). The Exoatmospheric Target/Decoy is a complex dodecahedron radar reflector (14). This 6 ft reflector was packaged in a 0.5 cubic ft. container.

Current research covers virtually all aspects of inflatable technology in support of the various application opportunities. From materials research to new systems design approaches, inflatables are challenging all technical fields. Space-based optics, however, drives the required precision beyond the limits currently available using inflatable technology.

1.1   Space-Based Optics

Reconnaissance and energy transmission missions increasingly demand larger reflectors. The Hubble telescope contains the largest optical reflector launched into space to date. Due to current launch vehicle constraints, larger, single-piece, rigid, space-based reflectors do not appear possible. One solution is to create the primary reflector by deploying a number of rigid subsections. This solution can increase the reflector size, but the ultimate size is quickly reached due to the weight and complexity of the overall system. An alternative solution might be an inflatable system, which can achieve very large reflector sizes compared to its pre-deployment storage volume.

A current effort seeks to create inflatable lenticular reflectors. Although these structures seem natural for reflectors and concentrators, the accuracy required for the surface at optical wavelengths (~ 600 nm) has yet to be attained (3). Pressurizing a uniform material in this configuration results in a near parabolic shape in which the 'nearness' is related to pressurization levels and initial pre-stress induced prior to inflation (15, 16). Although creating an optically accurate membrane reflector would provide a significant boost, additional problems must be considered. Manufacturing and material inaccuracies, always present, will provide significant localized errors which must be corrected. Optically precise membranes must be accurately created and maintained to provide the reflected wavefront necessary to satisfy mission requirements.

1.2   Optical Precision Membranes

The ability to create and operate optical quality membrane mirrors requires a number of technological advancements. Due to the inherent flexibility of a membrane surface, static mechanical actuation tends to produce only a localized effect (13). To correct the aberrations in the reflected wavefront from the membrane mirror, a

1-6

method to globally manipulate the reflective surface must be derived. Additionally, the materials desired for the membrane mirror tend to be approximately 100 microns thick, while the total area of the reflected surface can measure over 60 square meters. A space structure with this aerial density is often referred to as a Gossamer structure. From the large scale of such structural concepts to the extremely small wavelengths of interest in an optical system, there are many areas rich with research topics. The research presented herein explores the use of piezoelectric materials to manipulate the surface deflections of the membrane, creating the desired wavefront when reflected by the mirror.

Wagner conducted preliminary work in support of this research effort creating a laser-based surface measurement system capable of evaluating the surface at sub-wavelength accuracies (17). Using an interferometer, the fringe patterns were observed for wavefront distortions. In addition, an Adaptive Optics Associates (AOA) Wavescope provided Shack-Hartman wavefront sensor measurements. Using the Wavescope, the test system directly measured the the Zernike coefficients of the reflected wavefront. Wagner created and measured surface accuracies of seven different Polyvinylidine Flouride (PVDF) actuated membrane mirrors. Actual surface correction was not intended. While he proved the test system was adequate to measure the surface of a membrane mirror, he was unable to construct a satisfactory PVDF bonded membrane mirror. The bonding technique caused significant surface distortions (print-through) which dominated the error patterns. The fabricated mirrors produced significant surface movement when voltage was applied to the PVDF; hence, the results of this initial phase of the overall research program do provide confidence that such a device can be created.

1.3   Research Goals and Scope

The research herein presents a method to analyze piezothermoelastic laminated membranes to optical precision. The current computational analysis tools available

to an analyst are either limited to homogenous materials, unable to adequately model a laminated membrane, or fundamentally based on materials of significantly higher stiffness, resulting is significant error. A finite element approach is developed which provides extreme precision, when compared to standard tools available. This new methodology, based on the Method of Integral Multiple Scales, first introduced herein, can provide asymptotic solutions for systems containing 'small' parameters. The validation of this methodology is presented through comparison of known solutions.

Chapter II presents a broad background illustrating the technical challenges addressed with this research. Chapter III presents the introductory concepts through a thorough development of an analytical solution of a piezothermoelastic beam-string representing a cross-section of an electrically actuated inflatable structural element. The localized nature of the applied forces are clearly exhibited as small boundary layer effects. Chapter IV further expands this development to a circular plate-membrane model. The affects actuating forces have on a reflected wavefront are discussed. Chapter V develops finite element models using asymptotic expansion theory. The Method of Integral Multiple Scales (MIMS) is introduced, and used to formulate the finite element method. A linear beam is modelled to illustrate this novel method. Chapter VI expands this method into the solution of nonlinear problems. MIMS is applied to the nonlinear beam and circular plate problems presented earlier and compared to the analytical solutions presented in the previous chapters.

1.4   Contributions

The contributions within this dissertation are outlined here for clarity. The author has conducted a thorough literature review and is unaware of any previously published material relating to these subjects.

1. Chapters III and IV introduce beam-string and plate-membrane analytical solutions for piezothermoelastic laminates.

    (a) Energy-based equation of motion derivations produce the nonlinear equations governing the behavior of piezothermoelelastic laminated beam-strings and circular plate-membranes.

    (b) The methodology introduced integrates three previously independent methods to produce the desired solutions.

    (c) Static and dynamic solutions for the laminated beam-string and an axisymmetric plate-membrane are produced.

2. The Method of Integral Multiple Scales (MIMS) introduced in Chapter V presents a new perturbation method for solving Lagrangian-based systems.

    (a) An analytical solution is provided to illustrate the basic mechanics of the method for both spatial and temproal scales.

    (b) A finite element methodology, based on MIMS, is developed.

        i. Parametric asymptotic shape functions providing boundary layer capabilities are introduced.

        ii. Static and dynamic solution methods are developed.

3. Nonlinear MIMS based finite element solutions of the piezothermoelastic laminates are presented in Chapter VI.

    (a) Static beam-string solutions illustrate the method's ability to model electrode distribution patterns.

    (b) Static and dynamic axisymmetric optical membrane solutions are produced illustrating the capability of the piezo-laminate to modify a reflected wavefront.

Through the development of these contributions, a comprehensive set of analytical and numerical solutions are presented to aid in the further development of

inflatable optical reflectors. The introduction of MIMS promises far-reaching impact as a solution methodology for many areas beyond the specific application herein.

II. Background

Creation of a space-based inflatable optical reflector is beyond current technology. Advancements are necessary in many areas, including improved material properties, initial static shaping, and dynamic control of such compliant structures. This chapter outlines the pertinent published information related to the research goals discussed in Chapter I.

2.1 Inflatable Structures

Currently, space-based inflatable structures are constructed from polymeric thin films. The IAE design team chose Mylar. While primarily a technology demonstration, on-orbit post-deployment surface accuracy of the IAE was measured at 2mm rms (5). An RF (28 GHz) reflector surface requires a surface accuracy of approximately 0.58 mm rms (3). An optical reflector would require significantly higher precision (¡ 0.05 mm rms). Using interferometry methods, various materials were found to have significant thickness variations (18). UPILEX, with improved thin-film material qualities, has been considered in an attempt to increase surface accuracy. The need for further improvements led to development of improved materials (e.g., CP-1 and CP-2 have been developed by NASA and SRS Technologies).

The compliance of an inflatable structure can not satisfy many mission's requirements. Many materials, however, can remain flexible prior to deployment, and be rigidized on-orbit. May, et al. compiled space cured composite structure information through a literature search (19). Rigidization techniques included Plasticizer or Solvent Boil-off, Vapor Reactions and/or Catalysis, Ultraviolet Radiation, Thermal Cure, Elastic Memory, and Anaerobic Curing. The ability to strengthen the structure post-deployment will significantly improve inflatable structure mission requirements compliance.

Research underway at the Directed Energy Directorate of the Air Force Research Laboratory (AFRL/DE) seeks to create an inflatable optical telescope (20). A comprehensive review has produced both qualitative and quantitative measures at optical tolerances to evaluate a material's appropriateness (21). Membrane material thickness and shape variation categories were defined. Their effects on the reflected wavefront were described as well as resulting prestress effects. These categories can be used to evaluate prospective material candidates.

2.2   Environmental Effects

An understanding of the environmental effects on thin-film, polymeric materials is critical to the life cycle of any inflatable structure. Atmospheric conditions are not only important prior to deployment, but can affect the structure on-orbit. Gierow, et al. studied temperature and humidity effects relating to system pressure and thickness (22). Analysis presented indicates film thickness and pressurization levels are the most critical parameters and should dominate optimal design methodology of an inflatable space structure.

Post-deployment mission requirements will include dynamic activity such as slewing and repositioning. These maneuvers will impart significant vibrations through the structure. Dynamic behavior of inflatables continues to be a rich research environment. Non-rigidized inflatable beam analysis by Main has produced significant insight into the nature of this behavior (23). Of interest were determination of damping mechanisms present, practical model development and illustration of ground-test vs. on-orbit behavior discrepancies. Results indicated viscous damping was independent of pressurization, but the resulting stresses due to pressurization did affect strain-rate damping. The Bernoulli-Euler model used defined viscous damping as the effect due to the beam moving through the medium, and strain-rate damping resulting from the internal damping mechanisms within the beam. This model was shown to be adequate at lower natural frequencies. Through testing, gravity was shown

to have a significant effect on system damping. As gravity increased, wrinkling also increased, resulting in a drop in system damping.

The dynamic nature of a mission and the environment often demands a control mechanism, whether active or passive to either satisfy design requirements or relax design parameters. Structural vibrations, causing reflector surface movement, results in dynamic wavefront variations which must be corrected either real-time or through post-processing. Adaptive optics techniques could be implemented to correct these wavefront aberrations.

2.3   Post-Deployment Correction

Significant effort is being spent towards creating the perfect near-net reflector shape. Even if this end is met, disturbances will require some method of correction. Since correction is required through the life of the structure, it should be integrated earlier in the design process as a method to correct deviations present at any time. This could result in the relaxation of certain design parameters early in the design process. Adaptive optics could correct wavefront distortions received from an imperfect reflector, and the structure could be manipulated to improve the surface accuracy.

2.3.1   Adaptive Optics.   Adaptive optics techniques can be used to manipulate the reflected wavefront, often correcting the aberrations present. One very promising technique is Real-Time Holography (RTH) which promises the ability to correct hundreds of waves of aberrations (24, 25). Coupled with a coarse correction scheme used to actually deform the mirror, a viable imaging system may be possible. The RTH technique uses a surface interferogram projected onto a real-time optical recording medium, which is used to generate a diffraction hologram. This research was not concerned with the actual application of the RTH technique. It is only introduced to illustrate the true accuracy requirement for a membrane mirror in order

www.manaraa.com

to produce a usable optical system. This addition to an inflatable reflector system allows for a less precise surface. A reflector designed to precision levels satisfying RF mission requirements could conceivably satisfy optical mission requirements. While an RF reflector requires much lower precision than an optical reflector, significant technology advancements are still necessary.

As previously discussed, a large effort has been underway to create an optical reflector by improving design and manufacturing processes as well as material properties. Regardless of the actual shape produced, system vibrations will cause wavefront distortions which ultimately must be compensated. This will require some method of control. An inflatable system, however, cannot use many standard methods of control due to its extremely high compliance. Any point force or moment applied will cause localized buckling (or wrinkling) reducing the force's effectiveness. Distributed forcing is therefore considered an option to apply control.

2.3.2   *Active Structural Control.*   An example of active structural control applied to inflatable structures was presented by Bailey's review of a program to develop piezoelectric actuator distribution technology (26). Using a piezoelectric polymer material polyvinylidine floride (PVDF), a simulated large flexible space structure was tested. The low-authority actuators using PVDF were found to be unsatisfactory for large disturbances (e.g. slewing or docking maneuvers) in short time periods. For low disturbance levels, materials such as PVDF can provide increased system damping. While the low-authority of this material is unsatisfactory for overall structural control, it's compliance, low mass and low volume, make it an attractive option worthy of further research.

PVDF has been applied to a laminar glass plate and evaluated for its shaping effectiveness (27). Interferograpic images were evaluated and frequency characteristics measured as voltage levels were applied to plates with shaped PVDF patches applied.

2-4

Utku discussed piezo-film or shape memory alloy actuators as a mechanism to manipulate the shape of low-frequency antenna reflectors (28). Linearized thin shell and membrane theories were used assuming deviations are on the order of the surface thickness. Zernike decomposition was used to provide a measure of effective surface distortion. Appendix A presents a short introduction to Zernike modes and how they relate to membrane vibration modes.

Membrane mirror wavefront correction using laminated PVDF was studied by Xin (29). Experimental results from a study of electrode distribution patterns across a circular piezoelectric laminated membrane mirror indicated such a method did modify the wavefront. By using Zernike decomposition, Xin was able to directly relate structural deformation to standard optical wavefront modes providing good optical wavefront comparisons.

Bishop used a genetic algorithm to successfully correct for defects in an inflated flat membrane (30). Using distributed edge springs, surface distortion was reduced.

Grossman introduced a tension-resisting element along the major axis of an elliptical rim (31). The result is a reduction of loads and deformation in the rim structure and therefore improves its ability to provide adequate support for the reflector.

Moore evaluated catenary suspension of a reflector using a tunable catenary concept (32). Uniform tensioning of the catenary supports significantly improved the reflector shape, while individual load optimization produced only modest improvements.

Wilkes has presented two methods of shape manipulation (33). Edge tension is shown to have limited effect as f/D decreases. The f/D is a ratio of the focal distance to the reflector diameter: as f/D decreases, the curvature increases. A novel idea of using a plunger to translate the center of the membrane along the optical axis dramatically improves the reflector shape.

Greschik presented a comprehensive parametric study involving material irregularities, thermal loads, boundary layer effects and wrinkling (34). Reflectors became increasingly sensitive to design approximations and physical perturbations as the f/D increases (shallow dishes and higher pressures).

2.4   Research Focus

The research presented herein focuses on the effective modeling of an axisymmetric piezothermoelastic laminated membrane to optical precision. The author is not aware of any published information which adequately presents a modeling capability providing the precision demanded by the application of concern. Through a mechanics-based development, the fundamental behavior of these materials are modelled. Inflatable optical reflectors, possessing such extremely small thickness to area ratios, can not efficiently be treated as standard thin plates or shells. To better develop the necessary insights, initial development of a beam model is presented.

2.4.1   Nonlinear Beams.   Beam theory often provides the insight necessary to tackle more complicated problems in multiple dimensions. Eringen provides the fundamental theory on the classical vibration of bars assuming the deflection is small (35). The boundaries are allowed to move in the axial direction, and deflection is inextensional . The equations of motion were derived from dynamic equilibrium and perturbation techniques were introduced as a method to solve the resultant coupled set of equations. The resultant methodology is useful in analyzing small amplitude beam deflections.

Aravamudan presents large amplitude effects on inextensional and extensional vibrations of slender uniform elastic beams (36). Equations of motion were derived from basic energy principles assuming large amplitudes, but linear elasticity, shear deformation and rotatory inertia were ignored, plane sections remain plane and normal to the beam centerline, and damping and hysteresis is ignored. Perturbation

techniques were again used to solve the resultant system. Beam stability was analyzed as well as a comparison to numerical predictions.

Crespo da Silva studied non-linear, non-planar motion of beams (37, 38). Equations of motion with order-three nonlinearities suitable for perturbation analysis were developed from energy principles using Hamilton's extended principle assuming an inextensional beam and neglecting shear deformation. Perturbation analysis was presented and a representative test case was discussed.

Nayfeh formulated the beam-string solution from elemental dynamic equilibrium, allowing the deformed beam planes to move from perpendicular but remain plane (39). A perturbation solution was presented using first-order expansions and transverse shear and rotatory inertia were taken into account.

2.4.2 Nonlinear Plates/Membranes.
With the basic understanding of beam behavior and the methodologies available to solve such one-dimensional formulations, the two-dimensional problem can be attacked. Steele presents a comprehensive review of the structural mechanics analysis of pressurized membrane optical performance (40). Asymptotic solutions to the developed shell equations are presented and discussed. Asymmetric results of edge effects are shown to approach axisymmetric results due to the large diameter to thickness ratio.

With highly compliant two dimensional shapes comes the additional problem of wrinkling. Mikulas preformed early elastic analysis of deeply curved, axisymmetric, partly wrinkled membranes formed from an initially flat sheet (41). Wrinkling regions were predicted and experimentation validated the theory. More recently, Kang studied anisotropic and isotropic materials, allowing finite rotations (42). A coordinate system aligned with the wrinkling pattern allowed for a simple and efficient Lagrangian-based finite element analysis methodology.

Wilkes presented limitations of edge tension manipulation with regards to pressurized membrane shaping (43). Based on Hencky-Campbell membrane theory, the membrane was modelled and compared to experimental results.

Marker discussed the nature of the "W-Profile Error" or "Spherical Aberration" inherent with initially flat pressurized membranes (44). He clearly shows why removal of this phenomenon is necessary for optical reflectors, and how this error increases with reduction of f/D, or 'deepness' of surface.

Jenkins used analytical predictions based on Von-Kármán axisymmetric plate equations to define surface deviations (45). Nonlinear computational analysis is implemented using the finite element analysis tool ABAQUS. Manipulation of the boundary (rim) of a pressurized membrane was evaluated as a mechanism for shape correction. The inherent "W-profile error" present in inflated circular membranes was altered through discrete boundary displacements. Active methods including electrostatic, thermal, and boundary control were discussed as possible shape manipulation techniques.

Greschik presents a case study of different assumptions towards shape prediction of pressurized membranes (46). Both initially flat and doubly curved membranes with f/D ratios ranging from 0.25 to 10.0 and pressurization ranges resulting in skin stresses from 125 psi through 1000 psi at the center were presented. Ignoring wrinkling was shown to significantly increase errors in shallow dishes with low pressurization levels. All analysis focused on the RF frequency range precision level, but qualitative extension to higher frequencies is included.

Due to the limitations present in analytical solutions, significant effort has resulted in a couple specialized finite element analysis tools to be used in the design of inflatable structures. Palisoc described FAIM: Finite Element Analysis of Inflatable Membranes computer code (47). This is a family of utility programs for the design and analysis of inflatable membrane structures. Its capabilities include geometric and material nonlinearities as well as static and modal dynamic analysis. Available

forcing methods are follower pressure, body-loading (G-forces), point-loading, and nodal or thermal loads. This utility was developed by L'Garde Inc. to aid in the development of their space-based RF reflector designs. Greschik realized FAIM is not adequate for optical system accuracies (48). The fundamental pressurized membrane model cited by virtually all researchers was the foundation work presented by Hencky (49). The power series approximation method, proved far too limiting in the evaluation of reflectors used at optical wavelengths, and needed to be improved. A solution method was needed which would satisfy a $\lambda/20$ precision, where λ is the wavelength in question. Based on this analysis, a new software package was developed: AM (Axisymmetric Membrane) (16). This package includes geometric nonlinearities and wrinkling predictions. By modeling the axial displacements present in a pressurized membrane shape, an improvement to FAIM was claimed. This improvement is more prevalent as the frequency of reflected energy is increased. As with FAIM, this system was used to solve the *inverse problem*, or calculating the initial shape necessary to produce the correct pressurized surface.

Using both codes, FAIM and AM, Palisoc analyzed state-of-the-art membrane reflector designs (3). Initially flat and curved surfaces were discussed. FAIM and AM codes were tested against each other and experimentally validated. Analysis indicated inflatable reflectors capable of supporting lower wavelength missions are possible today, but significant improvements were required to satisfy optical telescope parameters.

2.4.3 *Finite Element Modeling.*

The use of specialized finite element codes were necessary due to the inherent modeling problems in inflatable membranes. As the thickness decreases, either the material's extremely low bending stiffness causes numerical locking problems, or the number of degrees of freedom grow so large as to make a solution inaccurate or even unattainable. What is desirable is a finite element solution method which can overcome these standard limitations, while maintaining the nonlinear nature of the mechanics modelled.

2-9

Mohan presented a geometrically nonlinear finite element formulation for static and dynamic analysis (50). Results correlated favorably with ABAQUS model predictions, but the calculations were not computationally expensive due to the simplicity of the formulation.

Karnaukhov discussed a finite element method for a material with *thermoelectroviscoelastic (TEVE)* properties (51). Thermal, electrical and mechanical equations of equilibrium were presented and linearized for use in solving non-linear problems. A method to determine damping and dynamic coupling coefficients was also derived. Elsami developed a finite element procedure for thermoelastic shells of elasticity under thermal shock (52). Integrated piezoelectric material modeling must allow simultaneous modeling of all three properties.

2.4.3.1 *Piezoelectric Materials.*

Piezoelectric materials hold interesting properties which may provide an answer for some of the problems currently facing the designers of inflatable space structures. Two brothers, Pierre and Jacques Curie, are credited with the discovery in 1880 that some materials will generate a change in electric field when pressure is applied. Hankel further refined the research and termed the effect 'piezoelectricity,' recognizing the different affects thermal and mechanical deformation had on these materials (53). When a mechanical force is applied to a piezoelectric material, and an electric charge is generated, this in known as the *direct piezoelectric effect.* These materials will also produce a mechanical force when an electrical charge is applied. This effect is known as the *converse piezoelectric effect* (54). While much research has been accomplished with regards to using the direct piezoelectric effect for dynamic behavior identification, this research concentrates only on the converse piezoelectric effect, as the material was used primarily as an actuation device.

The linear constitutive equations for piezothermoelasticity can be defined as:

$$\{T\} = [c]\{S\} - [e]^T\{E\} - \{\lambda\}\Delta t_p, \tag{2.1}$$

$$\{D\} = [e]\{S\} - [\epsilon]\{E\} - \{p\}\Delta t_p, \tag{2.2}$$

$$\{\lambda\} = [s]^{-1}\{\gamma\}, \tag{2.3}$$

where $\{T\}$ is the stress vector, $[c]$ is the elastic moduli matrix, $[e]$ is the piezoelectric constant matrix, $\{E\}$ is the electric field vector, Δt_p is the temperature change, $\{D\}$ is the electric displacement vector, $\{S\}$ is the mechanical strain vector, $[\epsilon]$ is the dielectric constant matrix, $\{p\}$ is the pyroelectric constant, $[s]$ is the elastic compliance matrix, and $\{\gamma\}$ is the coefficient of thermal expansion.

The coefficients contained within $[c]$, $[e]$, $[\epsilon]$, $\{p\}$, $[s]$, and $\{\gamma\}$ have been experimentally attained for the various materials which have been observed to exhibit the piezoelectric phenomena. Early research concentrated on those materials found in nature such as crystals. Later, polymer-based materials were created which exhibited these piezoelectric qualities. PVDF is such a material.

There are various class definitions covering all discovered piezoelectric materials. Whether crystal or polymer in nature, the molecular makeup of the substance is categorized, sometimes allowing simplification of the equations used in analysis. PVDF (or PVF_2) is classified as a class C_{6v} piezoelectric material, where the elastic moduli matrix is of the form:

$$[c_{ij}] = \begin{bmatrix} c_{11} & c_{12} & c_{13} & 0 & 0 & 0 \\ c_{12} & c_{11} & c_{13} & 0 & 0 & 0 \\ c_{13} & c_{13} & c_{33} & 0 & 0 & 0 \\ 0 & 0 & 0 & c_{44} & 0 & 0 \\ 0 & 0 & 0 & 0 & c_{44} & 0 \\ 0 & 0 & 0 & 0 & 0 & c_{66} \end{bmatrix} \tag{2.4}$$

2-11

$$c_{11} = \frac{E}{1 - \nu^2}$$

$$c_{12} = \frac{E\nu}{1 - \nu^2}$$

$$c_{66} = 1/2 \left(c_{11} - c_{12} \right)$$

$$= \frac{E}{2 \left(1 + \nu \right)}$$

where E is Young's modulus and ν is Poisson's ratio. Note, for thin shells, c_{13}, c_{33}, and c_{44} are usually neglected since through-the-thickness stress can usually be neglected. The piezoelectric constant, $[e]$, and the dielectric constant, $[\epsilon]$, are defined as:

$$[e_{ij}] = \begin{bmatrix} 0 & 0 & 0 & 0 & e_{15} & 0 \\ 0 & 0 & 0 & e_{15} & 0 & 0 \\ e_{13} & e_{13} & e_{33} & 0 & 0 & 0 \end{bmatrix}, \tag{2.5}$$

$$[\epsilon_{ij}] = \begin{bmatrix} \epsilon_{11} & 0 & 0 \\ 0 & \epsilon_{11} & 0 \\ 0 & 0 & \epsilon_{33} \end{bmatrix}. \tag{2.6}$$

Equations 2.4-2.6, used in Equations 2.1-2.3 can be used as the basic constitutive equations for the development of some preliminary finite element modeling of a piezoelectic laminated membrane mirror.

2.4.3.2 Piezoelectric Laminates.

The previous finite element methods assumed isotropic elastic properties, and must be modified if applied to a piezoelectric laminate which may exist in an inflatable space structure. Salama showed that surface accuracy of on-orbit inflatable antennas could be increased using piezo-film (55). Shape correction was modelled and experimentally assessed for both inflated tubes and pressurized membranes. Analysis relied on nonlinear NASTRAN procedures and Hencky assumptions. Since NASTRAN provides only thermal and elastic degrees of freedom, the piezoelectric effects were modelled as thermal effects.

2-12

Piezo-actuation was implemented through edge condition, in-plane membrane strain, and moment generation application. Each mechanism is discussed independently, along with its effectiveness. Non-piezo design testing indicated model predictions were approximately 10% too stiff, attributed to poor knowledge of Mylar's elastic modulus. The piezo-actuated designs proved far too error-prone to yield quantitative results, but qualitative indications imply shape control of these structures was possible using piezo-films. These errors are again attributed to the poorly known material properties.

Dökmeci presented a more complete dynamic theory for problems involving coated laminae in which there exists electrical, thermal and mechanical coupling. Each layer is assumed to to have uniform thickness, curvature and electromechanical properties. Three-dimensional linear fundamental equations of thermopiezoelectricity are presented and applied through Mindlin's variational theorem to develop a system of equations: Macroscopic stress equations of motion; macroscopic charge equations of electrostatics; macroscopic equations of heat conduction; mechanical, electrical and thermal boundary conditions as well as initial conditions.

Sun presented a piezoelectric composite laminate theory (56). Thickness was assumed to remain constant, in-plane displacements were assumed linear in nature, the constitutive relations were linear and linear finite deformation was assumed.

Tzou discussed linear finite element theory applied to a thin plate with integrated distributed piezoelectric sensor/actuators (54, 57). A new piezoelectric finite element was developed and integrated into the overall plate model. Vibration control was studied through the implementation of different control strategies. Temperature effects, while commented upon, were not included.

Tzou also presented thorough mechanics development of a distributed piezoelectric thick shell system (58, 59). Thermal effects, transverse shear and rotatory inertia were included, and simplifications were presented for use in thin shells and plates. Further development resulted in a geometrically non-linear piezothermoelas-

2-13

tic laminate theory (60). Constitutive relations include mechanical, electrical and thermal excitations. Non-linear system equations assuming large deformations were presented, but transverse shear deformation and rotatory inertia were not considered.

These theories, while complete and useful for their purposes, do not directly aid in the analysis of large inflatable optical membranes. They encounter numerical limitations identical to standard finite elements. Analytical solutions of some previously unsolvable systems have been found by applying perturbation theory. Any analytical solution to the non-linear problems previously referred to have made use of perturbation methods to arrive at a solution. The finite element solutions, however, have not.

2.4.3.3 *Variational-Asymptotic Theory.* The Variational-Asymptotic (VA) method merges these methodologies to arrive at solutions with greater efficiency. Berdichevsky's theory behind VA has been used to solve structural analysis problems (61). He applied this perturbation approach to a physically and geometrically non-linear theory of shells.

Cesnik applied the VA method to a composite beam (62, 63). A geometrically nonlinear theory for composite beams was developed. Using "shape functions" for through-the-thickness variations, a better approximation to the property variations within the beam is predicted. The results correlated well with known exact solutions.

Lee applied the VA method to a laminated plate (64). Using laminated plate theory, a two-dimensional theory is derived from general three-dimensional analysis. The "shape functions" again provide through-the-thickness variation approximation.

This research does not apply the VA method. But realizing the advantage perturbation techniques can have when applied to certain problems, a new mathematical approach, rooted in basic perturbation methods, is presented as another useful tool for the analyst. The Method of Integral Multiple Scales (MIMS), while providing valid analytical solutions, provides a solid mechanism for computational

solutions. Through the application of finite element derivation, nonlinear systems represented by their Lagrangian can be solved.

To develop this method, analytical solutions were developed. Initial insight is gained through the relatively simple beam-string in Chapter III. This one-dimensional system represents a cut-away of a non-linear optical membrane. A comprehensive mechanics derivation of the equations of motion governing the behavior of a beam constructed of electro-thermo-elastic materials results in a coupled nonlinear system which, through the creative application of perturbation techniques, can be solved.

Applying this methodology to the two dimensional system of interest, the derivation of the nonlinear equations of motion governing the laminated circular membrane are developed in Chapter IV . A simplified axisymmetric solution is created using the same methodology developed for the beam-string.

With the nonlinear analytic solutions in hand, MIMS is introduced in Chapter V. Through the presentation of a simple, linear example, MIMS is explained and argued. MIMS is then applied in Chapter VI to the nonlinear systems analyzed in Chapters III and IV. This method can then be used to improve analysis capabilities toward more effective inflatable space structure design.

III. Piezothermoelastic Beams

The design and implementation of an active membrane requires a new set of analytical tools. A finite element modeling capability providing thermal, electrical and mechanical evaluation would be of great utility. Analytical results using asymptotic methods will also be used to provide a necessary initial validation. The complexity involved in the analysis of a membrane can be better understood through the evaluation of a simpler one-dimensional beam model. This chapter represents the asymptotic solution for a piezoelectric laminated beam undergoing moderate deformation.

3.1 Laminated Piezothermoelastic Beam-String

A membrane mirror can be created using a membrane material, such as Upilex, metalized on one side to provide the necessary reflective surface. Applying a laminate of Polyvinylidine Flouride (PVDF) layers on the non-reflective side, an active membrane reflector can be constructed. PVDF is a piezoelectric polymer which strains when an electrical potential is applied across the thickness. In general this effect is orthotropic, resulting in much smaller effects in the transverse direction, but bidirectional PVDF is also available. Additionally, two layers of PVDF can be layered and, applying opposite electrical potential, used to produce a bimorph effect. As the two layers strain differently, curvature results. Applying a single layer of PVDF to Upilex and applying a time periodic electrical potential near the composite membrane's natural frequency produces significant deformation. Due to the directional properties of PVDF, a laminate of angled layers is being considered to provide desired controllability for a two-dimensional membrane surface. A one-dimensional 'beam' solution can provide valuable insights for the development of the more complex two-dimensional solution.
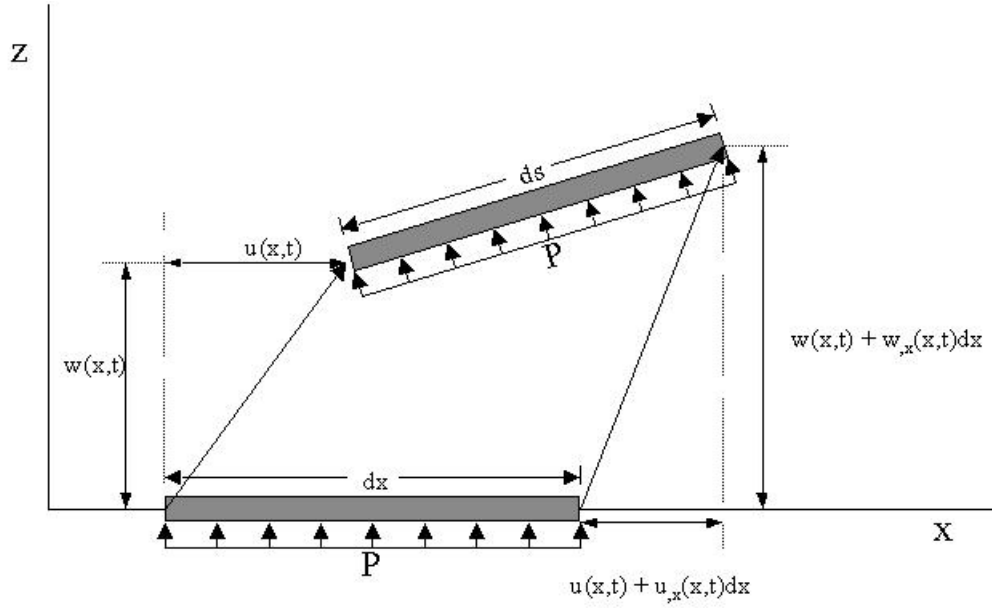
Figure 3.1   Pressurized Beam Deflection

3.2   Equations of Motion

To develop the necessary fundamental equations used in this analysis, an energy-based derivation is used. Refer to Figures 3.1 and 3.2 throughout the following derivation. The potential energy of an elastic beam can be defined over the volume ($\mathcal{V}$) using the strain energy representation (65):

$$\mathbb{V} = \int_{\mathcal{V}} \frac{1}{2}\{\epsilon\}^T\{\sigma\} - \{\epsilon\}^T\{\sigma_0\} + \{\epsilon_0\}^T\{\sigma\}d\mathcal{V} \\ + \frac{1}{2}K_0 w_{,x}(0,t)^2 + \frac{1}{2}K_L w_{,x}(L,t)^2 \tag{3.1}$$

with

$$\sigma = [E]\{\epsilon\} \qquad \sigma_0 = \frac{N_i}{A} \tag{3.2}$$

$$\epsilon = \frac{ds - dx}{dx} - zw_{,xx} \qquad \epsilon_0 = \alpha T + \frac{d_{31}V}{H} \tag{3.3}$$

where ϵ is strain in the beam, σ is stress equal to the strain multiplied by the material's modulus (E), ϵ_0 is prestrain resulting from thermal or piezoelectric actuation,

3-2

σ_0 is the prestress resulting from any initial axial load (N_i) across the cross-sectional area (A) and H is the laminate thickness. The addition of the spring constants (K_0 and K_L) at each end of the beam allows for variable boundary conditions used later in the analysis. Throughout this document, all variables after a comma in the subscript indicates the derivative with respect to that variable. Neglecting rotatory inertia, the beam's kinetic energy can be represented as

$$\mathbb{T} = \frac{1}{2} \int_{\mathcal{V}} \rho \left(u_{,t}^2 + w_{,t}^2 \right) d\mathcal{V}. \tag{3.4}$$

where ρ is the beam's density. The axial and transverse deflections are represented as u and w respectively. The system's non-conservative work is a result from the follower pressure force and can be approximated as

$$\mathbb{W}_{nc} = - \int_x P \left(w + u_{,x} w - w_{,x} u \right) dx. \tag{3.5}$$

To analyze a laminate, further development is required. Referring to Figure 3.2, each layer can have independent elastic, thermal, and piezoelectric properties. Assuming through-the-thickness strain is constant at any cross-section, the system can be collapsed into a one-dimensional integrodifferential system using

$$\rho A = \int_A \rho dA = \sum \int_{z_i} \rho_i dz \qquad N_z = \int_A \frac{N_i}{A} z dA = \sum \int_{z_i} \frac{N_i}{H} z dz$$

$$EA = \int_A E dA = \sum \int_{z_i} E_i dz \qquad N_0 = \int_A \frac{N_i}{A} dA = \sum \int_{z_i} \frac{N_i}{H} dz$$

$$EA_\epsilon = \int_A E \epsilon_0 dA = \sum \int_{z_i} E_i \epsilon_{0i} dz \qquad EA_{\epsilon z} = \int_A E \epsilon_0 z dA = \sum \int_{z_i} E_i \epsilon_{0i} z dz$$

$$EI = \int_A E z^2 dA = \sum \int_{z_i} E_i z^2 dz \qquad EA_z = \int_A E z dA = \sum \int_{z_i} E_i z dz \tag{3.6}$$

by integrating through each laminate layer i. Applying Hamilton's principle

$$\int_{t_1}^{t_2} \delta \mathbb{T} - \delta \mathbb{V} + \delta \mathbb{W}_{nc} dt = 0, \tag{3.7}$$
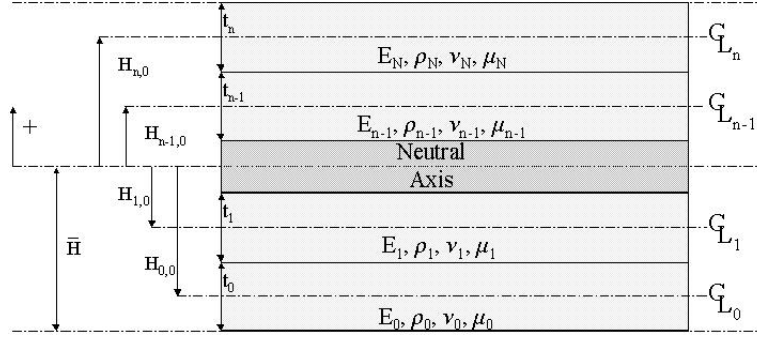
Figure 3.2   Piezoelectric Laminate Cross Section

where δ indicates variation, to this system, the following dimensional system is derived

$$\rho A u_{,tt} - EA u_{,xx} = \frac{1}{2}\left(EA - N\right)\frac{\partial}{\partial x}\left(w_{,x}^2 - 2u_{,x}w_{,x}^2\right) - 2P w_{,x}$$
$$- EA_z \frac{\partial}{\partial x}\left[w_{,xx}\left(1 - \frac{1}{2}w_{,x}^2 + u_{,x}w_{,x}^2\right)\right], \tag{3.8}$$

$$\rho A w_{,tt} - N w_{,xx} + EI w_{,xxxx} = \left(EA - N\right)\frac{\partial}{\partial x}\left(e w_{,x}\right) + P\left(1 - 2u_{,x}\right)$$
$$- EA_z \frac{\partial}{\partial x}\left[u_{,xx}\left(1 - \frac{1}{2}w_{,x}^2 + u_{,x}w_{,x}^2\right)\right], \tag{3.9}$$

$$e = u_{,x} - u_{,x}^2 + \frac{1}{2}w_{,x}^2, \tag{3.10}$$

$$N = N_i - EA_\epsilon, \tag{3.11}$$

with the following moment balance boundary conditions

$$EI w_{,xx} - N_z + EA_{\epsilon z} =$$
$$K_L w_{,x} + EA_z \left(u_{,x} + \frac{1}{2}w_{,x}^2 - \frac{1}{8}w_{,x}^4 - \frac{1}{2}u_{,x}w_{,x}^2 + \frac{1}{2}u_{,x}^2 w_{,x}^2\right)\bigg|_{x=L} \tag{3.12}$$

$$EI w_{,xx} - N_z + EA_{\epsilon z} =$$
$$- K_0 w_{,x} + EA_z \left(u_{,x} + \frac{1}{2}w_{,x}^2 - \frac{1}{8}w_{,x}^4 - \frac{1}{2}u_{,x}w_{,x}^2 + \frac{1}{2}u_{,x}^2 w_{,x}^2\right)\bigg|_{x=0}. \tag{3.13}$$

If all measurements are with respect to the original neutral axis of a symmetric laminate ($N_z, EA_z \to 0$), Equations 3.8 and 3.9 are the same as presented by Nayfeh (66) with additional pressure terms. Notice, the thermal and piezoelectric terms not only modify the axial tension within the beam (i.e. EA_ϵ), but also produce moments at the boundary (i.e. $EA_{\epsilon z}$).

To properly perform a perturbation analysis of this system, the system must be put in nondimensional form. The following nondimensional parameter scaling rules are used herein:

$$
\begin{aligned}
\hat{x} &= \frac{x}{L} & \hat{z} &= \frac{z}{L} \\
\hat{u} &= \frac{u}{L} & \hat{w} &= \frac{w}{L} \\
\hat{r}^2 &= \frac{EI}{L^2 EA}\eta & \hat{P} &= \frac{PL}{EA}\eta \\
\hat{N}_0 &= \frac{1}{\eta} & \hat{N}_z &= \frac{N_z}{LEA}\eta \\
\hat{EA}_z &= \frac{EA_z}{LEA}\eta & \hat{EA}_{\epsilon z} &= \frac{EA_{\epsilon z}}{LEA}\eta \\
\hat{K}_1 &= \frac{K_L}{LEA}\eta & \hat{K}_0 &= \frac{K_0}{LEA}\eta \\
\hat{EA}_\epsilon &= \frac{EA_\epsilon}{EA}\eta & \hat{t}^2 &= \frac{c_2^2}{L^2}t^2
\end{aligned}
\tag{3.14}
$$

where $\eta = \frac{c_1^2}{c_2^2}$, with $c_1 = \sqrt{\frac{EA}{\rho A}}$ and $c_2 = \sqrt{\frac{N_0}{\rho A}}$ being the longitudinal and transverse speeds of sound in the beam, to produce (eliminating the 'hats'):

$$
\begin{aligned}
u_{,tt} - \eta u_{,xx} = & -2\nu u_{,t} + \frac{1}{2}\left(\eta - 1 + EA_\epsilon\right)\frac{\partial}{\partial x}\left(w_{,x}^2 - 2u_{,x}w_{,x}^2\right) \\
& - 2Pw_{,x} - EA_z\frac{\partial}{\partial x}\left[w_{,xx}\left(1 - \frac{1}{2}w_{,x}^2 + u_{,x}w_{,x}^2\right)\right]
\end{aligned}
\tag{3.15}
$$

$$
\begin{aligned}
w_{,tt} - \left(1 - EA_\epsilon\right)w_{,xx} + r^2 w_{,xxxx} = & -2\mu w_{,t} + \left(\eta - 1 + EA_\epsilon\right)\frac{\partial}{\partial x}\left(ew_{,x}\right) \\
& + P\left(1 - 2u_{,x}\right) - EA_z\frac{\partial}{\partial x}\left[u_{,xx}\left(1 - \frac{1}{2}w_{,x}^2 + u_{,x}w_{,x}^2\right)\right]
\end{aligned}
\tag{3.16}
$$

3-5

$$e = u_{,x} - u_{,x}^2 + \frac{1}{2}w_{,x}^2 \tag{3.17}$$

with the following boundary conditions

$$r^2\eta^2 w_{,xx} - N_z + EA_{\epsilon z} + \hat{K}_0 w_{,x} =$$
$$EA_z \left(u_{,x} + \frac{1}{2}w_{,x}^2 - \frac{1}{8}w_{,x}^4 - \frac{1}{2}u_{,x}w_{,x}^2 + \frac{1}{2}u_{,x}^2 w_{,x}^2 \right)\bigg|_{x=0} \tag{3.18}$$

$$r^2\eta^2 w_{,xx} - N_z + EA_{\epsilon z} - \hat{K}_L w_{,x} =$$
$$EA_z \left(u_{,x} + \frac{1}{2}w_{,x}^2 - \frac{1}{8}w_{,x}^4 + \frac{1}{2}u_{,x}w_{,x}^2 + \frac{1}{2}u_{,x}^2 w_{,x}^2 \right)\bigg|_{x=1} \tag{3.19}$$

where ν and μ are added damping terms for the axial and transverse directions, respectively. The system is now normalized in time to the fundamental transverse frequency of the beam. Notice, the normalized axial frequency is the ratio of the transverse and axial speeds of sound. Since $\frac{c_2}{c_1} = \sqrt{\frac{N_0}{EA}}$, we can see the direct result the pretension causes when applied in a perturbation expansion.

Now, defining all measurements from the neutral axis, thus eliminating the N_z terms, and applying perturbation techniques, a system of linear equations can be developed. The solution presented was developed using a combination of three standard perturbation techniques: Lindstedt-Poincaré, Multiple Time Scales, and Matched Asymptotic Expansions (67). Using the following expansions:

$$\begin{aligned}
\tau &= \omega t \\
T_n &= \varepsilon^n \tau \\
\omega &= \omega_0 + \varepsilon\omega_1 + \varepsilon^2\omega_2 + \ldots \\
w(x,\tau;\varepsilon) &= \varepsilon^2 w_2(x,\tau) + \varepsilon^3 w_3(x,\tau) + \varepsilon^4 w_4(x,\tau) + \ldots \\
u(x,\tau;\varepsilon) &= \varepsilon^3 u_3(x,\tau) + \varepsilon^4 u_4(x,\tau) + \varepsilon^5 u_5(x,\tau) + \ldots \\
D &= D_0 + \varepsilon D_1 + \varepsilon^2 D_2 + \ldots \\
\varepsilon &= r
\end{aligned} \tag{3.20}$$

where $D_i = \frac{\partial}{\partial T_i}$, and $\omega_0 = 1$ in this problem, we simultaneously apply Lindstedt-Poincaré and Multiple Time Scale methods. Applying the expansions in Equation 3.21 and the scaling rules in Equation 3.15 to the system of linear partial differential equations, we can expand the original nonlinear system. Experimental results have shown the transverse deflection is on the order of optical wavelengths, indicating the small initial order ($\sim \varepsilon^2$), is acceptable (17). The axial deflection is expected to be much smaller than the transverse and is scaled as such.

The matched asymptotic expansion method using multiple scales (67) is also used to develop a solution which illustrates the string-like behavior in the center of the beam, with small boundary layers which act as a beam.

Applying the expansions (Equations 3.21) to Equations 3.15 through 3.17, then extracting equations based on the relative order, the following system of equations are derived for the 'outer' solution related to the center portion of the beam string (numerical subscripts attached to physical properties indicate assigned order):

$$u_{3,00} - \eta u_{3,xx} = 0 \tag{3.21}$$

$$
\begin{aligned}
u_{4,00} - \eta u_{4,xx} = {}& -2u_{3,01} - 2\omega_1 u_{3,00} - 2\nu_1 u_{3,0} - 2P_2 w_{2,x} \\
& + \frac{1}{2}(\eta - 1)\left(w_{2,x}^2\right)_{,x} - EA_{z2} w_{2,xxx}
\end{aligned}
\tag{3.22}
$$

$$
\begin{aligned}
u_{5,00} - \eta u_{5,xx} = {}& -2u_{4,01} - 2\omega_1 u_{4,00} - 2\nu_1 u_{4,0} - 2P_2 w_{3,x} \\
& -2u_{3,02} - u_{3,11} - 4\omega_1 u_{3,01} - \left(\omega_1^2 + 2\omega_2\right) u_{3,00} \\
& -2\nu_1 u_{3,1} - 2\omega_1 \nu_1 u_{3,0} + \eta\left(w_{2,x} w_{3,x}\right)_{,x} - EA_{z2} w_{3,xxx}
\end{aligned}
\tag{3.23}
$$

$$w_{2,00} - w_{2,xx} = P_2 \tag{3.24}$$

$$w_{3,00} - w_{3,xx} = -2w_{2,01} - 2\omega_1 w_{2,00} - 2\mu_1 w_{2,0} \tag{3.25}$$

$$
\begin{aligned}
w_{4,00} - w_{4,xx} = {} & -w_{2,11} - 2w_{2,02} - 4\omega_1 w_{2,01} - \left(\omega_1^2 + 2\omega_2\right) w_{2,00} - 2\mu_1 w_{2,1} \\
& -2\omega_1 \mu_1 w_{2,0} - 2w_{3,01} - 2\omega_1 w_{3,00} - 2\mu_1 w_{3,0} \\
& -EA_{\epsilon2} w_{2,xx} - w_{2,xxxx}.
\end{aligned}
\tag{3.26}
$$

These equations indicate in the 'outer' region of the beam, which is the dominant center portion, the dynamic shape of the beam appears as a string.

Next stretch the x dimension near one end (first at $x = 0$,) to create the 'inner' solution near that end of the beam. Applying the stretched variable $\xi = \frac{x}{\varepsilon}$, the following system is derived for the region near the $x = 0$ end of the beam

$$-\eta u_{3,\xi\xi} = \frac{1}{2}(\eta - 1)\left(w_{2,\xi}^2\right)_{,\xi} - EA_{z2} w_{2,\xi\xi\xi} \tag{3.27}$$

$$-\eta u_{4,\xi\xi} = (\eta - 1)\left(w_{2,\xi} w_{3,\xi}\right)_{,\xi} - EA_{z2} w_{3,\xi\xi\xi} \tag{3.28}$$

$$
\begin{aligned}
-\eta u_{5,\xi\xi} = {} & -u_{3,00} - 2P_2 w_{2,\xi} + \frac{1}{2}(\eta - 1)\left(w_{3,\xi}^2 + 2w_{2,\xi} w_{4,\xi} - 2u_{3,\xi} w_{2,\xi}^2\right)_{,\xi} \\
& + \frac{1}{2}EA_{\epsilon2}\left(w_{2,\xi}^2\right)_{,\xi} - EA_{z2}\left(w_{4,\xi\xi} - \frac{3}{2}\left(w_{2,\xi}{}^3\right)_{,\xi}\right)
\end{aligned}
\tag{3.29}
$$

$$w_{2,\xi\xi\xi\xi} - w_{2,\xi\xi} = 0 \tag{3.30}$$

$$w_{3,\xi\xi\xi\xi} - w_{3,\xi\xi} = 0 \tag{3.31}$$

$$
\begin{aligned}
w_{4,\xi\xi\xi\xi} - w_{4,\xi\xi} = {} & P_2 - w_{2,00} + EA_{\epsilon2} w_{2,\xi\xi} - EA_{z2} u_{3,\xi\xi\xi} \\
& + (\eta - 1)\left(u_{3,\xi} w_{2,\xi} + \frac{1}{2} w_{2,\xi}^3\right)_{,\xi}.
\end{aligned}
\tag{3.32}
$$

3-8

These equations indicate beam-like behavior near the end. Similarly, the 'inner' expansions for the other end ($x = 1$) of the beam can be derived using the stretching transform $\zeta = \frac{1-x}{\varepsilon}$:

$$-\eta u_{3,\zeta\zeta} = -\frac{1}{2}(\eta - 1)\left(w_{2,\zeta}^2\right)_{,\zeta} + EA_{z2}w_{2,\zeta\zeta\zeta} \tag{3.33}$$

$$-\eta u_{4,\zeta\zeta} = -(\eta - 1)\left(w_{2,\zeta}w_{3,\zeta}\right)_{,\zeta} + EA_{z2}w_{3,\zeta\zeta\zeta} \tag{3.34}$$

$$-\eta u_{5,\zeta\zeta} = -u_{3,00} + 2P_2 w_{2,\zeta} - \frac{1}{2}(\eta - 1)\left(w_{3,\zeta}^2 + 2w_{2,\zeta}w_{4,\zeta} + 2u_{3,\zeta}w_{2,\zeta}^2\right)_{,\zeta}$$
$$-\frac{1}{2}EA_{\epsilon 2}\left(w_{2,\zeta}^2\right)_{,\zeta} + EA_{z2}\left(w_{4,\zeta\zeta} - \frac{3}{2}\left(w_{2,\zeta}^3\right)_{,\zeta}\right)_{,\zeta} \tag{3.35}$$

$$w_{2,\zeta\zeta\zeta\zeta} - w_{2,\zeta\zeta} = 0 \tag{3.36}$$

$$w_{3,\zeta\zeta\zeta\zeta} - w_{3,\zeta\zeta} = 0 \tag{3.37}$$

$$w_{4,\zeta\zeta\zeta\zeta} - w_{4,\zeta\zeta} = P_2 - w_{2,00} + EA_{\epsilon 2}w_{2,\zeta\zeta} + EA_{z2}u_{3,\zeta\zeta\zeta} \tag{3.38}$$
$$-(\eta - 1)\left(u_{3,\zeta}w_{2,\zeta} - \frac{1}{2}w_{2,\zeta}^3\right)_{,\zeta}. \tag{3.39}$$

This system, represented by string equations in the 'outer' region and beam equations in the 'inner' regions, is linear with respect to the unknown variable at all levels, self-adjoint, and can be solved. Since the membrane may be mounted using an elastic ring, a torsional spring boundary condition appears more accurate than a clamped condition. This model can also represent a region between the edge of the membrane and the beginning of the piezoelectrically actuated region. This also may provide an additional control mechanism. Scaling and expanding these dimensional

boundary conditions

$$u(0) = 0$$

$$u_{,x}(0) = 0$$

$$w(0) = 0 \tag{3.40}$$

$$EIw_{,xx}(0) = N_z - EA_{\epsilon z} - K_0 w_{,x}(0) +$$

$$EA_z \left(u_{,x} + \frac{1}{2}w_{,x}^2 - \frac{1}{8}w_{,x}^4 - \frac{1}{2}u_{,x}w_{,x}^2 + \frac{1}{2}u_{,x}^2 w_{,x}^2 \right)$$

$$u(L) = 0$$

$$u_{,x}(L) = 0$$

$$w(L) = 0 \tag{3.41}$$

$$EIw_{,xx}(L) = N_z - EA_{\epsilon z} + K_L w_{,x}(L) -$$

$$EA_z \left(u_{,x} + \frac{1}{2}w_{,x}^2 - \frac{1}{8}w_{,x}^4 - \frac{1}{2}u_{,x}w_{,x}^2 + \frac{1}{2}u_{,x}^2 w_{,x}^2 \right)$$

using the same scaling previously presented, the following non-dimensional boundary conditions are derived for the $x = 0$ end of the beam

$$u_3(0) = 0 \quad u_{3,\xi}(0) = 0$$

$$u_4(0) = 0 \quad u_{4,\xi}(0) = 0$$

$$u_5(0) = 0 \quad u_{5,\xi}(0) = 0$$

$$\tag{3.42}$$

$$w_2(0) = 0 \quad N_0^2 w_{2,\xi\xi}(0) = -K_0 w_{2,\xi}(0)$$

$$w_3(0) = 0 \quad N_0^2 w_{3,\xi\xi}(0) = -K_0 w_{3,\xi}(0) - EA_{\epsilon z3}$$

$$w_4(0) = 0 \quad N_0^2 w_{4,\xi\xi}(0) = -K_0 w_{4,\xi}(0) + EA_{z2}u_{3,\xi}.$$

The opposite end, $x = L$, boundary conditions become

$$u_3(0) = 0 \quad u_{3,\zeta}(0) = 0$$
$$u_4(0) = 0 \quad u_{4,\zeta}(0) = 0$$
$$u_5(0) = 0 \quad u_{5,\zeta}(0) = 0$$

$$w_2(0) = 0 \quad N_0^2 w_{2,\zeta\zeta}(0) = -K_1 w_{2,\zeta}(0)$$
$$w_3(0) = 0 \quad N_0^2 w_{3,\zeta\zeta}(0) = -K_1 w_{3,\zeta}(0) - EA_{\epsilon z3}$$
$$w_4(0) = 0 \quad N_0^2 w_{4,\zeta\zeta}(0) = -K_1 w_{4,\zeta}(0) + EA_{z2} u_{3,\zeta}.$$

where it can now be seen that $EA_{\epsilon z3}$ represents the non-dimensional moment imposed by the piezoelectric layer(s), and $N_z = 0$ using the neutral axis as the datum. This research is concerned with both the dynamical properties of this material as well as its static shape manipulation capabilities. First, to study the shaping capabilities of the system, the static solution is considered.

3.3   Static Shaping

Noticing the system is now separated, the axial solution (u) is completely determined by lower order transverse solutions (w). We can solve the system of equations, using a two level matching, to find the following composite solution to order ε^3

$$
\begin{aligned}
u^c(x) &= 0 \\
w^c(x) &= \varepsilon^2 \frac{P_2}{2} \left(x - x^2 \right) - \varepsilon^3 \left[\Gamma_0 \left(1 - x - e^{-\frac{x}{\varepsilon}} \right) + \Gamma_1 \left(x - e^{-\frac{1-x}{\varepsilon}} \right) \right]
\end{aligned}
\quad (3.44)
$$

3-11

Property	Kapton	PVDF
Modulus, E	2.8 GPa	1.8 GPa
Thickness, H	100 micron	50 micron
Piezo Stress, d		$2.76x10^{-7}C/in^2$

Table 3.1   Material Properties

where

$$
\begin{aligned}
\Gamma_0 &= \frac{K_0}{K_0 - N_0^2}\left[\frac{P_2}{2} + \frac{EA_{\epsilon z3}}{K_0}\right] \\
\Gamma_1 &= \frac{K_1}{K_1 - N_0^2}\left[\frac{P_2}{2} + \frac{EA_{\epsilon z3}}{K_1}\right].
\end{aligned}
\tag{3.45}
$$

From this solution, we can see the axial distortion is not present to order ε^3. We will neglect the axial displacement to this level since the 'smallness' factor can be roughly the ratio of thickness to length of the membrane. As a note, the axial displacement equation is not trivial at the next order.

Figure 3.3 illustrates the behavior of the piezoelectric laminate beam with no pressure differential and symmetric edge conditions. Using a 15 cm long, simple 3 layer laminate with the base layer of Kapton, and two layers of PVDF with the properties listed in Table 3.1, reasonable environmental and actuation values can be applied to yield interesting results.

Actuation causes a pistoning of the center portion of the beam a total of approximately ten wavelengths of visible light ($\lambda \sim 600nm$). This corresponds favorably with experimental observations (17). The effective boundary layer region is approximately of the order of $\sqrt{\varepsilon}$, as expected from the original mathematical foundation. Because the center 'outer' region of the beam behaves as a string, incapable of countering any bending moment, this region can only produce a linear contribution. With the 'inner' regions providing the necessary bending stiffness to counter
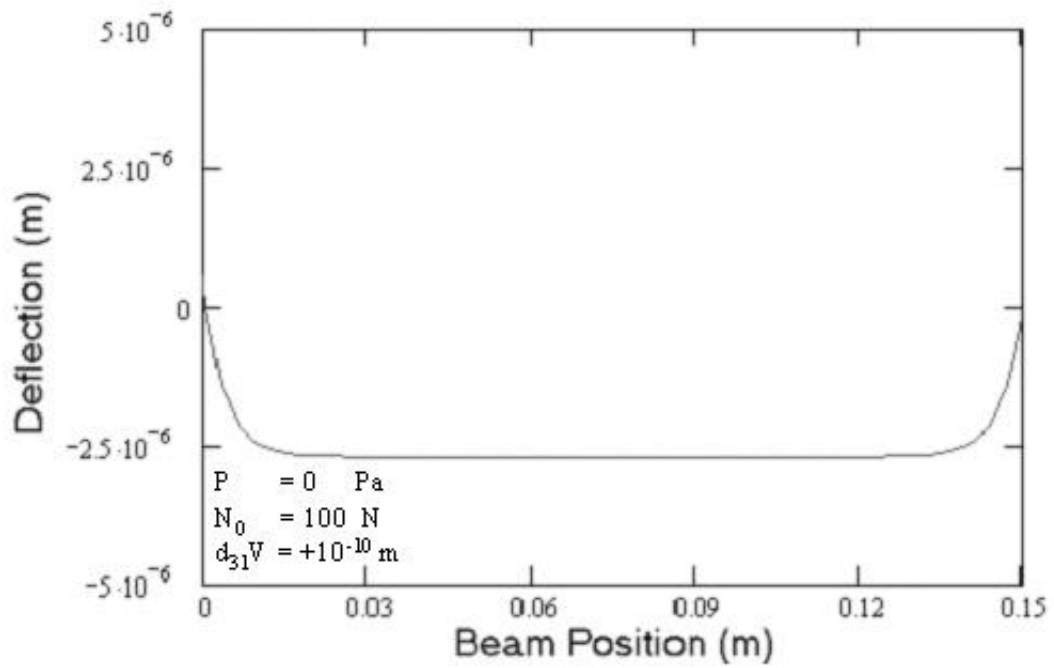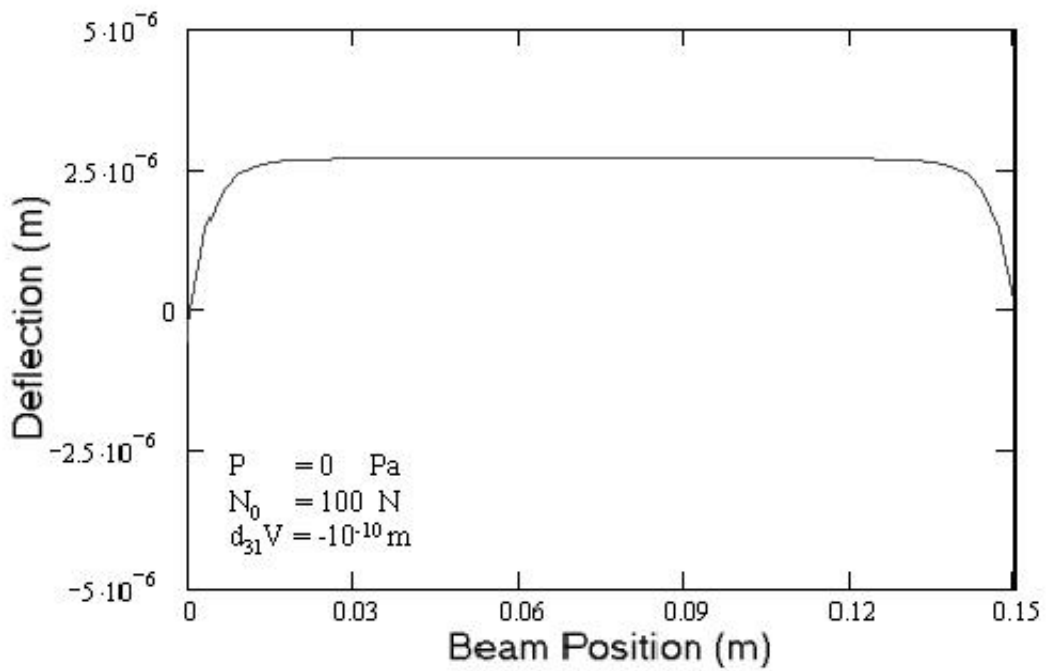
Figure 3.3 Unpressurized Piezoelectric Beam Deflection: (a)Positive Voltage Effects (b)Negative Voltage Effects

3-13
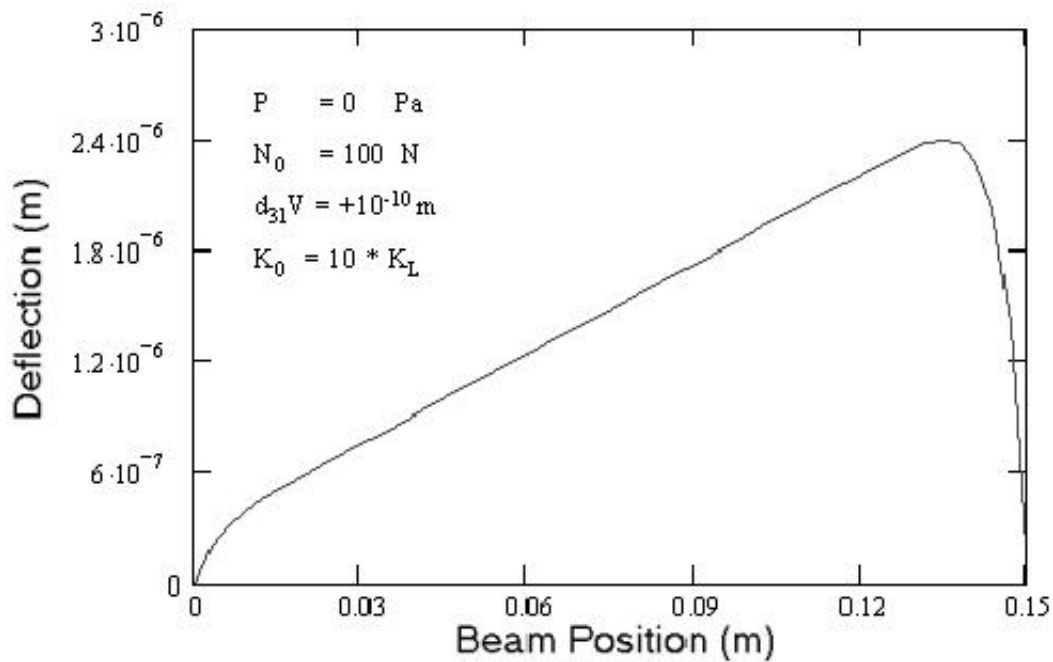
Figure 3.4   Asymmetric Edge Control Effects (Unpressurized Beam)

the piezo moment applied, these boundary regions illustrate significant curvature changes.

Results from applying dissimilar edge stiffness values are shown in Figure 3.4. Using a combination of edge control and piezoelectric laminate actuation, a reflected wavefront can be modified by ten wavelengths of tilt ($\lambda \sim 500nm$). Again notice the boundary regions are the same magnitude as the symmetric case previously discussed.

If the beam has a small pressure differential applied, similar results are possible. Symmetric edge conditions and actuation results in additional curvature alteration (see Figure 3.5). The solid line represents the actual surface deflection given the applied conditions, whereas the dashed line indicates the effective surface change due to the applied piezo effect. In this case, the wavefront modification again produces a plunging effect. As an additional note, different edge conditions result in addi-

3-14
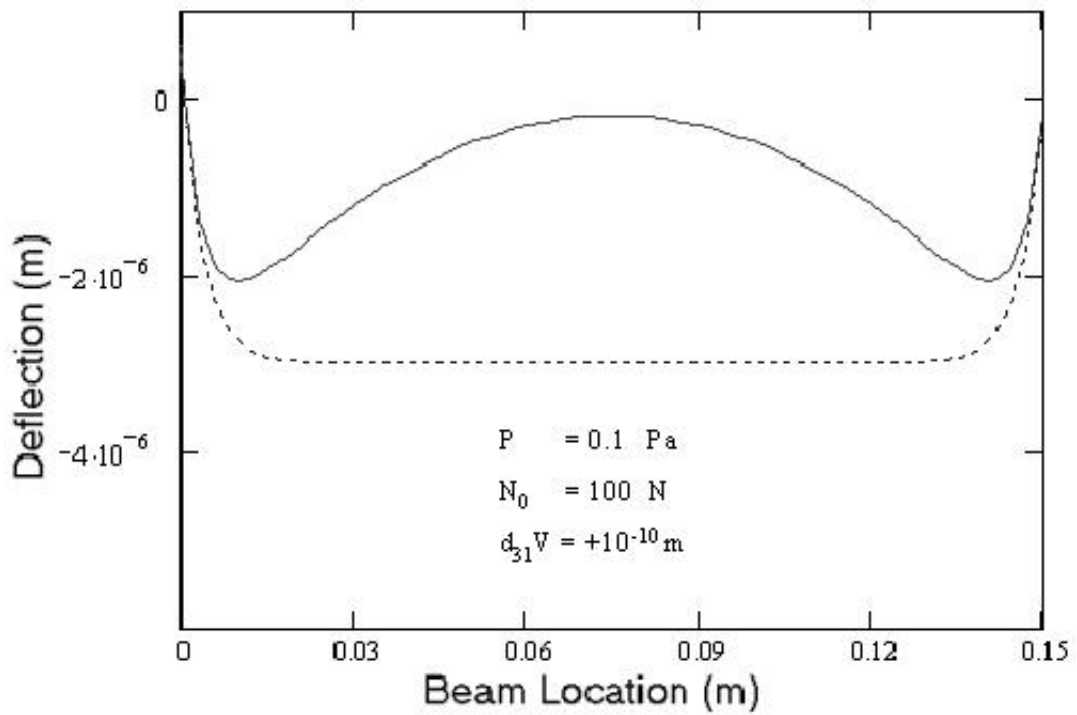
(a)
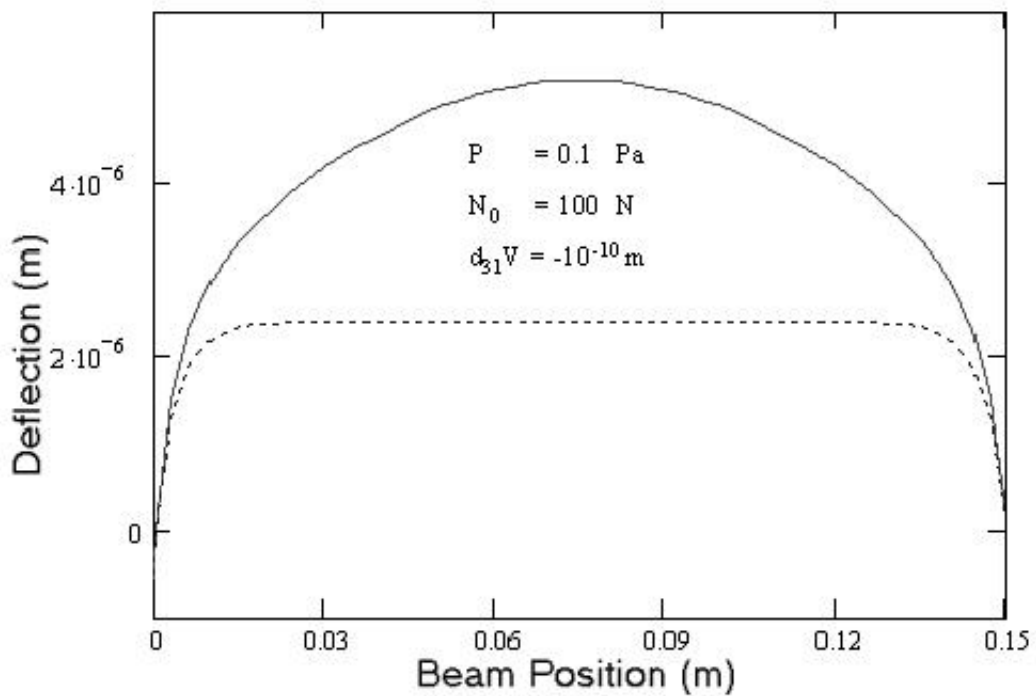
(b)

Figure 3.5   Pressurized Piezoelectric Beam Deflection (Dashed Line Represents Piezoelectric Effect): (a) Positive Voltage Effects (b) Negative Voltage Effects

3-15

tional tilt behavior as seen in the non-pressurized system. With the static shaping capabilities understood, interest lies in the dynamic nature of the laminate.

3.4 Dynamic Response

As discussed in the previous section, the axial equations (u) are decoupled from the transverse equations (w) when the system is scaled and expanded. Solving the system of equations at order ε^2, and eliminating any terms linear in time, yields a simple string:

$$w_2^c(x) = \frac{P_2}{2}\left(x - x^2\right) + \sum_{i=1}^{\infty} a_{1n}(T_1)\left(\mathrm{e}^{i\beta_{n0}(T_0+x)} - \mathrm{e}^{i\beta_{n0}(T_0-x)} + cc\right) \qquad (3.46)$$

where $\beta_{n0} = n\pi$ and $a_{1n}(T_1)$ can be a function of $T_1, T_2, \ldots$, and is yet to be determined. We now concentrate on the solution for next level of equations at order ε^3. Since this system is self-adjoint, we apply the Fredholm Alternative Theorem to derive the necessary solvability conditions. As a result, the $a_{1n}(T_1)$ coefficients in Equation 3.46 as well as ω_1 can be determined based on the applied boundary conditions.

We will concern ourselves with two different conditions: constant and periodic forcing. The forcing is applied through the thermal and electrical parameters:

$$
\begin{aligned}
EA_{\epsilon 2} &= f_0 + f\sin[(\Omega + \varepsilon\delta)t] \\
&= f_0 + f\sin(\Omega T_0 + \delta T_1) \\
EA_{\epsilon z3} &= m_0 + m\sin[(\Omega + \varepsilon\delta)t] \\
&= m_0 + m\sin(\Omega T_0 + \delta T_1) \qquad (3.47)
\end{aligned}
$$

where Ω will be considered a modal frequency, and δ is a small detuning parameter. Herein two values of Ω: $\beta_{j0}, 2\beta_{j0}$, which represent odd and even modes, are examined. To the order studied, these selections represent a complete set of possible solutions.

3-16

Applying the solvability conditions which effectively requires cancellation of all modes existing in 3.46 results in the following:

$$\omega_1 = -\frac{1}{\beta_{n0}}\left(\delta - i\mu_1\right) \tag{3.48}$$

and

$$\begin{aligned} a_{1k} &= 0 \, (k \neq j) \\ &= A_{1k}\mathrm{e}^{i\delta T_1} \, (k = j). \end{aligned} \tag{3.49}$$

where

$$A_{1k} = -\frac{m}{2\beta_{k0}}\left[\frac{(K_1 - N_0^2) - (-1)^k (K_0 - N_0^2)}{K_1 (K_0 - N_0^2) + K_0 (K_1 - N_0^2)}\right]. \tag{3.50}$$

It is now clear, with symmetric boundary conditions, only the single odd mode exists at this level. The solution for the next level transverse displacement is

$$\begin{aligned} w_3^c(x) &= -\frac{P_2}{2}\left[\frac{K_0}{K_0 - N_0^2}\right]\left(1 - x - \mathrm{e}^{-\xi}\right) \\ &\quad -\frac{P_2}{2}\left[\frac{K_1}{K_1 - N_0^2}\right]\left(x + \mathrm{e}^{-\zeta}\right) \\ &\quad -a_{1k}\beta_{j0}\left[\frac{K_0}{K_0 - N_0^2}\mathrm{e}^{-\xi} - (-1)^k\frac{K_1}{K_1 - N_0^2}\mathrm{e}^{-\zeta}\right]\sin(\beta_{j0}T_0) \\ &\quad -m\left[\frac{1}{K_0 - N_0^2}\mathrm{e}^{-\xi} - (-1)^k\frac{1}{K_1 - N_0^2}\mathrm{e}^{-\zeta}\right]\sin(\beta_{j0}T_0 + \delta T_1) \\ &\quad +\sum_{i=1}^{\infty}\left(a_{2n}(T_1)\mathrm{e}^{i\beta_{n0}(T_0+x)} + a_{3n}(T_1)\mathrm{e}^{i\beta_{n0}(T_0-x)} + cc\right). \end{aligned} \tag{3.51}$$

As in the static solution, the axial displacement solution is trivial to this level, and neglected in this analysis.

Continuing with the next level, we can derive the necessary solvability conditions which require cancellation of all modes existing in both the previous levels.

3-17

The results of interest are:

$$\omega_2 \begin{aligned} &= \frac{1}{\beta_{n0}^2}\left(\mu_1^2 + 2\delta^2 + \beta_{n0}^4 - f_0\beta_{n0}^2\right) & (\Omega = \beta_{j0}) \\ &= \frac{1}{\beta_{n0}^2}\left(\mu_1^2 + 2\delta^2 + \beta_{n0}^4 - f_0\beta_{n0}^2 - \frac{f}{2}\beta_{n0}^2 e^{i\delta T_1}\right) & (\Omega = 2\beta_{j0}) \end{aligned} \tag{3.52}$$

and

$$\begin{aligned} a_{2k} &= 0 & (k \neq j) \\ a_{2k} &= A_{2k}e^{i\delta T_1} & (k = j) \\ a_{3k} &= -\bar{a}_{2k}. \end{aligned}$$

where

$$A_{2k} = -\frac{fP_2}{2\beta_{k0}^2} - i\frac{m}{K_0 - N_0^2}\left[1 - K_0\left(\frac{(K_1 - N_0^2) - (-1)^k(K_0 - N_0^2)}{K_1(K_0 - N_0^2) + K_0(K_1 - N_0^2)}\right)\right]. \tag{3.54}$$

Applying these results, and the original scaling used, we can derive the dimensional results. Assuming an odd driving frequency ($n = odd$), the modal frequency for the beam-string is now:

$$\beta_n = (n\pi + \delta)\omega_n^*\left(\sqrt{\frac{N}{\rho A L^2}}\right) \tag{3.55}$$

where

$$\omega_n^* = 1 - \varepsilon\frac{\delta}{n\pi} + \varepsilon^2\frac{1}{2(n\pi)^2}\left(\mu_1^2 + 2\delta^2 + (n\pi)^4 - f_0(n\pi)^2\right) \tag{3.56}$$

which illustrates the difference (to this level) of the piezothermoelastic beam-string frequencies from the standard string frequencies: $\beta_n = n\pi\sqrt{\frac{N}{\rho A L^2}}$.

Maximum deflection per volt applied to the laminate described here is presented in Figure 3.6. As we select the higher modes, the resultant deflection becomes less. Figure 3.7 illustrates the dynamic behavior of the beam-string through its first five natural modes. The solid line indicates the actual beam deflection, while the dashed line quantifies the actual change from the static position. The center portion behaves much like a string, while the ends maintain the stiffness associated with

3-18
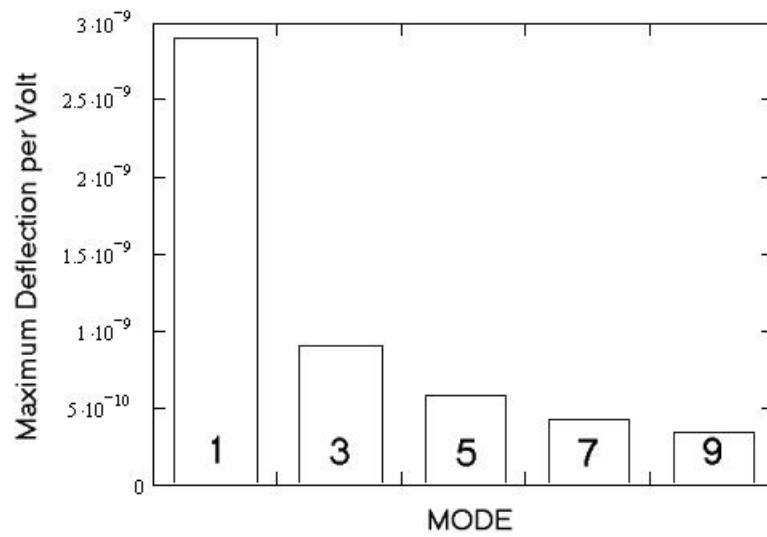
Figure 3.6   Maximum Dynamic Deflection

beams. As expected, the even modes are much less prominent due to the symmetric conditions.

The development of the perturbation solution of the nonlinear equations of motion derived in this chapter provides a solution for slender, flexible, laminated beams made of piezothermoelastic material. The results illustrate the effectiveness of a Kapton/PVDF beam at optical wavelengths. Further development into two dimensions is continued in the next chapter.

3-19
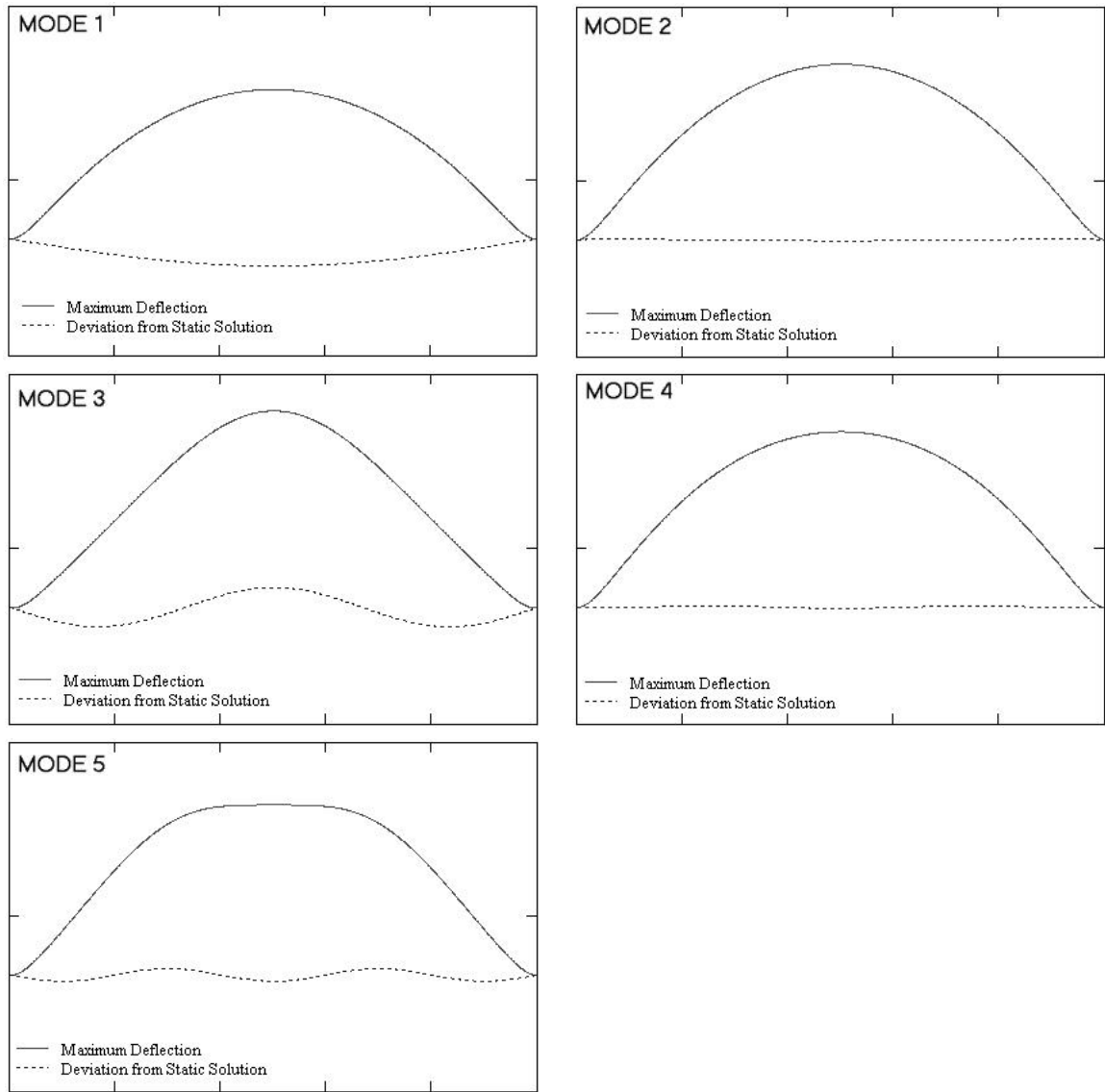
Figure 3.7   Mode Shape Results

3-20

IV.   Piezothermoelastic Plates

The previous chapter presented the analytical solution of a non-linear dynamic piezoelectric laminated beam-string. Using perturbation methods, a solution was developed assuming the beam's length was much larger than its width. This chapter expands this methodology to study a circular plate with a very small thickness to radius ratio.

4.1   Laminated Piezothermoelastic Plate-Membrane

To develop the necessary fundamental equations used in this two-dimensional analysis, again, an energy-based derivation is needed. The potential energy of an elastic, circular plate (radius=R) can be defined using the strain energy representation (65):

$$\mathbb{V} = \int_{\mathcal{V}} \frac{1}{2} \{\epsilon\}^T \{\sigma\} - \{\epsilon\}^T \{\sigma_0\} + \{\epsilon_0\}^T \{\sigma\} d\mathcal{V} + \frac{1}{2} K(\theta) w_{,r}(R,t)^2 \qquad (4.1)$$

with

$$\epsilon_0 = \alpha T + \frac{d_{31} V}{t}$$

$$\sigma_0 = \frac{N_i}{A} \qquad (4.2)$$

$$\sigma = [E]\{\epsilon\}$$

$$(4.3)$$

where ϵ_0 is prestrain resulting from thermal or piezoelectric actuation, σ_0 is the prestress resulting from any initial axial load (N_i) across the cross-sectional area (A), ϵ is the strain field in the plate, and σ is stress, equal to the product of strain

and the material's modulus matrix when in a state of plane stress:

$$[E] = \frac{E}{1-\nu^2} \begin{pmatrix} 1 & \nu & 0 \\ \nu & 1 & 0 \\ 0 & 0 & \frac{1}{2}(1-\nu) \end{pmatrix} \tag{4.4}$$

where E is the material's Young's Modulus, and ν is the material's Poisson's ratio. The addition of the spring constant $(K(\theta))$ at the edge of the plate allows for variable boundary conditions.

The general strain formula in a cylindrical coordinate frame of the neutral plane in the state of plane stress, neglecting in-plane quadratic terms, is (68)

$$\epsilon = \begin{pmatrix} u_{,r} + \frac{1}{2}w_{,r}^2 \\ \frac{u}{r} + \frac{1}{r}v_{,\theta} + \frac{1}{2}\frac{1}{r^2}w_{,\theta}^2 \\ \frac{1}{r}u_{,\theta} + v_{,r} - \frac{v}{r} + \frac{1}{r}w_{,\theta}w_{,r} \end{pmatrix}, \tag{4.5}$$

where, if we assume plane sections remain plane during deformation, a representation of the strain field through the laminate can then be derived as

$$\epsilon = \begin{pmatrix} \epsilon_{rr} \\ \epsilon_{\theta\theta} \\ \gamma_{r\theta} \end{pmatrix} = \begin{pmatrix} u_{,r} + \frac{1}{2}w_{,r}^2 - zw_{,rr} \\ \frac{u}{r} + \frac{1}{r}v_{,\theta} + \frac{1}{2}\frac{1}{r^2}w_{,\theta}^2 - z\left[\frac{1}{r^2}w_{,\theta\theta} + \frac{1}{r}w_{,r}\right] \\ \frac{1}{r}u_{,\theta} + v_{,r} - \frac{v}{r} + \frac{1}{r}w_{,\theta}w_{,r} - 2z\left[\frac{1}{r}w_{,r\theta}^2 - \frac{1}{r^2}w_{,\theta}\right] \end{pmatrix}. \tag{4.6}$$

Applying Equation 4.6 to Equation 4.1, the system's potential energy can be derived:

$$\mathbb{V} = \int_{\mathcal{V}} \frac{E}{2(1-\nu^2)} \left[\epsilon_{rr}^2 + 2\epsilon_{rr}\epsilon_{\theta\theta} + \epsilon_{\theta\theta}^2 + (1-\nu)\gamma_{r\theta}^2\right] \\ + \sigma_{0r}\epsilon_{rr} + \sigma_{0\theta}\epsilon_{\theta\theta} + \sigma_{0r\theta}\gamma_{r\theta} \, d\mathcal{V} + \frac{1}{2}K(\theta)w_{,r}(R,t)^2 \tag{4.7}$$

Neglecting rotatory inertia, the plate's kinetic energy can be represented as:

$$\mathbb{T} = \frac{1}{2} \int_{\mathcal{V}} \rho \left(u_{,t}^2 + v_{,t}^2 + w_{,t}^2 \right) d\mathcal{V} \tag{4.8}$$

where ρ is the plate's density. The radial, in-plane 'cross-track' and out-of-plane 'transverse' deflections are represented as u, v and w, respectively.

To analyze this laminate, further development is required. As in Chapter III, each layer can have independent elastic, thermal, and piezoelectric properties. Again, elastically isotropic materials in each layer are assumed. Assuming through-the-thickness strain is constant at any cross-section, the system can be collapsed into a one-dimensional integrodifferential system using

$$
\begin{aligned}
\rho h &= \int_z \rho \, dz & &= \sum \int_{zi} \rho_i \, dz \\
N_{rz} &= \int_z \sigma_{0r}(A) z \, dz & &= \sum \int_{zi} \sigma_{0r}(A) z \, dz \\
EH &= \int_z \frac{E}{1-\nu^2} \, dz & &= \sum \int_{zi} \frac{E_i}{1-\nu_i^2} \, dz \\
N_r &= \int_z \frac{\sigma_{0r}}{A} \, dz & &= \sum \int_{zi} \frac{\sigma_{0ri}}{A} z \, dz \\
N_\theta &= \int_z \frac{\sigma_{0\theta}}{A} \, dz & &= \sum \int_{zi} \frac{\sigma_{0\theta i}}{A} z \, dz \\
N_{r\theta} &= \int_z \frac{\sigma_{r\theta}}{A} \, dz & &= \sum \int_{zi} \frac{\sigma_{0r\theta i}}{A} z \, dz \\
EH_{\epsilon r} &= \int_z \frac{E}{1-\nu^2} \epsilon_r \, dz & &= \sum \int_{zi} \frac{E_i}{1-\nu_i^2} \epsilon_{ri} \, dz \\
EH_{\epsilon\theta} &= \int_z \frac{E}{1-\nu^2} \epsilon_\theta \, dz & &= \sum \int_{zi} \frac{E_i}{1-\nu_i^2} \epsilon_{\theta i} \, dz \\
EZ_\epsilon &= \int_z \frac{E}{1-\nu^2} \epsilon_r z \, dz & &= \sum \int_{zi} \frac{E_i}{1-\nu_i^2} \epsilon_{ri} z \, dz \\
EZ &= \int_z \frac{E}{1-\nu^2} z \, dz & &= \sum \int_{zi} \frac{E_i}{1-\nu_i^2} z \, dz \\
D &= \int_z \frac{E}{1-\nu^2} z^2 \, dz & &= \sum \int_{zi} \frac{E_i}{1-\nu_i^2} z^2 \, dz
\end{aligned}
\tag{4.9}
$$

by integrating through each laminate layer i. The resulting equations of motion are then:

$$\rho h u_{,tt} - EH\frac{1}{r}\left([r\left(e_r + \nu e_\theta\right)]_{,r} + \frac{1}{2}(1-\nu)e_{r\theta,\theta} - e_\theta - \nu e_r\right) - \frac{1}{r}\left[N_r - N_\theta\right] =$$
$$EH_z\frac{1}{r}\left(\frac{1}{r^2}w_{,\theta\theta} + \frac{1}{r}w_{,r}\right. \tag{4.10}$$
$$\left. - \left[rw_{,rr} + \nu\frac{1}{r}w_{,\theta\theta}\right]_{,r} - (1-\nu)\left[\frac{1}{r}w_{,r\theta} - \frac{1}{r^2}w_{,\theta}\right]_{,\theta}\right)$$

$$\rho h v_{,tt} - EH\frac{1}{r}\left([e_\theta + \nu e_r]_{,\theta} + \frac{1}{2}(1-\nu)\left[e_{r\theta} + (re_{r\theta})_{,r}\right]\right) =$$
$$EH_z\frac{1}{r}\left(\left[\frac{1}{r^2}w_{,\theta\theta} + \frac{1}{r}w_{,r} + \nu w_{,rr}\right]_{,\theta}\right. \tag{4.11}$$
$$\left. + (1-\nu)\left[\frac{1}{r}w_{,r\theta} - \frac{1}{r^2}w_{,\theta} + \left(\frac{1}{r}w_{,r\theta} - \frac{1}{r^2}w_{,\theta}\right)_{,r}\right]\right)$$

$$\rho h w_{,tt} - N_r\frac{1}{r}\left(rw_{,r}\right)_{,r} - N_\theta\frac{1}{r^2}w_{,\theta\theta} - 2N_{r\theta}\frac{1}{r}w_{,r\theta} + D\nabla^4 w =$$
$$EH\frac{1}{r}\left([rw_{,r}\left(e_r + \nu e_\theta\right)]_{,r} + \left[\frac{1}{r}w_{,\theta}\left(e_\theta + \nu e_r\right)\right]_{,\theta}\right.$$
$$\left. + \frac{1}{2}(1-\nu)\left[(w_{,\theta}e_{r\theta})_{,r} + (w_{,r}e_{r\theta})_{,\theta}\right]\right)$$
$$+ EZ\frac{1}{r}\left(\left[\left(e_\theta + \nu e_r\right) + rw_{,r}\left[w_{,rr} + \nu\left(\frac{1}{r}w_{,r} + \frac{1}{r^2}w_{,\theta\theta}\right)\right]\right.\right.$$
$$\left.+ (1-\nu)\frac{1}{r}w_{,\theta}\left(w_{,r\theta} - \frac{1}{r}w_{,\theta}\right)\right]_{,r} \tag{4.12}$$
$$+ \left[(1-\nu)\frac{1}{r}e_{r\theta} + \frac{1}{r}w_{,\theta}\left[\frac{1}{r}w_{,r} + \frac{1}{r^2}w_{,\theta\theta} + \nu w_{,rr}\right]\right.$$
$$\left.-(1-\nu)\frac{1}{r}w_{,r}\left(w_{,r\theta} - \frac{1}{r}w_{,theta}\right)\right]_{,\theta}$$
$$\left.- [r\left(e_r + \nu e_\theta\right)]_{,rr} + \left[\frac{1}{r}\left(e_\theta + \nu e_r\right)\right]_{,\theta\theta} + (1-\nu)e_{r\theta,r\theta}\right)$$

4-4

where

$$\nabla^4 = \nabla^2\nabla^2$$

$$\nabla^2 = \frac{\partial^2}{\partial r^2} + \frac{1}{r}\frac{\partial}{\partial r} + \frac{1}{r}\frac{\partial^2}{\partial \theta^2} \tag{4.13}$$

$$e_r = u_{,r} + \frac{1}{2}w_{,r}^2$$

$$e_\theta = \frac{u}{r} + \frac{1}{r}v_{,\theta} + \frac{1}{2r^2}w_{,\theta}^2 \tag{4.14}$$

$$e_{r\theta} = \frac{1}{r}u_{,\theta} + v_{,r} + \frac{1}{r}v + \frac{1}{r}w_{,r}w_{,\theta}$$

$$N_r = N_{ir} - EH_{\epsilon r} - \nu EH_{\epsilon\theta}$$

$$N_\theta = N_{i\theta} - EH_{\epsilon\theta} - \nu EH_{\epsilon r} \tag{4.15}$$

$$N_{r\theta} = N_{ir\theta}$$

with the following boundary conditions of interest:

$$D\left[rw_{,rr} + \nu\left(\frac{1}{r}w_{,\theta\theta} + w_{,r}\right) \right] - N_{rz} + EZ_\epsilon =$$

$$K(\theta)w_{,r} + EZ\left[r\left(e_r + \nu e_\theta\right)\right] \Big|_{r=R} \tag{4.16}$$

$$w\Big|_{r=0} < \infty \tag{4.17}$$

If all measurements are with respect to the original neutral axis of a symmetric laminate, then $N_{rz} = 0$. Equations 4.10 through 4.12 represent the nonlinear thin plate equations of motion in cylindrical coordinates. Notice, the thermal and piezo-electric terms not only modify the in-plane tension within the plate (i.e. $EH_{\epsilon r}$ and $EH_{\epsilon\theta}$), but also produce moments at the boundary (i.e. EZ_ϵ).

To properly perform a perturbation analysis of this system, the system must be put in nondimensional form. The following nondimensional parameter scaling

4-5

rules are used:

$$\hat{r} = \frac{r}{R} \qquad \hat{z} = \frac{z}{R}\eta^2$$

$$\hat{u} = \frac{u}{R}\eta^2 \qquad \hat{w} = \frac{w}{Rr^*}\eta$$

$$\hat{v} = \frac{v}{R}\eta^2$$

$$\hat{r^*}^2 = \frac{D}{R^2 EH}\eta^2 \qquad \eta^2 = \frac{c_1^2}{c_2^2}$$

$$\hat{N}_r = \frac{1}{\eta^2} \qquad \hat{N}_{rz} = \frac{N_{rz}}{REH}\eta^2$$

$$\hat{N}_\theta = \hat{N}_r \qquad \hat{N}_{r\theta} = 0 \qquad\qquad (4.18)$$

$$\hat{EZ} = \frac{EZ}{REH}\eta^2 \qquad \hat{EZ}_\epsilon = \frac{EZ_\epsilon}{REH}\eta^2$$

$$\hat{K}(\theta) = \frac{K(\theta)}{REH}\eta^2 \qquad \hat{t}^2 = \frac{c_2^2}{R^2}t^2$$

$$\hat{EH}_{\epsilon r} = \frac{EH_{\epsilon r}}{EH}\eta^2 \qquad \hat{EH}_{\epsilon\theta} = \frac{EH_{\epsilon\theta}}{EH}\eta^2$$

where $c_1 = \sqrt{\frac{EH}{\rho h}}$ and $c_2 = \sqrt{\frac{N_r}{\rho h}}$ are the in-plane and transverse speeds of sound in the beam, to produce (eliminating the 'hats'):

$$u_{,tt} - \eta^2 \frac{1}{r}\left([r(e_r + \nu e_\theta)]_{,r} + \frac{1}{2}(1-\nu)e_{r\theta,\theta} - e_\theta - \nu e_r \right) =$$
$$-2\nu_u u_{,t} + \eta^4(1-\nu)\frac{1}{r}[EH_{\epsilon\theta} - EH_{\epsilon r}]$$
$$+\eta^2 EZ \frac{1}{r}\left(\frac{1}{r^2}w_{,\theta\theta} + \frac{1}{r}w_{,r} - \left[rw_{,rr} + \nu\frac{1}{r}w_{,\theta\theta} \right]_{,r} \right. \qquad (4.19)$$
$$\left. - (1-\nu)\left[\frac{1}{r}w_{,r\theta} - \frac{1}{r^2}w_{,\theta} \right]_{,\theta} \right)$$

$$v_{,tt} - \eta^2 \frac{1}{r}\left([e_\theta + \nu e_r]_{,\theta} + \frac{1}{2}(1-\nu)\left[e_{r\theta} + (re_{r\theta})_{,r} \right] \right) = -2\nu_v v_{,t}$$
$$-\eta^2 EZ \frac{1}{r}\left(\left[\frac{1}{r^2}w_{,\theta\theta} + \frac{1}{r}w_{,r} + \nu w_{,rr} \right]_{,\theta} \right. \qquad (4.20)$$
$$\left. + (1-\nu)\left[\frac{1}{r}w_{,r\theta} - \frac{1}{r^2}w_{,\theta} + \left(\frac{1}{r}w_{,r\theta} - \frac{1}{r^2}w_{,\theta} \right)_{,r} \right] \right)$$

4-6

$$w_{,tt} - \nabla^2 w + \epsilon^2 \nabla^4 w = -2\mu w_{,t}$$

$$-\eta^2 \left([EH_{\epsilon r} + \nu EH_{\epsilon\theta}] \frac{1}{r} (rw_{,r}) + [EH_{\epsilon\theta} + \nu EH_{\epsilon r}] \frac{1}{r^2} w_{,\theta\theta} \right)$$

$$+\frac{1}{r} \left([rw_{,r}(e_r + \nu e_\theta)]_{,r} + \left[\frac{1}{r} w_{,\theta}(e_\theta + \nu e_r) \right]_{,\theta} \right.$$

$$\left. + \frac{1}{2}(1-\nu) \left[(w_{,\theta} e_{r\theta})_{,r} + (w_{,r} e_{r\theta})_{,\theta} \right] \right)$$

$$+ EZ \frac{1}{r} \left(\left[(e_\theta + \nu e_r) + rw_{,r} \left(w_{,rr} + \nu \left(\frac{1}{r} w_{,r} + \frac{1}{r^2} w_{,\theta\theta} \right) \right) \right. \right. \tag{4.21}$$

$$\left. + (1-\nu) \frac{1}{r} w_{,\theta} \left(w_{,r\theta} - \frac{1}{r} w_{,\theta} \right) \right]_{,r}$$

$$+ \left[(1-\nu) \frac{1}{r} e_{r\theta} + \frac{1}{r} w_{,\theta} \left(\frac{1}{r} w_{,r} + \frac{1}{r^2} w_{,\theta\theta} + \nu w_{,rr} \right) \right.$$

$$\left. - (1-\nu) \frac{1}{r} w_{,r} \left(w_{,r\theta} - \frac{1}{r} w_{,\theta} \right) \right]_{,\theta}$$

$$\left. - [r(e_r + \nu e_\theta)]_{,rr} - \left[\frac{1}{r}(e_\theta + \nu e_r) \right]_{,\theta\theta} - (1-\nu) e_{r\theta,r\theta} \right)$$

where

$$\begin{aligned} e_r &= u_{,r} + \frac{1}{2} w_{,r}^2 \\ e_\theta &= \frac{u}{r} + \frac{1}{r} v_{,\theta} + \frac{1}{2r^2} w_{,\theta}^2 \\ e_{r\theta} &= \frac{1}{r} u_{,\theta} + v_{,r} + \frac{1}{r} v + \frac{1}{r} w_{,r} w_{,\theta} \end{aligned} \tag{4.22}$$

with the following boundary conditions :

$$\eta \epsilon^2 \left[rw_{,rr} + \nu \left(\frac{1}{r} w_{,\theta\theta} + w_{,r} \right) \right] - N_{rz} + EZ_\epsilon =$$

$$\eta K(\theta) w_{,r} - EZ \left[r(e_r + \nu e_\theta) \right] \bigg|_{r=1} \tag{4.23}$$

$$w \bigg|_{r=0} < \infty \tag{4.24}$$

4-7

where ν_u, ν_v and μ are added damping terms for the radial, in-plane, and transverse directions, respectively. The system is now normalized in time to the fundamental transverse frequency of the plate. Notice, the normalized in-plane frequency is the ratio of the transverse and in-plane speeds of sound. Since $\frac{c_2}{c_1} = \sqrt{N_0}$, we can see the direct result the pretension causes when applied in this perturbation expansion. As the in-plane wave speed becomes much larger than the transverse wave speed, the in-plane dynamics decouple from the first level solution.

Defining all measurements from the neutral axis, thus eliminating the N_{rz} term, and applying perturbation techniques, a system of linear equations can be developed which, when solved, provide the solution to the original non-linear problem. The application of interest is a very thin circular plate. The ratio of the radius of gyration to the radial dimension (ϵ) is very small (< 0.01), which will be the 'small' parameter in this analysis. The solution presented was developed using a combination of three standard perturbation techniques: Lindstedt-Poincaré, Multiple Time Scales, and Matched Asymptotic Expansions, as in the previous chapter (67). Using the following expansions

$$
\begin{aligned}
\tau &= \omega t \\
T_n &= \varepsilon^v \tau \\
\omega &= \omega_0 + \varepsilon\omega_1 + \varepsilon^2\omega_2 + \ldots \\
u(r,\theta,\tau;\varepsilon) &= \varepsilon^3 u_3(r,\theta,\tau) + \varepsilon^4 u_4(r,\theta,\tau) + \varepsilon^5 u_5(r,\theta,\tau) + \ldots \\
v(r,\theta,\tau;\varepsilon) &= \varepsilon^3 v_3(r,\theta,\tau) + \varepsilon^4 v_4(r,\theta,\tau) + \varepsilon^5 v_5(r,\theta,\tau) + \ldots \\
w(r,\theta,\tau;\varepsilon) &= \varepsilon^2 w_2(r,\theta,\tau) + \varepsilon^3 w_3(r,\theta,\tau) + \varepsilon^4 w_4(r,\theta,\tau) + \ldots \\
D &= D_0 + \varepsilon D_1 + \varepsilon^2 D_2 + \ldots \\
\eta &= \varepsilon^{-1}\eta_1 \\
\varepsilon &= r^*
\end{aligned}
\tag{4.25}
$$

where $D_i = \frac{\partial}{\partial T_i}$, and $\omega_0 = 1$ in this problem, we simultaneously apply Lindstedt-Poincaré and Multiple Time Scale methods. Applying the expansions in Equation 4.25 and the scaling rules in Equation 4.18 to the system of linear partial differential equations, we can expand the original nonlinear system. The axial deflection is expected to be much smaller than the transverse, and is scaled as such.

The matched asymptotic expansion method using multiple scales (67) is also used to develop a solution which illustrates the membrane-like behavior in the center of the plate, with a small boundary layer which acts at the edge of the plate.

Applying the expansions (Equations 4.25) to Equations 4.19 through 4.21, then extracting equations based on the relative order, the following system of equations are derived for the 'outer' solution related to the center portion of the plate (numerical subscripts attached to physical properties indicate assigned order). Two levels of in-plane displacement are presented with three levels of transverse displacement considering the dominance of the transverse motion

$$
\begin{aligned}
\frac{1}{r}\left(ru_{3,r}\right)_{,r} &-\frac{1}{r^2}u_3 + \frac{1}{2}(1-\nu)\frac{1}{r^2}u_{3,\theta\theta} \\
&-\frac{1}{r^2}v_{3,\theta} + \nu\frac{1}{r}v_{3,r\theta} + \frac{1}{2}(1-\nu)\frac{1}{r}\left(v_{3,r\theta} - \frac{1}{r}v_{3,\theta}\right) = 0
\end{aligned}
\tag{4.26}
$$

$$
\begin{aligned}
\frac{1}{r}\left(ru_{4,r}\right)_{,r} &-\frac{1}{r}u_4 + \frac{1}{2}(1-\nu)\frac{1}{r^2}u_{4,\theta\theta} \\
&-\frac{1}{r^2}v_{4,\theta} + \nu\frac{1}{r}v_{4,r\theta} + \frac{1}{2}(1-\nu)\frac{1}{r}\left(v_{4,r\theta} - \frac{1}{r}v_{4,\theta}\right) = -\frac{1}{\eta_1^2}u_{3,00} \\
&-\frac{1}{2}\left[\left(rw_{2,r}^2 + \frac{1}{r}w_{2,\theta}^2\right)_{,r} + (1-\nu)\frac{1}{r^2}\left(w_{2,r}w_{2,\theta}\right)_{,\theta}\right. \\
&\left. -w_{2,r}^2 - \nu\frac{1}{r^2}w_{2,\theta}^2\right] \\
&+\frac{1}{r}EZ_2\left[w_{2,\theta\theta} + \frac{1}{r}w_{2,r} - \left(r^2w_{2,rr} + \nu\frac{1}{r}w_{2,\theta\theta}\right)_{,r}\right. \\
&\left. -(1-\nu)\left(\frac{1}{r}w_{2,r\theta} - \frac{1}{r^2}w_{2,\theta}\right)_{,\theta}\right]
\end{aligned}
\tag{4.27}
$$

4-9

$$\frac{1}{r^2}v_{3,\theta} - \frac{1}{r}v_{3,r\theta} + \frac{1}{2}(1-\nu)\frac{1}{r}\left(\frac{1}{r}v_{3,\theta}v_{3,r\theta}\right)$$
$$+\frac{1}{r^2}v_{3,\theta\theta} + \frac{1}{2}(1-\nu)\frac{1}{r}\left[(rv_{3,r})_{,r} - \frac{1}{r}v_3\right] = 0 \tag{4.28}$$

$$\frac{1}{r^2}v_{4,\theta} - \frac{1}{r}v_{4,r\theta} + \frac{1}{2}(1-\nu)\frac{1}{r}\left(\frac{1}{r}v_{4,\theta}v_{4,r\theta}\right)$$
$$+\frac{1}{r^2}v_{4,\theta\theta} + \frac{1}{2}(1-\nu)\frac{1}{r}\left[(rv_{4,r})_{,r} - \frac{1}{r}v_4\right] = -\frac{1}{\eta_1^2}v_{3,00}$$
$$-\frac{1}{2}\left[\left(\frac{1}{r^2}w_{2,\theta}^2 + \nu w_{2,r}^2\right)_{,\theta} + (1-\nu)\frac{1}{r}\left[w_{2,r}w_{2,\theta} + (w_{2,r}w_{2,\theta})_{,\theta}\right]\right]$$
$$+\frac{1}{r}EZ_2\left[\left(\frac{1}{r^2}w_{2,\theta\theta} + \frac{1}{r}w_{2,r} + \nu w_{2,rr}\right)_{,\theta}\right. \tag{4.29}$$
$$\left.+(1-\nu)\left(\frac{1}{r}w_{2,r\theta} - \frac{1}{r^2}w_{2,\theta}\right) + r\left(\frac{1}{r}w_{2,r\theta} - \frac{1}{r^2}w_{r,\theta}\right)_{,r}\right]$$

$$w_{2,00} - \nabla^2 w_2 = 0 \tag{4.30}$$
$$w_{3,00} - \nabla^2 w_3 = -2w_{2,01} - 2\omega_1 w_{2,00} - 2\mu_1 w_{2,0} \tag{4.31}$$
$$w_{4,00} - \nabla^2 w_4 = -w_{2,11} - 2w_{0,02} - 4\omega_1 w_{2,01}$$
$$- \left(\omega_1^2 + 2\omega_2\right)w_{2,00} - 2\mu_1 w_{2,1}$$
$$-2\omega_1\mu_1 w_{2,0} - 2w_{3,01} - 2\omega_1 w_{3,00}$$
$$-2\mu_1 w_{3,0} - \eta_1^2\left[EH_{\epsilon r2} + \nu EH_{\epsilon\theta2}\right]\frac{1}{r}(rw_{2,r})_{,r}$$
$$-\eta_1^2\left[EH_{\epsilon\theta2} + \nu EH_{\epsilon r2}\right]\frac{1}{r^2}w_{2,\theta\theta} - \nabla^2 w_2. \tag{4.32}$$

These equations indicate, in the 'outer' region of the plate, the dynamic response and shape of the plate appear much as a membrane. Equation 4.30 is the dynamic equation of motion of a membrane. If we now stretch the radius dimension near the edge, we can create the 'inner' solution near that edge of the plate. No

4-10

boundary layer exists at the center of the plate ($r = 0$). Applying the stretching variable $\xi = \frac{1-r}{\varepsilon}$, the following system is derived for the stretched region near the $r = 1$:

$$u_{3,\xi\xi} = \frac{1}{2}\left(w_{2,\xi}^2\right)_{,\xi} + EZ_2 w_{2,\xi\xi\xi} \tag{4.33}$$

$$u_{4,\xi\xi} = \left(w_{2,\xi}w_{3,\xi}\right)_{,\xi} + \frac{1}{2}w_{2,\xi}^2 + u_{3,\xi} + \frac{1}{2}(1-\nu)v_{3,\xi\theta}$$
$$+ EZ_2\left(w_{3,\xi\xi\xi} + 3\xi w_{2,\xi\xi\xi} + 2w_{2,\xi\xi}\right) \tag{4.34}$$

$$\frac{1}{2}(1-\nu)v_{3,\xi\xi} = 0 \tag{4.35}$$

$$\frac{1}{2}(1-\nu)v_{4,\xi\xi} = -\frac{1}{2}\nu\left(w_{2,\xi}^2\right)_{,\theta} + \frac{1}{2}(1-\nu)\xi v_{3,\xi} + (1+\nu)u_{3,\xi\theta}$$
$$+ EZ_2(1+\nu)w_{2,\xi\xi\theta} \tag{4.36}$$

$$w_{2,\xi\xi\xi\xi} - w_{2,\xi\xi} = 0 \tag{4.37}$$

$$w_{3,\xi\xi\xi\xi} - w_{3,\xi\xi} = -\eta_1\left[w_{2,\xi}\left(u_{3,\xi} - \frac{1}{2}w_{2,\xi}^2\right)\right]_{,\xi} + w_{2,\xi} - w_{2,\theta\theta} + w_{2,\xi\xi\xi} \tag{4.38}$$

$$w_{4,\xi\xi\xi\xi} - w_{4,\xi\xi} = -w_{2,00} - \left[EH_{\epsilon r2} + EH_{\epsilon\theta 2}\right]w_{2,\xi\xi}$$
$$-\eta_1\left(\left[w_{2,\xi}\left(u_{4,\xi} - w_{2,\xi}w_{3,\xi}\right) + w_{3,\xi}\left(u_{3,\xi} - \frac{1}{2}w_{2,\xi}^2\right)\right]_{,\xi}\right.$$
$$+ w_{2,\xi}\left(u_{3,\xi} - \frac{1}{2}w_{2,\xi}^2\right) + \nu\left[w_{2,\xi}\left(u_3 + v_\theta\right)\right]_{,\xi}$$
$$\left. -\frac{1}{2}(1-\nu)\left[\left(w_{,\theta}v_{,\xi}\right)_{,\xi} + \left(w_{,\xi}v_{,\xi}\right)_{,\theta}\right]\right)$$
$$-EZ_2\left(u_{3,\xi} - \frac{1}{2}w_{2,\xi}^2\right)_{\xi\xi} \tag{4.39}$$

This system, represented by membrane equations in the 'outer' region and beam equations in the 'inner' region, is linear at each level, self-adjoint, and can

4-11

be solved. As applied in the previous one-dimensional analysis, a torsional spring boundary condition appears more flexible than a clamped condition. This also may be used as an additional control mechanism. The complete set of dimensional boundary conditions:

$$
\begin{aligned}
u(R,\theta) &= 0 \\
u_{,r}(R,\theta) &= 0 \\
u_{,\theta}(R,\theta) &= 0 \\
u(r,\theta) &= u(r,\theta+2\pi) \\
u_{,\theta}(r,\theta) &= u_{,\theta}(r,\theta+2\pi)
\end{aligned}
\tag{4.40}
$$

$$
\begin{aligned}
v(R,\theta) &= 0 \\
v_{,r}(R,\theta) &= 0 \\
v_{,\theta}(R,\theta) &= 0 \\
v(r,\theta) &= v(r,\theta+2\pi) \\
v_{,\theta}(r,\theta) &= v_{,\theta}(r,\theta+2\pi)
\end{aligned}
\tag{4.41}
$$

$$
\begin{aligned}
w(0,\theta) &= \alpha; \alpha < \infty \\
w_{,r}(0,\theta) &= -w_{,r}(0,\theta+\pi) \\
D\left[rw_{,rr}(R,\theta) + \nu\left(\tfrac{1}{r}w_{,\theta\theta}(R,\theta) + w_{,r}(R,\theta)\right)\right] &= \\
N_{rz} - EZ_\epsilon(R,\theta) + K(\theta)w_{,r}(R,\theta) & \\
+EZr\left[\left(u_{,r}(R,\theta) + \tfrac{1}{2}w_{,r}(R,\theta)^2\right)\right. & \\
\left. -\nu\left(\tfrac{1}{r}u(R,\theta) + \tfrac{1}{r}v_{,\theta}(R,\theta) + \tfrac{1}{2}\tfrac{1}{r^2}w_{,\theta}(R,\theta)^2\right)\right] &
\end{aligned}
\tag{4.42}
$$

using the same scaling rules previously presented, the following non-dimensional boundary conditions are derived:

$$u_3(R) = 0 \quad u_{3,\xi}(R) = 0$$
$$u_4(R) = 0 \quad u_{4,\xi}(R) = 0$$

$$v_3(R) = 0 \quad v_{3,\xi}(R) = 0$$
$$v_4(R) = 0 \quad v_{4,\xi}(R) = 0$$

$$(4.43)$$

$$w_2(R) = 0 \quad w_{2,\xi\xi}(R) = -K_R(\theta)w_{2,\xi}$$
$$w_3(R) = 0 \quad w_{3,\xi\xi}(R) = -K_R(\theta)w_{3,\xi} - \frac{1}{\eta_1}EZ_{\epsilon3} + (\xi w_{2,\xi\xi} - \nu w_{2,\xi})$$
$$\qquad\qquad\qquad\qquad - \frac{1}{\eta_1}EZ_2\left(u_{3,\xi} - \frac{1}{2}w_{2,\xi}^2\right)$$
$$w_4(R) = 0 \quad w_{4,\xi\xi}(R) = -K_R\theta w_{4,\xi} + [\xi w_{3,\xi\xi} + \nu\left(w_{2,\theta\theta} - w_{3,\xi}\right)]$$
$$\qquad\qquad\qquad\qquad - \frac{1}{\eta_1}EZ_2\left[(u_{4,\xi} - \xi u_{3,\xi} - w_{2,\xi}w_{3,\xi}) + \nu\left(u_3 + v_{3,\theta}\right)\right]$$

where it can now be seen that $EZ_{\epsilon3}$ represents the non-dimensional moment imposed by the piezoelectric layer(s), and $N_z = 0$ using the neutral axis. This system represents the nonlinear equations of motion of a circular plate-membrane. A further simplification at this point can be used to analyze an axisymmetric system.

4.2 Axisymmetric Solution

The nonlinear equations of motion of an axisymmetric, circular membrane can be derived by removing all θ dependence in the system developed in the previous section. At this point, we assume $EH_{\epsilon\theta} = EH_{\epsilon r} = EH_\epsilon$. This physically means bidirectional piezoelectric materials are assumed, and the spring stiffness is constant around the membrane. The follower-force pressure terms, similar to the beam terms in the previous chapter, will be reinserted at this stage also.

4-13

$$u_{,tt} - \eta^2 \left[\nabla^2 u - \frac{u}{r} \right] = \eta^2 \left[w_{,r} \left(w_{,rr} - \nu \frac{1}{2r} w_{,r}^2 \right) \right]$$
$$- 2\nu_u u_{,t} + \eta^2 EZ \frac{1}{r} \left[\frac{1}{r} w_{,r} - (r w_{,rr})_{,r} \right] - 2P w_{,r} \tag{4.44}$$

$$v_{,tt} - \frac{1}{2} \eta^2 \frac{1}{r} \left((1-\nu) \left[e_{r\theta} + (r e_{r\theta})_{,r} \right] \right) = -2\nu_v v_{,t} \tag{4.45}$$

$$w_{,tt} - \nabla^2 w + \epsilon^2 \nabla^4 w = - 2\mu w_{,t} + \frac{1}{r} \left([r w_{,r} e_r] + \nu [u w_{,r}] \right)_{,r}$$
$$- \eta^2 (1+\nu) EH_\epsilon \nabla^2 w + P\left[1 - 2u_{,r}\right]$$
$$+ EZ \frac{1}{r} \left(r \left[\nabla^2 u - e_\theta \right] + \nu \frac{3}{2} w_{,r}^2 \right)_{,r} \tag{4.46}$$

with the following moment balance boundary condition:

$$\eta \epsilon^2 \left[r w_{,rr} + \nu w_{,r} \right] - EZ_\epsilon + \eta K w_{,r} - EZ \left[(r u_{,r} - \nu u) + \frac{1}{2} w_{,r}^2 \right] \Bigg|_{r=1} \tag{4.47}$$

where

$$\nabla^4 = \nabla^2 \nabla^2$$
$$\nabla^2 = \frac{\partial^2}{\partial r^2} + \frac{1}{r} \frac{\partial}{\partial r} \tag{4.48}$$

$$e_r = u_{,r} + \frac{1}{2} w_{,r}^2$$
$$e_\theta = \frac{u}{r} \tag{4.49}$$
$$e_{r\theta} = v_{,r} + \frac{1}{r} v$$

$$N = N_i - (1+\nu) EH_\epsilon \tag{4.50}$$

with the following boundary conditions of interest:

$$D \left[r w_{,rr} + \nu w_{,r} \right] - N_z + EZ_\epsilon = K w_{,r} + EZ \left[(r u_{,r} + \nu u) + \frac{1}{2} w_{,r}^2 \right] \Bigg|_{r=R} \tag{4.51}$$

4-14

$$w\bigg|_{r=0} < \infty \tag{4.52}$$

After expanding, only the first couple expansion terms are collected and in-dividually evaluated. The following system of equations represent the 'outer' expansion of the system which dominates the deflection in the center region of the plate-membrane:

$$\nabla^2 u_3 - \frac{1}{r^2}u_3 = 0 \tag{4.53}$$

$$\nabla^2 u_4 - \frac{1}{r}u_4 = -\frac{1}{\eta_1^2}u_{3,00} - \frac{1}{2}\left[\left(rw_{2,r}^2\right)_{,r} - w_{2,r}^2\right]$$
$$+\frac{1}{r}EZ_2\left[\frac{1}{r}w_{2,r} - \left(r^2 w_{2,rr}\right)_{,r}\right] \tag{4.54}$$

$$\nabla^2 v_3 - \frac{1}{r^2}v_3 = 0 \tag{4.55}$$

$$\nabla^2 v_4 - \frac{1}{r^2}v_4 = -\frac{1}{\eta_1^2}v_{3,00} \tag{4.56}$$

$$w_{2,00} - \nabla^2 w_2 = 0 \tag{4.57}$$

$$w_{3,00} - \nabla^2 w_3 = -2w_{2,01} - 2\omega_1 w_{2,00} - 2\mu_1 w_{2,0} \tag{4.58}$$

$$w_{4,00} - \nabla^2 w_4 = -w_{2,11} - 2w_{0,02} - 4\omega_1 w_{2,01}$$
$$-\left(\omega_1^2 + 2\omega_2\right)w_{2,00} - 2\mu_1 w_{2,1} \tag{4.59}$$
$$-2\omega_1\mu_1 w_{2,0} - 2w_{3,01} - 2\omega_1 w_{3,00}$$
$$-2\mu_1 w_{3,0} - \eta_1^2(1+\nu)EH_{\epsilon 2}\frac{1}{r}\left(rw_{2,r}\right)_{,r}\frac{1}{r^2}w_{2,\theta\theta} - \nabla^2 w_2 \tag{4.60}$$

Again, these clearly indicate the dominant membrane behavior in the 'outer' region of the plate. As discussed previously, the only boundary layer occurs at the

4-15

edge of the plate. Applying the stretching variable $\xi = \frac{1-r}{\varepsilon}$, the following system is derived for the stretched region near the $r = 1$:

$$u_{3,\xi\xi} = \frac{1}{2}\left(w_{2,\xi}^2\right)_{,\xi} + EZ_2 w_{2,\xi\xi\xi} \tag{4.61}$$

$$u_{4,\xi\xi} = (w_{2,\xi}w_{3,\xi})_{,\xi} + \frac{1}{2}w_{2,\xi}^2 + u_{3,\xi}$$
$$+EZ_2\left(w_{3,\xi\xi\xi} + 3\xi w_{2,\xi\xi\xi} + 2w_{2,\xi\xi}\right) \tag{4.62}$$

$$\frac{1}{2}(1-\nu)v_{3,\xi\xi} = 0 \tag{4.63}$$

$$\frac{1}{2}(1-\nu)v_{4,\xi\xi} = +\frac{1}{2}(1-\nu)\xi v_{3,\xi} \tag{4.64}$$

$$w_{2,\xi\xi\xi\xi} - w_{2,\xi\xi} = 0 \tag{4.65}$$

$$w_{3,\xi\xi\xi\xi} - w_{3,\xi\xi} = -\eta_1\left[w_{2,\xi}\left(u_{3,\xi} - \frac{1}{2}w_{2,\xi}^2\right)\right]_{,\xi} + w_{2,\xi\xi\xi} \tag{4.66}$$

$$w_{4,\xi\xi\xi\xi} - w_{4,\xi\xi} = -w_{2,00} - \left[EH_{\epsilon r2} + EH_{\epsilon\theta2}\right]w_{2,\xi\xi}$$
$$-\eta_1\left(\left[w_{2,\xi}\left(u_{4,\xi} - w_{2,\xi}w_{3,\xi}\right) + w_{3,\xi}\left(u_{3,\xi} - \frac{1}{2}w_{2,\xi}^2\right)\right]_{,\xi}\right.$$
$$\left.+\left[w_{2,\xi}\left(u_{3,\xi} - \frac{1}{2}w_{2,\xi}^2\right)\right] - \nu\left[w_{2,\xi}u_3\right]_{,\xi}\right)$$
$$-EZ_2\left(u_{3,\xi} - \frac{1}{2}w_{2,\xi}^2\right)_{\xi\xi} \tag{4.67}$$

4-16

The adjusted boundary conditions are:

$$u(R) = 0$$
$$u_{,r}(R) = 0 \tag{4.68}$$

$$v(R) = 0$$
$$v_{,r}(R) = 0 \tag{4.69}$$

$$w(0) < \infty$$
$$D\left[rw_{,rr}(R) + w_{,r}(R)\right] = N_z - EZ_\epsilon + Kw_{,r}(R)$$
$$+EZr\left[\left(u_{,r}(R) + \tfrac{1}{2}w_{,r}(R)^2\right) - \nu\tfrac{1}{r}u(R)\right] \tag{4.70}$$

using the same scaling rules previously presented, the following non-dimensional boundary conditions are derived:

$$u_3(0) = 0,\ u_{3,\xi}(0) = 0$$
$$u_4(0) = 0,\ u_{4,\xi}(0) = 0 \tag{4.71}$$

$$v_3(0) = 0,\ v_{3,\xi}(0) = 0$$
$$v_4(0) = 0,\ v_{4,\xi}(0) = 0 \tag{4.72}$$

4-17

$$w_2(0) = 0$$

$$w_{2,\xi\xi}(0) = -Kw_{2,\xi}(0)$$

$$w_3(0) = 0$$

$$w_{3,\xi\xi}(0) = -Kw_{3,\xi}(0) - \frac{1}{\eta_1}EZ_{\epsilon 3} + (\xi w_{2,\xi\xi} - \nu w_{2,\xi})$$
$$- \frac{1}{\eta_1}EZ_2\left(u_{3,\xi} - \frac{1}{2}w_{2,\xi}^2\right) \tag{4.73}$$

$$w_4(0) = 0$$

$$w_{4,\xi\xi}(0) = -Kw_{4,\xi}(0) + [\xi w_{3,\xi\xi} - \nu w_{3,\xi}]$$
$$- \frac{1}{\eta_1}EZ_2\left[(u_{4,\xi} - \xi u_{3,\xi} - w_{2,\xi}w_{3,\xi}) + \nu u_3\right]$$

where it can again be seen that $EZ_{\epsilon 3}$ represents the non-dimensional moment imposed by the piezoelectric layer(s), and $N_z = 0$ using the neutral axis. This system represents the nonlinear equations of motion of a circular plate-membrane.

This system, represented by membrane equations in the 'outer' region and beam equations in the 'inner' region, is again linear at all levels, self-adjoint, and can be solved. Matching each level prior to solving the next level in the expansion provides a methodical approach to the problem.

The solution to the differential equation governing the behavior of the plate in the 'outer' region (Equation 4.57)

$$w_{2,00}^o - \nabla^2 w_2^o = 0 \tag{4.74}$$

can be represented as

$$w_2^o(r, T_0, T_1, T_2, \ldots) = a_0(T_1, T_2, \ldots) - \frac{P_2}{4}r^2$$
$$+ \sum_n \left[a_1(T_1, T_2, \ldots)\mathrm{J}_0(r\beta_n)\mathrm{e}^{i\beta_n T_0} + cc\right] \tag{4.75}$$

4-18

where the a_i terms represent constant terms with respect to the radial (r) and dominant time (T_0) variables. At this point they can be functions of the higher order time variables $(T_1, T_2, \ldots)$, however. The general solution includes Bessel functions of the first, J_i, and of the second, Y_i, kinds. The Bessel functions of the second kind have been discarded due to their non-finite values at the origin. The solution to the differential equation governing the behavior of the plate in the 'inner' region (Equation 4.65):

$$w_{2,\xi\xi\xi\xi}^i - w_{2,\xi\xi}^i = 0 \tag{4.76}$$

is

$$w_2^i(\xi, T_0, T_1, \ldots) = b_0(T_0, T_1, \cdots) + b_1(T_0, T_1, \cdots)\xi + b_2(T_0, T_1, \cdots)e^{-\xi} \tag{4.77}$$

where the b_i terms can be functions of time only. The positive exponential term is neglected since the inner solution would be unbounded otherwise. Applying the boundary conditions at this level:

$$w_2(0) = 0$$
$$w_{2,\xi\xi}(0) = -Kw_{2,\xi}(0)$$

the 'inner' solution becomes:

$$w_2^i(\xi, T_0, T_1, \ldots) = -b_2(T_0, T_1, \cdots)\left(1 - \frac{K-1}{K}\xi - e^{-\xi}\right). \tag{4.78}$$

Expanding the 'outer' solution with the 'inner' variable, and vice-versa, the boundary layer equation drops out $(w_2^i = 0)$. The complete solution of the second level expansion is:

$$
\begin{aligned}
w_2^o(r, T_0, T_1, T_2, \ldots) =& \frac{P_2}{4}\left(1 - r^2\right) \\
&+ \sum_n \left[a_1(T_1, T_2, \ldots)J_0(r\beta_n)e^{i\beta_n T_0} + cc\right]
\end{aligned}
\tag{4.79}
$$

4-19

where β_n are the zeros of the zeroth order Bessel function. To this point, only one unknown (a_1) remains at this level. This term will be calculated through a solvability condition at the next level.

At the next level, the in-plane displacement terms present themselves. Since, in the expansion, these terms are independent at this level, each can be solved independently. The solution to the differential equation governing the behavior of the radial displacement of the plate in the 'outer' region (Equation 4.53):

$$\nabla^2 u_3 - \frac{1}{r^2} u_3 = 0 \tag{4.80}$$

is

$$u_3^o(r, T_0, T_1, T_2, \ldots) = c_0(T_0, T_1, T_2, \ldots)r + \frac{1}{r} c_1(T_0, T_1, T_2, \ldots). \tag{4.81}$$

The corresponding 'inner' differential equation:

$$u_{3,\xi\xi} = \frac{1}{2} \left(w_{2,\xi}^2 \right)_{,\xi} \tag{4.82}$$

yields the following linear equation:

$$u_3^i(\xi, T_0, T_1, T_2, \ldots) = d_0(T_0, T_1, T_2, \ldots) + d_1(T_0, T_1, T_2, \ldots)\xi. \tag{4.83}$$

Applying the boundary conditions:

$$u_3(R) = 0, \, u_{3,\xi}(R) = 0,$$

both d_0 and d_1 are zero, indicating no boundary layer effect at this level within the plate. Matching the 'outer' and 'inner' equations eliminates each of the c_i variables also. Performing the same procedure also produces a trivial solution for the other in-plane displacement (v_3).

4-20

Solving the transverse displacement at this level (w_4) will yield solvability conditions completing the solution of the previous level. The solution to the differential equation governing the behavior of the plate in the 'outer' region at this level (Equation 4.58):

$$w_{3,00} - \nabla^2 w_3 = -2w_{2,01} - 2\omega_1 w_{2,00} - 2\mu_1 w_{2,0} \tag{4.85}$$

cannot be completed without removing the forcing terms which lie within the null-space of the homogenous adjoint solution of this system. These terms would produce non-secular behavior if ignored. The left-hand side of each differential equation is also the adjoint of this system. All forcing parameters on the right-hand side of each equation must be removed prior to solving each equation, thus producing a 'solvability equation' necessary to complete the analysis. The entire right-hand side of this equation above must be removed. Setting this system to zero, the following results

$$a_1(T_1, T_2, \ldots) = a_{11}(T_2, \ldots)e^{\gamma_1 T_1} \tag{4.86}$$

where

$$\gamma_1 = -\mu_1 - i\omega_1\beta_n. \tag{4.87}$$

The 'outer' solution is then

$$w_3^o(r, T_0, T_1, T_2, \ldots) = a_2(T_1, T_2, \ldots) + \sum_n \left[a_3(T_1, T_2, \ldots)J_0(r\beta_n)e^{i\beta_n T_0} + cc \right] \tag{4.88}$$

where the a_i terms represent constant terms with respect to the radial (r) and dominant time (T_0) variables, as before. The solution to the differential equation governing the behavior of the plate in the 'inner' region:

$$w_{3,\xi\xi\xi\xi} - w_{3,\xi\xi} = -\eta_1 \left[w_{2,\xi}\left(u_{3,\xi} - \frac{1}{2}w_{2,\xi}^2 \right) \right]_{,\xi} + w_{2,\xi\xi\xi} \tag{4.89}$$

4-21

is

$$w_3^i(\xi, T_0, T_1, \ldots) = b_3(T_0, T_1, \cdots) + b_4(T_0, T_1, \cdots)\xi + b_5(T_0, T_1, \cdots)e^{-\xi} \qquad (4.90)$$

where the constant terms (b_i) can be function of time only, as before. Applying the boundary conditions at this level:

$$w_3(0) = 0$$

$$w_{3,\xi\xi}(0) = -Kw_{3,\xi}(0) - \frac{1}{\eta_1}EZ_{\epsilon3} + (\xi w_{2,\xi\xi} - \nu w_{2,\xi}) - \frac{1}{\eta_1}EZ_2\left(u_{3,\xi} - \frac{1}{2}w_{2,\xi}^2\right)$$

the 'inner' solution becomes:

$$w_3^i(\xi, T_0, T_1, \ldots) = -\frac{1}{\eta_1 K}EZ_{\epsilon3}\xi - b_5(T_0, T_1, \cdots)\left(1 - \frac{K-1}{K}\xi - e^{-\xi}\right). \qquad (4.91)$$

Expanding the 'outer' solution with the 'inner' variable, and vice-versa, the boundary layer solution results. At this point we will consider the same time-varying actuation function with bias used in Chapter III:

$$
\begin{aligned}
EA_{\epsilon2} &= f_0 + f\sin[(\Omega + \varepsilon\delta)t] \\
&= f_0 + f\sin(\Omega T_0 + \delta T_1) \\
EA_{\epsilon z3} &= m_0 + m\sin[(\Omega + \varepsilon\delta)t] \\
&= m_0 + m\sin(\Omega T_0 + \delta T_1) \qquad (4.92)
\end{aligned}
$$

After applying Equation 4.92 to the system, the following results:

$$a_2 = \frac{K}{K-1}\left[\frac{m_0}{K} - \frac{P_2}{2}\right] \qquad (4.93)$$

$$\sum_n \left[a_1(T_1, T_2, \ldots)J_0(\beta_n)e^{i\beta_n T_0} + cc\right] = \frac{2m}{K}e^{i(\Omega T_0 + \delta T_1)}. \qquad (4.94)$$

Equation 4.94 is used to compute the actual displacement in w_2 produced for a given applied voltage and frequency. The results also provide the value of ω_1, the first order time correction

$$\omega_1 = -\frac{1}{\beta_n}\left(\delta - i\mu_1\right).\tag{4.95}$$

Continuing the procedure as previously demonstrated, the next level is solved to produce not only the next level solution, but also additional solvability conditions. Recognizing the dominance of the driving frequency, other modes will be neglected.

This research is concerned with both the dynamical properties of this material as well as its static shape manipulation capabilities. At this point, to study the shaping capabilities of the system, only the static solution in necessary.

4.2.1 Static Shaping.   Since the system is decoupled, and the in-plane solutions (u and v) have no affect through order $\sim \varepsilon^3$, only the transverse solution, w, will be discussed for the remainder of this chapter. We can solve the system of equations, using a two level matching, to find the following composite solution to order ε^4:

$$\begin{aligned}
w^c(r) &= \varepsilon^2 \frac{P_2}{2}\left(1 - r^2\right)\\
&\quad + \varepsilon^3 \left(\frac{K}{K-1}\left[\frac{P_2}{2} + \frac{EZ_{\epsilon 3}}{K}\right]\left(\mathrm{e}^{-\xi} - 1\right)\right)\\
&\quad + \varepsilon^4 \left(\frac{P_2}{4}\eta^2(1+\nu)EH_{\epsilon 2}\left(1 - r^2\right)\right)\\
&\quad + \varepsilon^4 \left(\frac{K}{K-1}\left[\frac{2K-3+2\nu}{K-1}\left(\frac{P_2}{2} + \frac{EZ_{\epsilon 3}}{K}\right) - \frac{EZ_{\epsilon 3}}{K^2}\right]\left(\mathrm{e}^{-\xi} - 1\right)\right)
\end{aligned}\tag{4.96}$$

Figure 4.1 illustrates the behavior of the piezoelectric laminate plate-membrane with a pressure differential and symmetric edge conditions. Consider a 15 cm diameter circular membrane with three laminate layers consisting of a Kapton base layer, and two layers of PVDF with the properties listed in Table 3.1 of Chapter III. Reasonable environmental and actuation values yield interesting results.
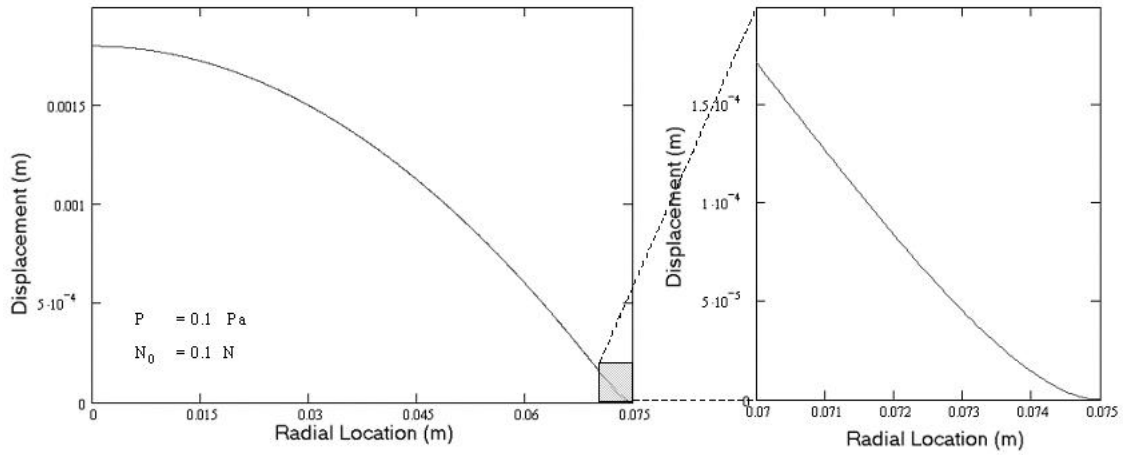
Figure 4.1   Axisymmetric Plate Deflection (Pressurized/No Voltage Applied)

(a)   (b)
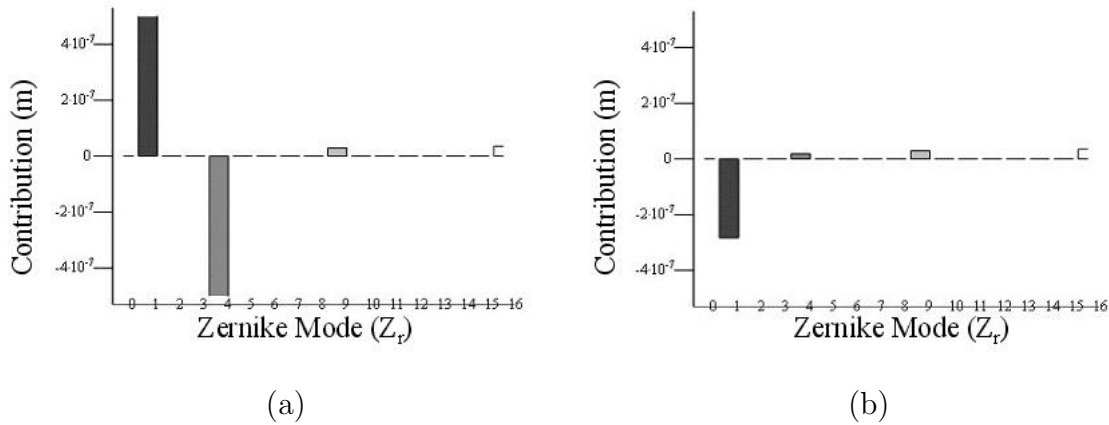
Figure 4.2   Axisymmetric Plate Zernike Deviations: (a) Pressurized/No Voltage
Applied (b) Change Due to 10 Volt Potential

A 10 volt actuation potential causes a small deviation in the center portion
of the plate totalling approximately one wavelength of visible light ($\sim 600nm$).
(Note: Materials currently available allow over 1000 volts.) Figure 4.2 illustrates
the change in the reflected wavefront. Both plots present the Zernike coefficients for
modes less than 17. Appendix A presents a short overview and graphic illustration
of the Zernike polynomial series. Figure 4.2 indicates, as expected, the reflected
wavefront is dominated by the axisymmetric modes. The right side of Figure 4.2 is
the change in the wavefront due to the boundary layer effects and actuation. The

4-24

effective boundary layer region is approximately of the order of $\sqrt{\varepsilon}$, as expected from the original mathematical foundation and is considered to have a small affect on the membrane away from this region. The dynamics of the plate are also effected.

4.2.2 **Dynamic Response.** As discussed earlier, applying the solvability conditions produces temporal adjustments (ω_i terms). The first two are presented here:

$$\omega_1 = \frac{1}{\beta_n}\left(\delta + i\mu_1\right) \tag{4.97}$$

$$\begin{aligned}
\omega_2 &= \frac{\mu_1}{\beta_n^2}\left[\frac{2\delta}{\beta_n} + \beta_n - 6\mu_1\beta_n - 8\right] \\
&\quad + \frac{i}{\beta_n}\left[\frac{2\delta^2}{\beta_n} + \beta_n^2\left(\beta_n^2 + EH_{\epsilon 2}\right)\right. \\
&\quad \left. -4\left(\delta^2 - \mu_1^2\right) + 6\mu_1\beta_n\delta + 2\beta_n\mu_1^2 + \beta_n\delta + \beta_n^2\mu_1\right].
\end{aligned} \tag{4.98}$$

Since time has been scaled as:

$$\omega = 1 + \varepsilon\omega_1 + \varepsilon^2\omega_2 + \cdots,$$

the real terms provide a direct method of computing the deviation of the modal frequencies from the linear case. The imaginary terms function as modifiers to the dissipation inherent in the material. As expected the amplitudes will not decay without damping, and the damping within the material is a direct cause of the modal frequency shift.

The coupled nonlinear equations of motion derived in this chapter represent the behavior of a piezothermoelastic laminated circular membrane. The development of the perturbation solution, based on axisymmetric assumptions, provides a solution for a laminated membrane made of piezothermoelastic material. The results illustrate the effectiveness of a Kapton/PVDF beam at optical wavelengths and is related to actual reflected wavefront displacements. The solutions in this chapter represent

4-25

the limit of the analytical approach. The next chapter presents a new mathematical approach to this problem which can produce solutions to more complicated systems.

V. Integral Multiple Scales

The perturbation method of multiple scales can be used to produce solutions of a certain class of differential equations. In particular, this method can produce the same result as the method of matched asymptotic expansions when a boundary layer effect is present. This chapter adapts this method to a new finite element approach. After presenting a short analytical linear beam-string example, a finite element approach is developed. This finite element method is applied to the linear string-beam, for which the closed-form solution is well known, and comparisons are made. This method will then be applied to the non-linear problems of interest in the next chapter.

5.1   Linear One-Dimensional Beam-String

Nayfeh (69) presented the linear beam-string problem using the method of matched asymptotic expansions. He also presented the solution of a boundary layer problem using multiple scales when a system has a single boundary layer (67). Here, the method of multiple scales is expanded to include multiple boundary layers. To develop the necessary fundamental equations needed in this analysis, the Lagrangian is needed. The potential energy of a clamped-clamped elastic beam, assuming plane sections remain plane, can be defined using the strain energy representation:

$$\hat{\mathbb{V}} = \frac{1}{2} \int_{\hat{\mathcal{V}}} E\hat{w}_{,\hat{x}}^2 - 2E\hat{z}\hat{w}_{,\hat{x}}\hat{w}_{,\hat{x}\hat{x}} + E\hat{z}^2\hat{w}_{,\hat{x}\hat{x}}^2 d\hat{\mathcal{V}} \tag{5.1}$$

As previously stated, all variables after a comma in the subscript indicate the derivative with respect to that variable. The beam's kinetic energy, ignoring rotatory

inertia, can be represented as:

$$\hat{\mathbb{T}} = \frac{1}{2} \int_{\hat{\mathcal{V}}} \rho \hat{w}_{,\hat{t}}^2 d\hat{\mathcal{V}} \tag{5.2}$$

where ρ is the beam's density. The transverse deflection is represented as w. The system's non-conservative work is a result from the follower pressure force and can be represented as

$$\hat{\mathbb{W}}_{nc} = - \int_{\hat{x}} \hat{P} \hat{w} d\hat{x}. \tag{5.3}$$

The simple beam's Lagrangian can then be compiled from Hamilton's principle

$$\int_{t_1}^{t_2} \delta \hat{\mathbb{T}} - \delta \hat{\mathbb{V}} + \delta \hat{\mathbb{W}}_{nc} dt = 0, \tag{5.4}$$

where δ indicates variation. This system's dimensional Lagragian, $\mathbb{L}$, representing the beam's energy is derived:

$$\hat{\mathbb{L}} = \frac{1}{2} \int_{\hat{\mathcal{V}}} \rho \hat{w}_{,\hat{t}}^2 - E\hat{w}_{,\hat{x}}^2 + 2E\hat{z}\hat{w}_{,\hat{x}}\hat{w}_{,\hat{x}\hat{x}} - E\hat{z}^2 \hat{w}_{,\hat{x}\hat{x}}^2 d\hat{\mathcal{V}} - \int_{\hat{x}} \hat{P}\hat{w} d\hat{x} \tag{5.5}$$

with clamped boundary conditions, where the hats $\hat{()}$ represent the dimensional values.

The equation of motion for this system can be quickly verified as

$$\rho A \hat{w}_{\hat{t}\hat{t}} + EI\hat{w}^{IV} - EA\hat{w}'' = -\hat{P}, \tag{5.6}$$

which is the dynamic Bernoulli-Euler beam equation. Applying the scaling relations: $w = \hat{w}/L$, $z = \hat{z}/L$, $x = \hat{x}/L$, $dx = d\hat{x}/L$, and:

$$\varepsilon^2 = \frac{EI}{EAL^2}, \quad P(x) = \frac{\hat{P}L}{EA}, \quad t = \sqrt{\frac{\rho AL^2}{EA}} \hat{t} \tag{5.7}$$

to Equation 5.5, where L is the length of the beam, and ε which is the scaled radius of gyration of the beam and represents the 'smallness' parameter which lends this system to perturbation solution methods, produces:

$$\mathbb{L} = \int_x \frac{1}{2}w_{,t}^2 - \frac{1}{2}w,x^2 + EA_z w_{,x}w_{,xx} - \frac{1}{2}\varepsilon^2 w_{,xx}^2 - Pw\,dx \qquad (5.8)$$

Performing a standard matched asymptotic expansion of this system yields the following static solution (69)

$$w^c = \frac{P}{2}(x - x^2) - \varepsilon\left[\frac{P}{2}\left(1 - \mathrm{e}^{-\xi} - \mathrm{e}^{-\zeta}\right)\right] \qquad (5.9)$$

where

$$\xi = \frac{x}{\varepsilon}, \ \zeta = \frac{1-x}{\varepsilon}. \qquad (5.10)$$

The EA_z term drops out of the solution as the variation of the Lagrangian is evaluated. Based on the discussions in Chapter III, $EA_z = 0$ for a symmetric beam. Therefore, this term will be neglected for the remainder of this chapter.

Figure 5.1 illustrates the beam-string deflection and the effect of the 'smallness' factor on the solution. The region where the beam-like behavior occurs is near the ends, in the boundary layers. The length of this area is roughly on the order of $\sqrt{\varepsilon}$ which is therefore directly related to the beam's thickness to length ratio. We can clearly see the dramatic impact this value has on the solution. It's important to note that the region of validity is finite. An initial assumption was that ε was very small. As ε increases, the solution begins to break down as the boundary layer effects begin to interact. This is a common limitation of all perturbation methods.

Equation 5.8 produces a beam-string solution. Near its ends, it exhibits beam-like behavior, and in the center region it acts like a string. This suggests a spatial multiple scales application may be appropriate. Multiple scales is commonly applied to differential equations of motion resulting from application of variational principles.
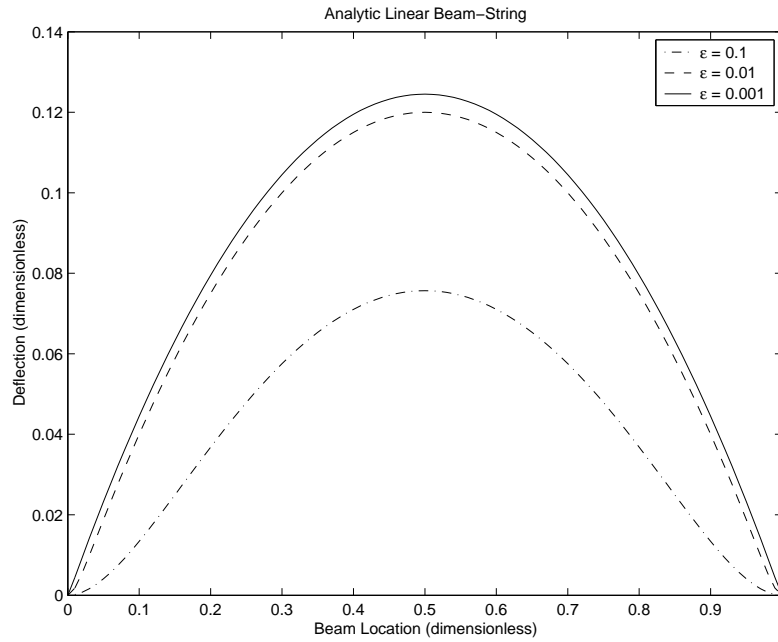
Figure 5.1   Analytic Beam-String Solution (P=1)

Why not apply multiple scales directly to the Lagrangian? The result would be an integrated solution.

5.2   Integral Multiple Scales

The procedure begins by introducing three scales: $\eta = x$, $\xi = \frac{x}{\varepsilon}$, and $\zeta = \frac{1-x}{\varepsilon}$. The primary assumption with the method of multiple scales is that these scales are considered independent (67). The method introduced here relies on this assumption.

Applying the chain rule to $x = x(\eta, \xi, \zeta; \varepsilon)$, the following differentials are produced:

$$\frac{d}{dx} = \frac{\partial}{\partial \eta} + \frac{1}{\varepsilon}\left[\frac{\partial}{\partial \xi} - \frac{\partial}{\partial \zeta}\right] \tag{5.11}$$

$$\frac{d^2}{dx^2} = \frac{\partial^2}{\partial \eta^2} + \frac{2}{\varepsilon}\left[\frac{\partial^2}{\partial \xi \partial \eta} - \frac{\partial^2}{\partial \zeta \partial \eta}\right] + \frac{1}{\varepsilon^2}\left[\frac{\partial^2}{\partial \xi^2} + \frac{\partial^2}{\partial \zeta^2} - 2\frac{\partial^2}{\partial \xi \partial \zeta}\right] \tag{5.12}$$

5-4

Substituting Equation 5.12 into Equation 5.8 produces the multiple scale representation of the beam-string's Lagrangian ($w(x) = w(\eta, \xi, \zeta; \varepsilon)$):

$$\mathbb{L} = \int_x \frac{1}{2} w_{,t}^2 - \frac{1}{2} \left[w_{,\eta} + \frac{1}{\varepsilon} (w_{,\xi} - w_{,\zeta}) \right]^2 \\ - \varepsilon^2 \frac{1}{2} \left[w_{,\eta\eta} + \frac{2}{\varepsilon} (w_{,\xi\eta} - w_{,\zeta\eta}) + \frac{1}{\varepsilon^2} (w_{,\xi\xi} + w_{,\zeta\zeta} - 2w_{,\xi\zeta}) \right]^2 - Pw \, dx \tag{5.13}$$

Next, substituting the expansions:

$$t = \omega\tau \tag{5.14}$$

$$T_n = \varepsilon^n \tau \tag{5.15}$$

$$\omega = \omega_0 + \varepsilon\omega_1 + \varepsilon^2\omega_2 + \cdots \tag{5.16}$$

$$w(\eta, \xi, \zeta, t; \varepsilon) = w_0(\eta, \xi, \zeta, t) + \varepsilon w_1(\eta, \xi, \zeta, t) + \varepsilon^2 w_2(\eta, \xi, \zeta, t) + \cdots \tag{5.17}$$

where $\omega_0 = 1$ as the original system was effectively scaled by ω_0, into Equation 5.13. The Lagrangian can now be organized into increasing orders of ε:

$$\mathbb{L} = \varepsilon^{-2} \mathbb{L}_{-2} + \varepsilon^{-1} \mathbb{L}_{-1} + \mathbb{L}_0 + \varepsilon \mathbb{L}_1 + \varepsilon^2 \mathbb{L}_2 + \cdots \tag{5.18}$$

where

$$\mathbb{L}_{-2} = \int_x \frac{1}{2} F_0^2 + \frac{1}{2} G_0^2 \, dx \tag{5.19}$$

$$\mathbb{L}_{-1} = \int_x F_0 F_1 + G_0 G_1 \, dx \tag{5.20}$$

$$\mathbb{L}_0 = \int_x \frac{1}{2} F_1^2 + F_0 F_2 + \frac{1}{2} G_1^2 + G_0 G_2 - Pw_0 + \frac{1}{2} w_{0,0}^2 \, dx \tag{5.21}$$

$$\vdots$$

and

$$F_i = w_{i,\xi\xi} + w_{i,\zeta\zeta} - w_{i,\xi\zeta} + 2\left((w_{i-1,\xi\eta} - w_{i-1,\zeta\eta}) + w_{i-2,\eta\eta}\right)$$
$$G_i = w_{i,\xi} - w_{i,\zeta} + w_{i-1,\eta}.$$

(5.22)

Applying variational principles to each $\mathbb{L}_i$ produces

$$\mathbb{L}_{-2}: \quad \nabla^2\left[\nabla^2 w_0 - w_0\right] = 0 \tag{5.23}$$

$$\mathbb{L}_{-1}: \quad \nabla^2\left[\nabla^2 w_0 - w_0\right] = 0 \tag{5.24}$$

$$\nabla^2\left[\nabla^2 w_1 - w_1\right] = -\nabla\left[4\nabla^2 w_0 - 2w_0\right]_{,\eta}$$

$$\mathbb{L}_0: \quad \nabla^2\left[\nabla^2 w_0 - w_0\right] = 0 \tag{5.25}$$

$$\nabla^2\left[\nabla^2 w_1 - w_1\right] = -\nabla\left[4\nabla^2 w_0 - 2w_0\right]_{,\eta}$$

$$\nabla^2\left[\nabla^2 w_2 - w_2\right] = -\nabla\left[4\nabla^2 w_1 - 2w_1\right]_{,\eta} - \left[6\nabla^2 w_0 - w_0\right]_{,\eta\eta} - w_{0,00} - P$$

$$\vdots$$

where

$$\nabla = \frac{\partial}{\partial\xi} - \frac{\partial}{\partial\zeta}$$
$$\nabla^2 = \frac{\partial^2}{\partial\xi^2} + \frac{\partial^2}{\partial\zeta^2} - 2\frac{\partial^2}{\partial\xi\partial\zeta}.$$

(5.26)

Notice all lower solutions exist within each successive level. This allows selection of the desired level of precision at the beginning of the solution method. Therefore, if the desired solution is to be to order ε^2, select $\mathbb{L}_2$ and apply the desired variational principles. Applying Euler's equations to $\mathbb{L}_2$, the following system of

5-6

equations is produced:

$$\nabla^2 \left[\nabla^2 w_0 - w_0 \right] = 0 \tag{5.27}$$

$$\nabla^2 \left[\nabla^2 w_1 - w_1 \right] = -\nabla \left[4\nabla^2 w_0 - 2w_0 \right]_{,\eta} \tag{5.28}$$

$$\nabla^2 \left[\nabla^2 w_2 - w_2 \right] = -\nabla \left[4\nabla^2 w_1 - 2w_1 \right]_{,\eta} - \left[6\nabla^2 w_0 - w_0 \right]_{,\eta\eta}$$
$$- w_{0,00} - P \tag{5.29}$$

$$\nabla^2 \left[\nabla^2 w_3 - w_3 \right] = -\nabla \left[4\nabla^2 w_2 - 2w_2 \right]_{,\eta} - \left[6\nabla^2 w_1 - w_1 \right]_{,\eta\eta}$$
$$- \left[4\nabla w_0 \right]_{,\eta\eta\eta} - 2w_{0,01} - w_{1,00} - 2\omega_1 w_{0,00} \tag{5.30}$$

$$\nabla^2 \left[\nabla^2 w_4 - w_4 \right] = -\nabla \left[4\nabla^2 w_3 - 2w_3 \right]_{,\eta} - \left[6\nabla^2 w_2 - w_2 \right]_{,\eta\eta}$$
$$- \left[4\nabla w_1 \right]_{,\eta\eta\eta} - w_{0,\eta\eta\eta\eta} - w_{0,11} - 2w_{0,02} - 2w_{1,01}$$
$$- w_{2,00} - 2\omega_1 w_{1,00} - 2\omega_2 w_{0,00} - \omega_1^2 w_{0,00} \tag{5.31}$$

The system can be solved in successive layers from Equation 5.27 to Equation 5.31. Removing all time-based derivatives, a static solution can be attained. The static solution of Equation 5.27 is:

$$w_0(\eta, \xi, \zeta) = a_0(\eta) + a_1(\eta) e^{-\xi} + a_2(\eta) e^{-\zeta} \tag{5.32}$$

where the positive exponential and linear terms have already been removed since as $\varepsilon \to 0$, the solution must be finite. Applying this result to the next equation produces:

$$\nabla^2 \left[\nabla^2 w_1 - w_1 \right] = -\nabla \left[4\nabla^2 w_0 - 2w_0 \right]_{,\eta}$$
$$= 2 \left[a_{1,\eta} e^{-\xi} + a_{2,\eta} e^{-\zeta} \right] \tag{5.33}$$

The right-hand side of this equation must be zero to eliminate possible secular terms. This requires a_1 and a_2 not to be functions of η, which means they must be constant values. With the clamped boundary conditions, these terms are eliminated, leaving

only the $a_0(\eta)$ term. Therefore, no boundary layer exists at this level. This term can be completed in the next level. The solution of Equation 5.28 is then:

$$w_1(\eta, \xi, \zeta) = b_0(\eta) + b_1(\eta)\mathrm{e}^{-\xi} + b_2(\eta)\mathrm{e}^{-\zeta}. \qquad (5.34)$$

Successive levels are solved to produce the level of precision desired. The entire solution is not continued here, but it's simple to verify the original solution produced through the matched-asymptotic expansion method (Equation 5.9) satisfies this system. While even this most trivial example proves to be challenging to solve analytically, this methodical approach can take advantage of computational techniques and be applied to a finite element method.

5.3 Finite Element Approach

A typical finite element approach begins by substituting an assumed shape function vector and an unknown displacement vector into the energy equation. Applying Euler's equations, or variational methods, would produce the finite element system which can be used to model the system in question. To apply this methodology to the linear beam-string discussed in this chapter, we substitute the shape function vector and displacement vector into Equation 5.8:

$$w(x, t) = \{N(x)\}\{d(t)\} \qquad (5.35)$$

where $\{N(x)\}_{1 \times n}$ is the assumed shape function vector, and $\{d(t)\}_{n \times 1}$ is the elemental displacement vector to be computed, producing:

$$\begin{aligned} \mathbb{L} = \int_x &\frac{1}{2}\{d_{,t}\}^T\{N\}^T\{N\}\{d_{,t}\} - \frac{1}{2}\varepsilon^2\{d\}^T\{N_{,xx}\}^T\{N_{,xx}\}\{d\} \\ &- \frac{1}{2}\{d\}^T\{N_{,x}\}^T\{N_{,x}\}\{d\} - P\{N\}\{d\}dx. \end{aligned} \qquad (5.36)$$

The Lagrangian in Equation 5.36 is now only a function of one independent variable, t. Taking the variation of Equation 5.36, applying the integration, and rearranging the system, we can arrive at the standard dynamical finite element equations:

$$[M]\{d_{,tt}\} + [K]\{d\} = \{\Gamma\} \tag{5.37}$$

$$[M] = \int_x \{N\}^T\{N\}dx \tag{5.38}$$

$$[K] = \int_x \{N_{,x}\}^T\{N_{,x}\} + \varepsilon^2\{N_{,xx}\}^T\{N_{,xx}\}dx \tag{5.39}$$

$$\{\Gamma\} = -\int_x P\{N\}^T dx \tag{5.40}$$

where $[M]_{n\times n}$ and $[K]_{n\times n}$ are the system matrices. As ε approaches zero, the behavior approaches that of a string, and locking may occur. To counter this problem, an increase in the number of elements might improve stability, but will quickly increase the solution time. This is a byproduct of the assumed shapes of the displacement. If the material being modelled behaves as a beam-string, the shape functions should behave as beam-strings.

Previous discussions illustrate how a beam with extremely low bending stiffness only behaves as a beam near the point where the force or moment is applied. It behaves as a string elsewhere. Appendix B presents the development of a set of asymptotic shape functions which can be used in the following finite element approach. The asymptotic shape functions are beam-strings.

5.3.1 Finite Element Expansion. Substituting Equations 5.16, 5.17 and

$$\begin{aligned}
\{N\} &= \{N_0\} + \varepsilon\{N_1\} + \varepsilon^2\{N_2\} + \varepsilon^3\{N_3\} + \cdots \\
\{d\} &= \{d_0\} + \varepsilon\{d_1\} + \varepsilon^2\{d_2\} + \varepsilon^3\{d_3\} + \cdots
\end{aligned} \tag{5.41}$$

into Equation 5.13, and separating orders of ε, an energy expansion can be created:

$$\mathbb{L} = \varepsilon^{-2}L_{-2} + \varepsilon^{-1}L_{-1} + L_0 + \varepsilon L_1 + \varepsilon^2 L_2 + \cdots \qquad (5.42)$$

As discussed in section 5.2, selecting the order of precision is equivalent to selecting the Lagrangian order component. All vector brackets ({ }) and matrix brackets ([ ]) will no longer be carried as the reader should recognize the difference between scalars, vectors, and matrices. Applying Euler's equations to the individual $\mathbb{L}_i$ terms produces:

$$\mathbb{L}_{-2}: \qquad K_{-2}d_0 = 0 \qquad (5.43)$$

$$\mathbb{L}_{-1}: \qquad K_{-2}d_0 = 0 \qquad (5.44)$$
$$K_{-2}d_1 = -K_{-1}d_0$$

$$\mathbb{L}_0: \qquad K_{-2}d_0 = 0 \qquad (5.45)$$
$$K_{-2}d_1 = -K_{-1}d_0$$
$$K_{-2}d_2 = -K_{-1}d_1 - \Gamma_0 - M_0\ddot{w}_0 - K_0 d_0$$
$$\vdots$$

where

$$K_{-2} = \int_x \quad G_0^T G_0 + F_0^T F_0 \, dx \qquad (5.46)$$

$$K_{-1} = \int_x \quad G_0^T G_1 + G_1^T G_0 + F_0^T F_1 + F_1^T F_0 \, dx \qquad (5.47)$$

$$K_0 = \int_x \quad G_1^T G_1 + G_0^T G_2 + G_2^T G_0 + F_1^T F_1 + F_0^T F_2 + F_2^T F_0 \, dx \qquad (5.48)$$

$$\Gamma_0 = \int_x \quad F_1^T \, dx \qquad (5.49)$$

$$M_0 = \int_x \quad N_0^T N_0 \, dx \qquad (5.50)$$

and

$$F_i = [N_{i,\xi\xi} + N_{i,\zeta\zeta} - N_{i,\xi\zeta} + 2(N_{i-1,\xi\eta} - N_{i-1,\zeta\eta}) + N_{i-2,\eta\eta}]$$
$$G_i = [N_{i,\xi} - N_{i,\zeta} + N_{i-1,\eta}]$$

(5.51)

As seen before, all lower order equations exist in each Lagrangian element. This means the functions produced through the application of Euler's equations to $\mathbb{L}_n$ exists in the set of functions produced through the application of Euler's equations to $\mathbb{L}_m$, where $m > n$.

To produce a solution through order ε^2, Euler's equations are applied to term $\mathbb{L}_2$ producing the following system of equations:

$$K_{-2}d_0 = 0 \tag{5.52}$$

$$K_{-2}d_1 = -K_{-1}d_0 \tag{5.53}$$

$$K_{-2}d_2 = -K_{-1}d_1 - \Gamma_0 - M_0\ddot{w}_0 - K_0d_0 \tag{5.54}$$

$$K_{-2}d_3 = -K_{-1}d_2 - \Gamma_1 - M_0\ddot{w}_1 - K_0d_1 - \omega_1 M_0\ddot{d}_0 - M_1\ddot{d}_0 - K_1d_0 \tag{5.55}$$

$$K_{-2}d_4 = -K_{-1}d_3 - \Gamma_2 - M_0\ddot{d}_2 - K_0d_2 - \omega_1 M_0\ddot{d}_1 - M_1\ddot{d}_1 - K_1d_1$$
$$- \omega_1 M_1\ddot{d}_0 - \omega_2 M_0\ddot{d}_0 - \omega_1^2 M_0\ddot{d}_0 - M_2\ddot{d}_0 - K_2d_0 \tag{5.56}$$

where

$$K_{-2} = \int_x \; G_0^T G_0 + F_0^T F_0 \, dx \tag{5.57}$$

$$K_{-1} = \int_x \; G_0^T G_1 + G_1^T G_0 + F_0^T F_1 + F_1^T F_0 \, dx \tag{5.58}$$

$$K_0 = \int_x \; G_1^T G_1 + G_0^T G_2 + G_2^T G_0 + F_1^T F_1 + F_0^T F_2 + F_2^T F_0 \, dx \tag{5.59}$$

$$K_1 = \int_x \; G_0^T G_3 + G_3^T G_0 + G_2^T G_1 + G_1^T G_2 + F_0^T F_3 + F_3^T F_0$$
$$+ F_2^T F_1 + F_1^T F_2 \, dx \tag{5.60}$$

$$K_2 = \int_x \; G_2^T G_2 + G_1^T G_3 + G_3^T G_1 + G_0^T G_4 + G_4^T G_0 + F_2^T F_2$$
$$+ F_1^T F_3 + F_3^T F_1 + F_0^T F_4 + F_4^T F_0 \, dx \tag{5.61}$$

$$\Gamma_0 = \int_x \ PN_0^T dx \tag{5.62}$$

$$\Gamma_1 = \int_x \ PN_1^T dx \tag{5.63}$$

$$\Gamma_2 = \int_x \ PN_2^T dx \tag{5.64}$$

$$M_0 = \int_x \ N_0^T N_0 dx \tag{5.65}$$

$$M_1 = \int_x \ N_0^T N_1 + N_1^T N_0 dx \tag{5.66}$$

$$M_2 = \int_x \ N_1^T N_1 + N_0^T N_2 + N_2^T N_0 dx \tag{5.67}$$

and F_i and G_i are defined in Equation 5.51.

As discussed earlier in the chapter, the fundamental assumption to the method of multiple scales is the independence of the scales (i.e. η, ξ, ζ). From an energy perspective, this can be viewed as the energy in the region of dominance for each variable dominates the energy integral. The conjecture here is the integral bounds can be transformed as

$$\int_x f(x)dx = \int_\zeta \int_\xi \int_\eta f(\eta, \xi, \zeta)d\eta d\xi d\zeta. \tag{5.68}$$

The validity of this statement can be evaluated best through evaluation of the results when applied to the example beam. Equations 5.57 and 5.58 represent the first solvability equations in the analysis. Since d_0 is arbitrary, the system matrix K_{-2} must be trivial. Since K_{-2} represents the sum of the outer products of G_0 and F_0, N_0 must be only a function of η. The shape functions presented in Appendix B satisfy this requirement. Imposing these solvability conditions, the following system

of equations remain:

$$M_0\ddot{d}_0 + K_0 d_0 = -\Gamma_0 \tag{5.69}$$

$$M_0\ddot{d}_1 + K_0 d_1 = -\Gamma_1 - [2\omega_1 M_0 + M_1]\ddot{d}_0 - K_1 d_0 \tag{5.70}$$

$$M_0\ddot{d}_2 + K_0 d_2 = -\Gamma_2 - [2\omega_1 M_0 + M_1]\ddot{d}_1 - K_1 d_1$$
$$- \left[\left(2\omega_2 + \omega_1^2\right) M_0 + 2\omega_1 M_1 + M_2\right]\ddot{d}_0 - K_2 d_0 \tag{5.71}$$

which represent the asymptotic finite element equations of motion of the linear beam string presented earlier in this chapter.

5.3.2 Static Beam Results.
Neglecting dynamic terms, the static shape modeling capability of this system can be evaluated. Applying the desired shape functions to this system and compiling the global stiffness matrices for a desired grid, the beam's shape can be predicted by applying the following procedure:

$$d_0 = -K_0^{-1}\Gamma_0 \tag{5.72}$$

$$d_1 = -K_0^{-1}\left[\Gamma_1 + K_1 d_0\right] \tag{5.73}$$

$$d_2 = -K_0^{-1}\left[\Gamma_2 + K_1 d_1 + K_2 d_0\right] \tag{5.74}$$

$$d = d_0 + \varepsilon d_1 + \varepsilon^2 d_2. \tag{5.75}$$

Each successive level of d_i corrects the fundamental d_0 shape. Since each i level, $i = 1..n$, is of the order of ε^i, the order of the system can be matched to the desired precision of the output.

Equation 5.75 is a function of ε. To correctly produce a finite element solution, this value must be integrated into the system matrices. Beginning with Equation

5.75, the equivalent displacement equation is then:

$$\hat{d} = \hat{d}_0 + \hat{d}_1 + \hat{d}_2 \tag{5.76}$$

where

$$\begin{aligned} \hat{d}_0 &= d_0 \\ \hat{d}_1 &= \varepsilon d_1 \\ \hat{d}_2 &= \varepsilon^2 d_2. \end{aligned} \tag{5.77}$$

Multiplying the corresponding power of ε through Equations 5.72-5.74, produces

$$\begin{aligned} \hat{d}_0 &= \hat{K}_0^{-1}\hat{\Gamma}_0 \\ \hat{d}_1 &= \hat{K}_0^{-1}\left[\hat{\Gamma}_1 - \hat{K}_1\hat{d}_0\right] \\ \hat{d}_2 &= \hat{K}_0^{-1}\left[\hat{\Gamma}_2 - \hat{K}_1\hat{d}_1 - \hat{K}_2\hat{d}_0\right] \end{aligned} \tag{5.78}$$

where

$$\begin{aligned} \hat{K}_0 &= K_0 & \hat{\Gamma}_0 &= \Gamma_0 \\ \hat{K}_1 &= \varepsilon K_1 & \hat{\Gamma}_1 &= \varepsilon\Gamma_1 \\ \hat{K}_2 &= \varepsilon^2 K_2 & \hat{\Gamma}_2 &= \varepsilon^2\Gamma_2 \end{aligned} \tag{5.79}$$

The completed solution is then

$$w = \left(N_0 + \varepsilon N_1 + \varepsilon^2 N_2 + \cdots\right)\hat{d} \tag{5.80}$$

where ε, in this case, is the elemental parameter.

The displacements are directly effected by the choice of the shape functions. The two shape function expansions developed in Appendix B satisfy the solvability conditions and can be used in this formulation.

5-14
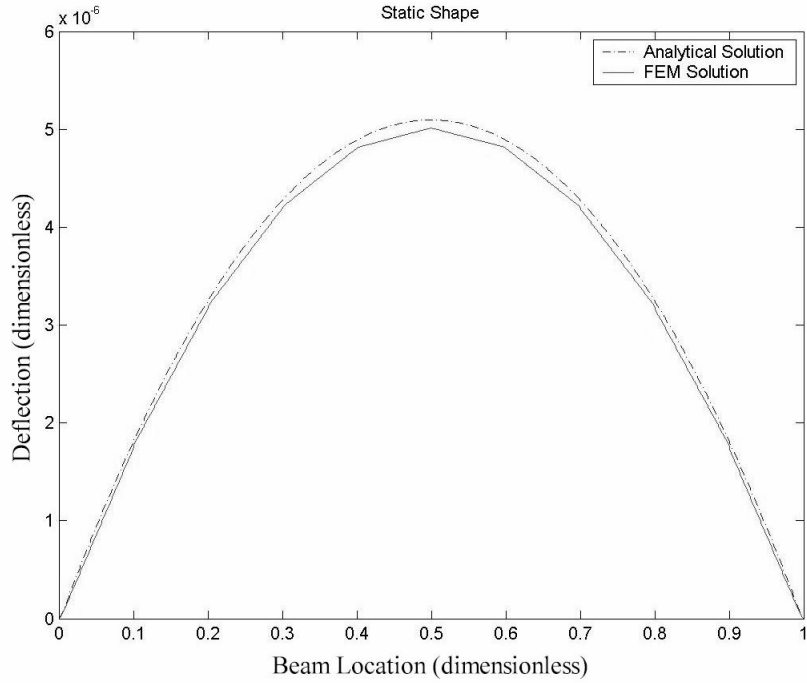
Figure 5.2   Beam Simulation using Linear C^1 Elements

Property	Value
Young's Modulus (E)	406 ksi
Thickness Ratio (t/L)	0.006
Pressure Differential (P)	0.1 lbs/in

Table 5.1   Linear Beam Element Properties

5-15
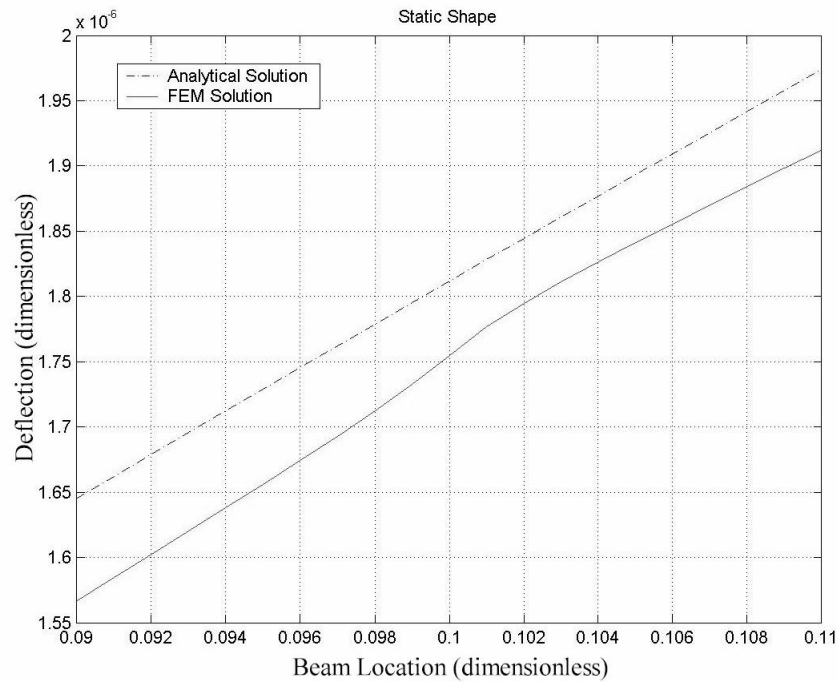
Figure 5.3   Linear C^1 Element Interface

5.3.2.1   *Linear C^1 Shape Function Results.*   If Linear C^1

shape functions are selected for this system (Equation B.9), an initial evaluation

of the validity of this method can be performed. Figure 5.2 illustrates a selected

result from applying a 10 element grid to a beam with properties outlined in Table

5.1. The smooth curve on top is the analytical prediction, while the 'bumpy' lower

curve in the prediction from the finite element procedure using the Linear C^1 shape

functions. The predicted shape error indicates an increased stiffness prediction, but

these elements may provide an alternative to simple rod or string (C^0) elements.

While the center portion of each element is incapable of modeling any curvature, as

discussed earlier, the shape does closely follow the analytical shape prediction.

The interface regions between each element is of interest. Figure 5.3 shows

that while the shape is smooth, unlike a C^0 model, the curvature changes in the

interface regions cause concern. The upper curve is the analytical prediction. The

lower finite element prediction remains below the analytical prediction and has a

5-16
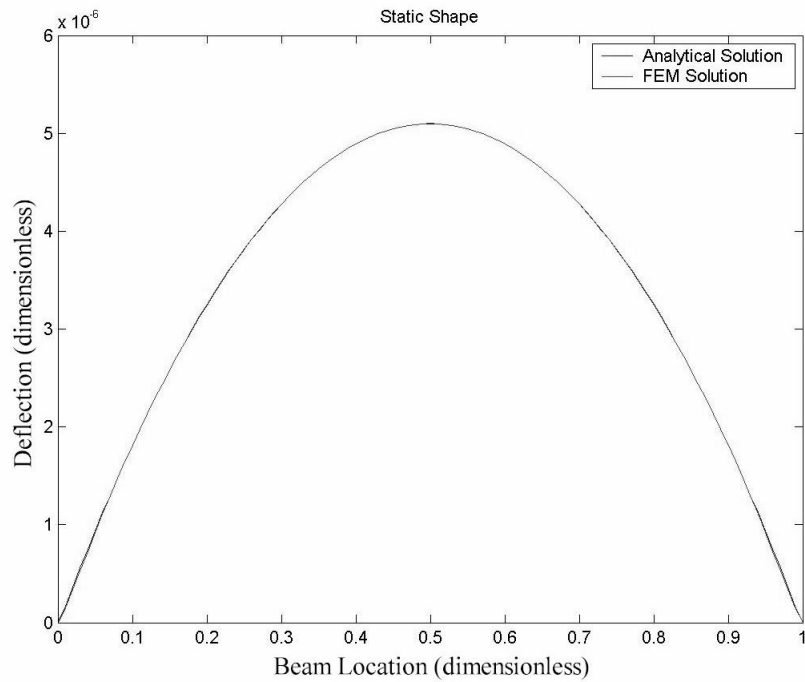
Figure 5.4   Beam Simulation using Cubic C^1 Elements

significant curvature change near the interface in the center of the figure. It's believed this might be a byproduct of the systems inability to handle the curvature changes anywhere but in the narrow boundary region of each element. If a better prediction is required, the Cubic C^1 shape functions allow internal curvature and could be used.

5.3.2.2   Cubic C^1 Shape Function Results.   While the Linear C^1 elements provided a string like element behavior, a better approximation can be attained using Cubic C^1 shape functions (Equation B.13). Figure 5.4 illustrates a selected result from applying the same 10 element grid to a beam with the same properties used in the last section (Table 5.1). These elements appear to provide a much better approximation than the Linear C^1 elements.

Figure 5.5 shows the clamped end of the beam indicating a close fit to the analytical solution. While the element can't quite match the curvature predicted by the analytical result, the interface between each element (Figure 5.6) indicates an

5-17
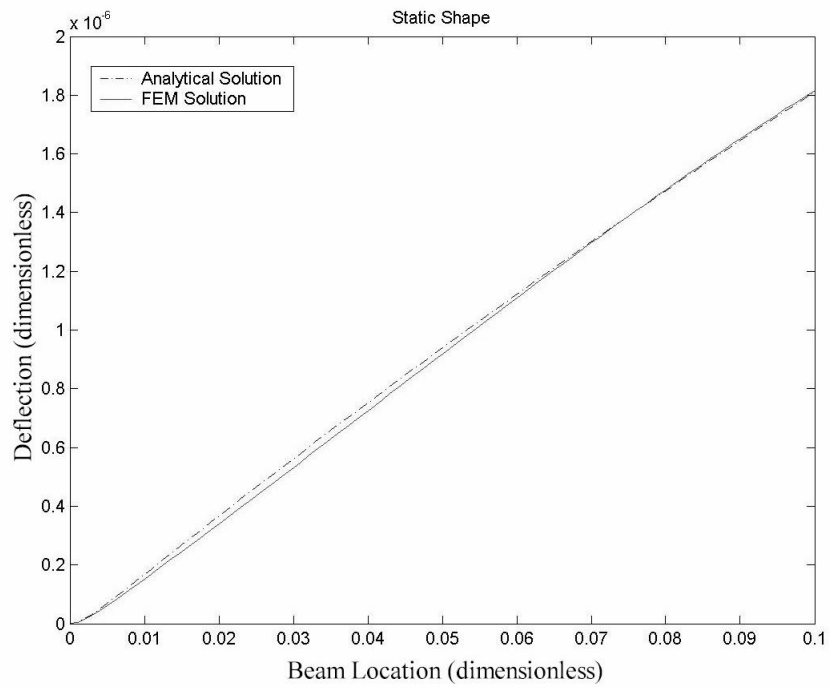
Figure 5.5   Cubic C^1 Element Beam Edge
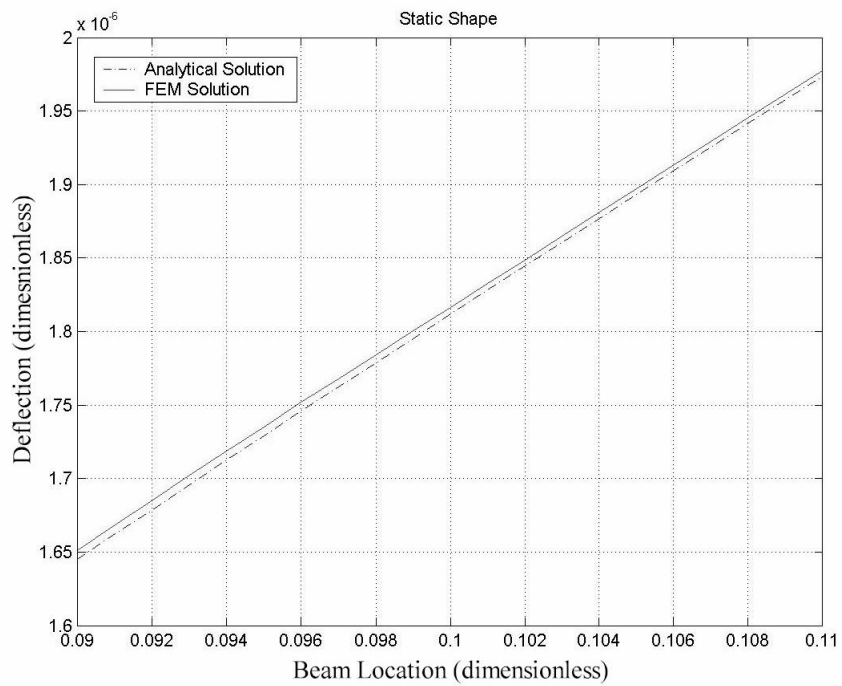
Figure 5.6   Cubic C^1 Element Interface

5-18
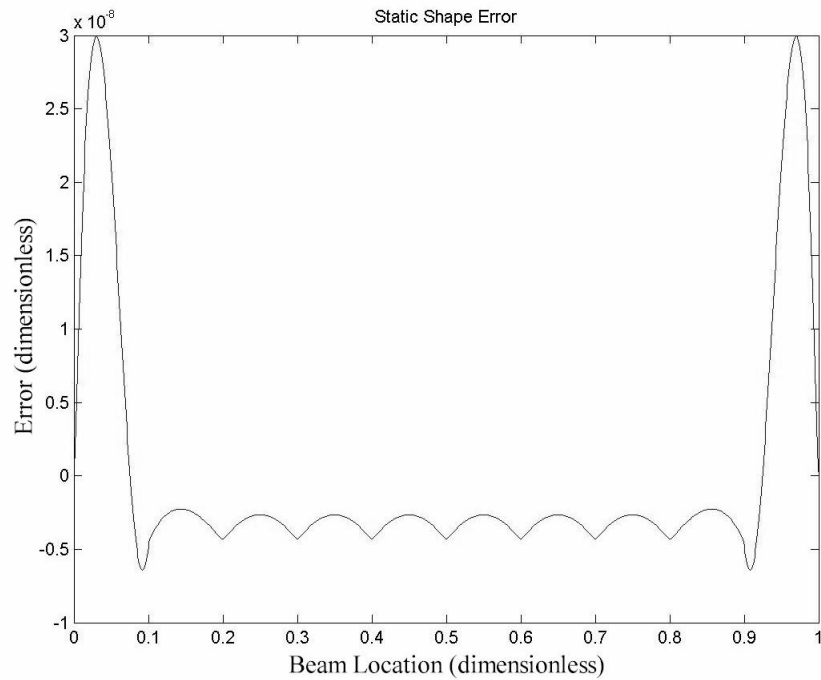
Figure 5.7   Cubic C^1 Element Beam Error

excellent fit to the analytical solution. Boundary layer effects within the element shape functions disappear in the solution. It appears the use of the Cubic C^1 shape functions provide a much better approximation of the beam's true stiffness. Figure 5.7 illustrates the error across this beam model. The error is small, but the beam edge regions indicate possible areas of concern which appear to be a result of a boundary layer conflict between the analytical and finite element solutions.

To see the significant improvement this method provides, Figures 5.8 and 5.9 compare the MIMS result error using Cubic C^1 elements to the standard finite element method error using standard C^1 elements. Both are measured against the analytical solution. Identical material properties and gridding were selected. While the standard model appears to produce a smoother result, the MIMS result is over 3 orders of magnitude more accurate.
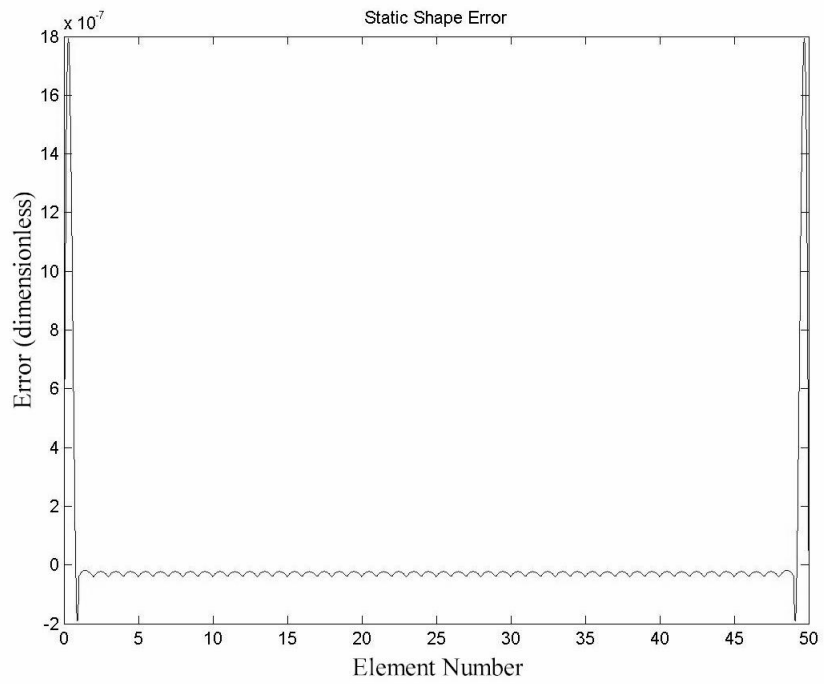
Figure 5.8   Cubic C^1 Element Beam Error - 50 Elements
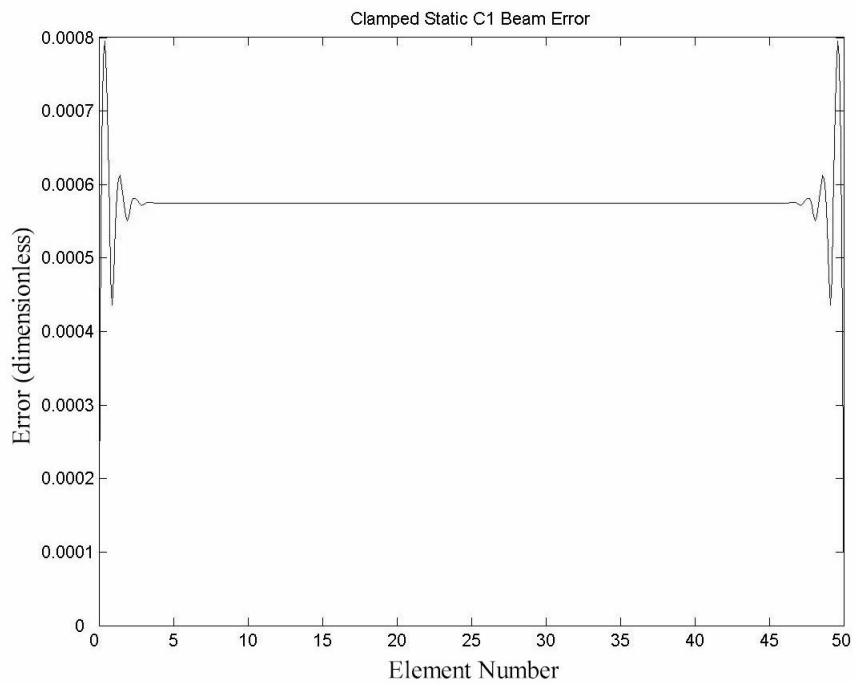
Figure 5.9   Standard C^1 Element Beam Error - 50 Elements

5-20
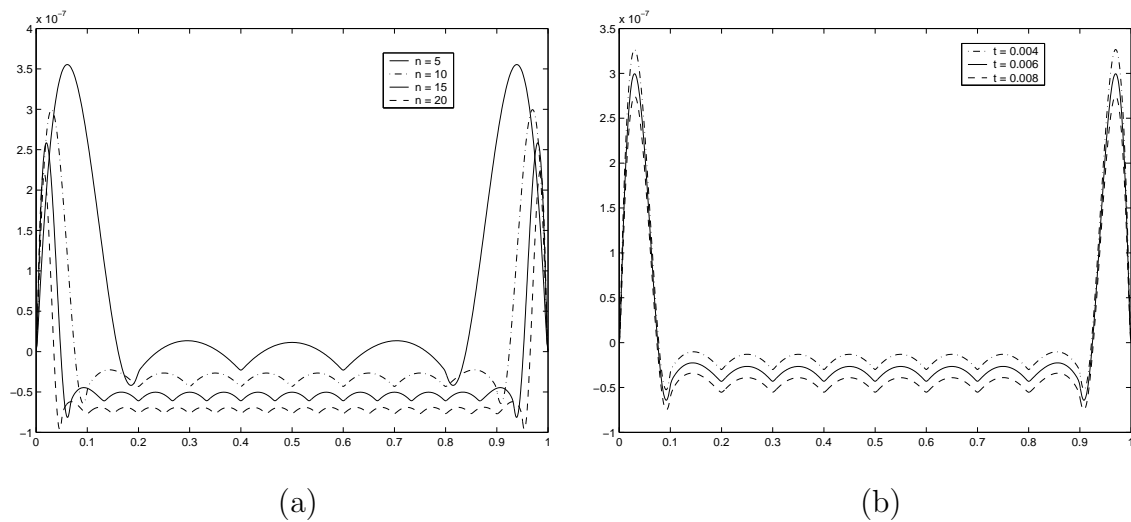
Figure 5.10   Cubic C^1 Error Examples: (a) Grid Size Effects (b) Thickness Effects

As the grid size is increased, it is important to not get too close to the global boundary layer, approximated by the square root of the beam's radius of gyration, within the system. Figure 5.10 shows how increasing the number of elements causes the center region of the model to deviate from the analytic prediction. This same effect is realized by increasing the thickness ratio of the beam. This appears to be an indication of 'boundary layer encroachment'. As the thickness of the beam is reduced, the effect of grid size is less noticeable. To better visualize the boundaries of this method, analysis of extreme parameter values will more clearly present the bounds of this method.

Figure 5.11 presents an analysis of beam thickness and grid size over the values indicated, for a unit pressure differential. The standard deviation of the error across the beam is plotted for increasing grid size and beam thickness, all other parameters remaining constant. Because the finite element method is an approximation, there will always be a small amount of error, therefore a standard deviation of zero is not expected. It's clear there is a region of optimum performance for this model. The trough formed represents the optimum grid size given a beam's physical size. The error increases as the grid becomes too large because the real boundary layer
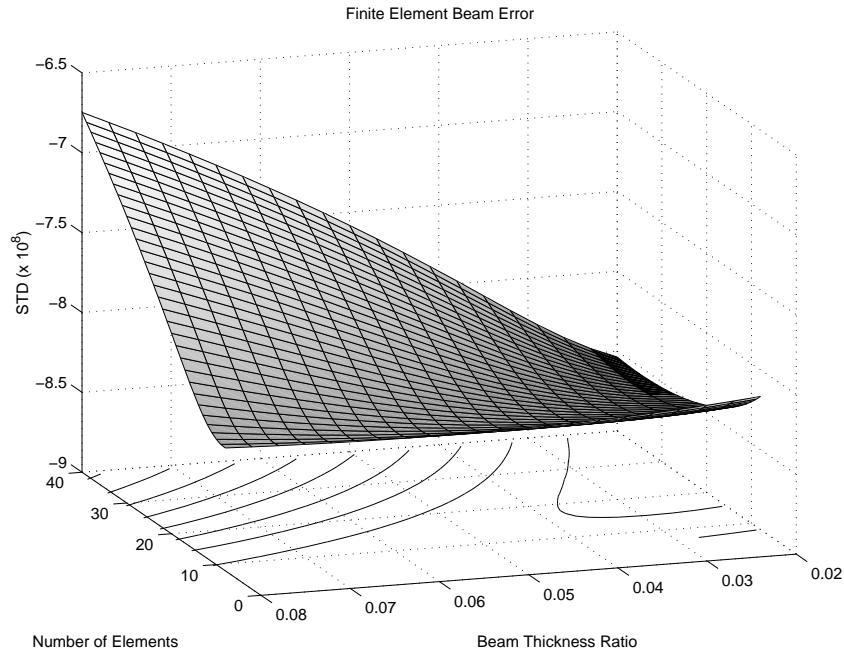
Figure 5.11   Cubic C^1 Element Error (Beam Thickness vs. Grid Size)

effect analytically modelled becomes larger than the shape functions can accurately model. As the thickness increases the beam-string becomes more of a beam. The fundamental assumption of a beam-string is that the thickness-to-length ratio is very small. It's expected the error increases as this value increases.

As mentioned, the minimum of this surface provides the optimum grid size for a given beam thickness. Fitting a curve to the trough results in:

$$n = \frac{1}{2}t^{-\frac{13}{12}} \tag{5.81}$$

where t is the beam thickness and n is the number of grid elements. This trough is clear at these extreme values, but becomes extremely flat as beam thickness shrinks. This indicates good results can be attained with a large range of grid density selections.

5-22

5.3.3 Natural Response.

The dynamic properties of the clamped-clamped linear beam-string can be studied through the sequential evaluation of Equations 5.69 through 5.71. By neglecting forcing, we can calculate the natural modes of this system ($\Gamma_i = 0, i = 0, 1, 2, ...$). As discussed in Section 5.3.2, the solution implementation can be rescaled using:

$$\hat{d} = \hat{d}_0 + \hat{d}_1 + \hat{d}_2 \tag{5.82}$$

where

$$\hat{M}_0 \ddot{\hat{d}}_0 + \hat{K}_0 \hat{d}_0 = 0 \tag{5.83}$$

$$\hat{M}_0 \ddot{\hat{d}}_1 + \hat{K}_1 \hat{d}_1 = -\hat{K}_1 \hat{d}_0 - \left(2\hat{\omega}_1 \hat{M}_0 + \hat{M}_1 \right) \ddot{\hat{d}}_0 \tag{5.84}$$

$$\hat{M}_0 \ddot{\hat{d}}_2 + \hat{K}_2 \hat{d}_2 = -\hat{K}_1 \hat{d}_1 - \hat{K}_2 \hat{d}_0 - \left(2\hat{\omega}_1 \hat{M}_0 + \hat{M}_1 \right) \ddot{\hat{d}}_1$$
$$- \left[\left(2\hat{\omega}_2 + \hat{\omega}_1^2 \right) \hat{M}_0 + 2\hat{\omega}_1 \hat{M}_1 + \hat{M}_2 \right] \ddot{\hat{d}}_0 \tag{5.85}$$

and

$$\begin{aligned}
\hat{M}_0 &= M_0 & \hat{K}_0 &= K_0 & \hat{\omega}_0 &= \omega_0 \\
\hat{M}_1 &= \varepsilon M_1 & \hat{K}_1 &= \varepsilon K_1 & \hat{\omega}_1 &= \varepsilon \omega_1 \\
\hat{M}_2 &= \varepsilon^2 M_2 & \hat{K}_2 &= \varepsilon^2 K_2 & \hat{\omega}_2 &= \varepsilon^2 \omega_2
\end{aligned} \tag{5.86}$$

The response frequencies are now:

$$\hat{\omega} = \hat{\omega}_0 + \hat{\omega}_1 + \hat{\omega}_2 \tag{5.87}$$

The solution to Equation 5.83 is found through a standard eigenanalysis method assuming $\hat{d}_0 = \nu_0 e^{i\hat{\omega}_0 t}$:

$$\left[\hat{K}_0 - \lambda_0 \hat{M}_0 \right] \nu_0 = 0 \tag{5.88}$$

where $\hat{\omega}_0 = \sqrt{\lambda_0}$, the first order frequencies of the system corresponding to the first order mode shapes, ν_0. It should be noted here, due to the shape functions used in

5-23

this analysis which are described in Appendix B, this system is positive semi-definite. The next level will provide corrections to this solution. Continuing this methodology to Equation 5.84:

$$\left[\hat{K}_0 - \lambda_0 \hat{M}_0\right] \nu_1 = -\left[\hat{K}_1 - \lambda_0 \left(2\hat{\omega}_1 \hat{M}_0 + \hat{M}_1\right)\right] \nu_0 \tag{5.89}$$

Since the space spanned by ν_0 completely defines all mode contributions allowed in Equation 5.88. Any contribution to the solution through ν_1 must then be orthogonal to the ν_0 solution. We can impose this by premultiplying Equation 5.89 by the solution of Equation 5.88. The right side, with only one undetermined value, can be solved:

$$\hat{\omega}_1 = \frac{\nu_0^T \left[\hat{K}_1 - \lambda_0 \hat{M}_1\right] \nu_0}{2\lambda_0 \nu_0^T \hat{M}_0 \nu_0} \tag{5.90}$$

providing the first ω correction.

Continuing this procedure to the next level, the next ω correction can be calculated using the same procedure from Equation 5.85:

$$\hat{\omega}_2 = \frac{\nu_0^T \left[\hat{K}_2 - \lambda_0 \left(\hat{\omega}_1^2 \hat{M}_0 + 2\hat{\omega}_1 \hat{M}_1 + \hat{M}_2\right)\right] \nu_0}{2\lambda_0 \nu_0^T \hat{M}_0 \nu_0} \tag{5.91}$$

Section 5.3.2 clearly illustrated the advantage of choosing Cubic C^1 shape functions over Linear C^1 shape functions developed in Appendix B. Applying these shape functions to the above procedure will provide a basis for the same decision when used in dynamic analysis.

5.3.3.1 *Linear C^1 Shape Function Results.* Figure 5.12 plots the first several computed wave shapes predicted by this system. As expected they are very near a string solution. The coarse grid size accentuates the poor quality of the Linear C^1 elements. As the grid density is increased; however, the mode shapes become very smooth, as expected. Correspondingly, the scaled mode frequencies are

5-24
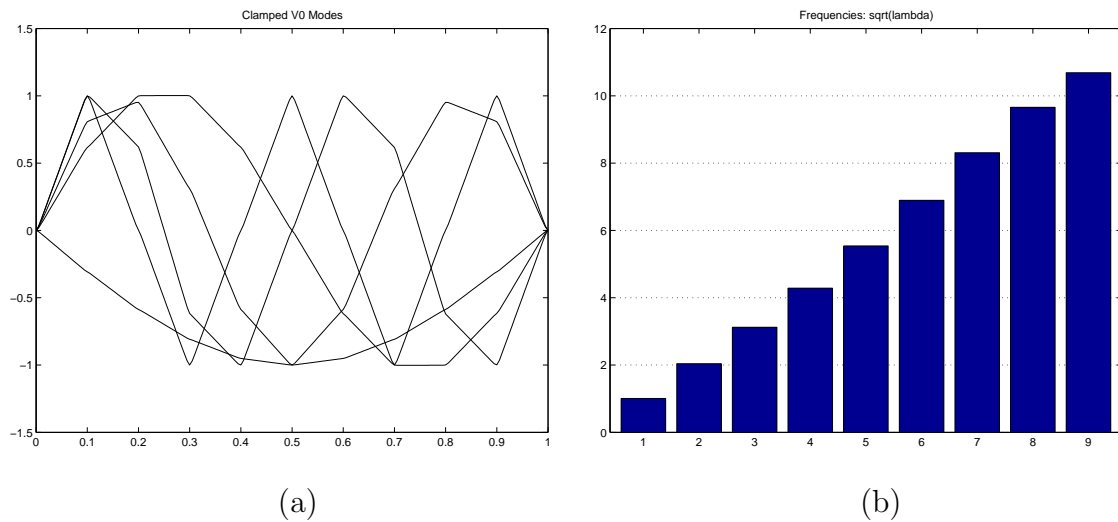
Figure 5.12   Linear C^1 Modes: (a) First 5 Mode Shapes (b) Normalized Frequencies

presented in Figure 5.12. The increased stiffness of the system is again apparent as the modal frequencies are higher than expected, especially at the higher modes.

5.3.3.2 Cubic C^1 Shape Function Results.   Figure 5.13 plots the first five computed wave shapes predicted by this system. While both solutions approach the analytical beam-string solution, the superiority of the Cubic C^1 elements is clear. The grid size and properties are identical to that used in Section 5.3.2. Correspondingly, the scaled mode frequencies are presented in Figure 5.13. As the beam's thickness-to-length ratio decreases, the scaled modal frequencies continue to approach integer values representing string solutions. Due to the apparent superiority of the Cubic C^1 element, the Linear C^1 element will no longer be used in this analysis. So far only undamped systems have been considered. To properly study system dynamics, damped response should be included.

5.3.4   Damped Response.   Forced response computation of a dynamic system often requires the addition of damping terms. Damping terms are nonconservative contributions and can't be directly inserted into the system Lagrangian. This effect is normally inserted directly into the equations of motion,
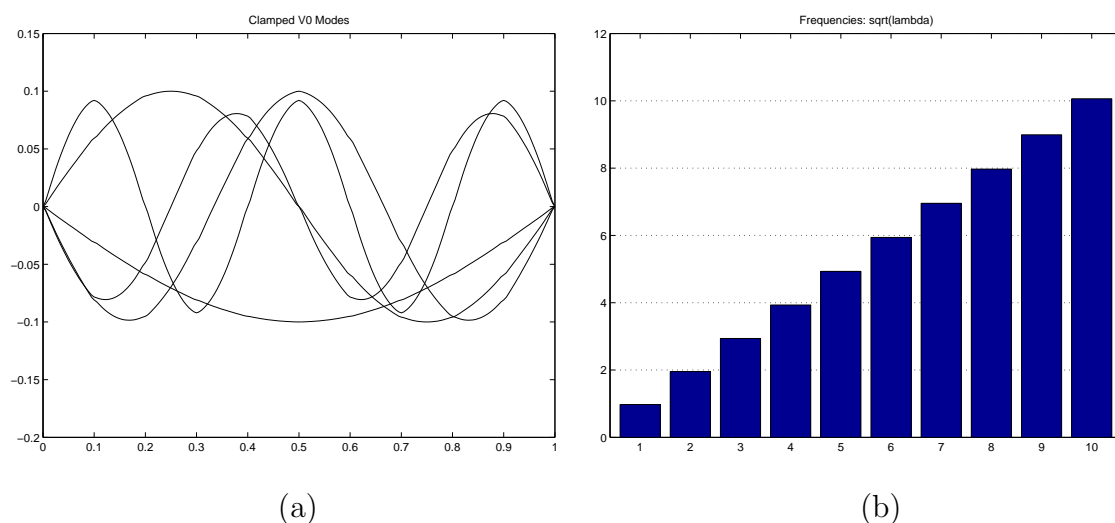
Figure 5.13   Cubic C^1 Modes: (a) First 5 Mode Shapes (b) Normalized Frequencies

and values are assigned through experimental evaluation. The Method of Integral Multiple Scales (MIMS) will require a similar approach.

Analytic solutions discussed in Chapters III and IV indicate the damping terms commonly fall one level lower in the asymptotic expansion. Finite element methods commonly model the damping term using the known mass and stiffness matrices. *Rayleigh* or *proportional* damping is one example (65):

$$[C] = \alpha [K] + \beta [M] \tag{5.92}$$

where α and β are related to critical damping ξ and frequency ω through

$$\xi = \frac{1}{2} \left(\alpha \omega + \frac{\beta}{\omega} \right). \tag{5.93}$$

The parameters α and β are considered of order ε for the materials discussed herein.

To understand how the damping terms are related to the system presented in Equations 5.69 through 5.71, remove any temporal related scaling terms (dropping

5-26

www.manaraa.com

[ ] brackets again):

$$M_0\ddot{d}_0 + K_0 d_0 \;=\; -\Gamma_0 \tag{5.94}$$

$$M_0\ddot{d}_1 + K_0 d_1 \;=\; -\Gamma_1 - M_1\ddot{d}_0 - K_1 d_0 \tag{5.95}$$

$$M_0\ddot{d}_2 + K_0 d_2 \;=\; -\Gamma_2 - M_1\ddot{d}_1 - K_1 d_1$$
$$- M_2\ddot{d}_0 - K_2 d_0. \tag{5.96}$$
$$\vdots$$

Multiplying each level by its corresponding ε order, and summing the system, the following results:

$$M_0 \sum_{i=0}^{n} \varepsilon^i \ddot{d}_i + K_0 \sum_{i=0}^{n} \varepsilon^i d_i = -\sum_{i=0}^{n} \varepsilon^i \Gamma_i - \varepsilon M_1 \sum_{i=0}^{n-1} \varepsilon^i \ddot{d}_i - \varepsilon K_1 \sum_{i=0}^{n-1} \varepsilon^i d_i$$
$$- \varepsilon^2 M_2 \sum_{i=0}^{n-2} \varepsilon^i \ddot{d}_i - \varepsilon^2 K_2 \sum_{i=0}^{n-2} \varepsilon^i d_i - \cdots \tag{5.97}$$

As $n \to \infty$, the system can be reorganized as

$$M\ddot{d} + Kd = -\Gamma \tag{5.98}$$

where

$$M = M_0 + \varepsilon M_1 + \varepsilon^2 M_2 + \cdots$$
$$K = K_0 + \varepsilon K_1 + \varepsilon^2 K_2 + \cdots$$
$$\Gamma = \Gamma_0 + \varepsilon \Gamma_1 + \varepsilon^2 \Gamma_2 + \cdots \tag{5.99}$$
$$d = d_0 + \varepsilon d_1 + \varepsilon^2 d_2 + \cdots .$$

Combining this result with Equation 5.92, a damping matrix expansion is suggested

$$C = \varepsilon C_1 + \varepsilon^2 C_2 + \cdots \tag{5.100}$$

where

$$C_i = \alpha_1 K_{i-1} + \beta_1 M_{i-1}. \tag{5.101}$$

This term can then be inserted into Equations 5.83 through 5.85, producing:

$$M_0 \ddot{d}_0 + K_0 d_0 = -\Gamma_0 \tag{5.102}$$

$$M_0 \ddot{d}_1 + K_0 d_1 = -\Gamma_1 - [2\omega_1 M_0 + M_1] \ddot{d}_0 - C_1 \dot{d}_0 - K_1 d_0 \tag{5.103}$$

$$\begin{aligned} M_0 \ddot{d}_2 + K_0 d_2 = {} & -\Gamma_2 - [2\omega_1 M_0 + M_1] \ddot{d}_1 - C_1 \dot{d}_1 - K_1 d_1 \\ & - \left[\left(2\omega_2 + \omega_1^2 \right) M_0 + 2\omega_1 M_1 + M_2 \right] \ddot{d}_0 \\ & - C_2 \dot{d}_0 - K_2 d_0 \end{aligned} \tag{5.104}$$

The solution to Equation 5.102 is found through a standard eigenanalysis method assuming $d_0 = \nu_0 e^{i\omega_0 t}$:

$$[K_0 - \lambda_0 M_0] \nu_0 = 0 \tag{5.105}$$

where $\omega_0 = \sqrt{\lambda_0}$, the first order frequencies of the system corresponding to the first order mode shapes, ν_0. Continuing this methodology to Equation 5.103

$$[K_0 - \lambda_0 M_0] \nu_1 = -[K_1 + i\omega_0 C_1 - \lambda_0 (2\omega_1 M_0 + M_1)] \nu_0 \tag{5.106}$$

As discussed earlier, the space spanned by ν_0 completely defines all mode contributions allowed in Equation 5.105. Any contribution to the solution through ν_1 must then be orthogonal to the ν_0 solution. We can impose this by premultiplying Equation 5.106 by the solution of Equation 5.105. The right side, with only one undetermined value, can be solved:

$$\omega_1 = \frac{\nu_0^T [K_1 + i\omega_0 C_1 - \lambda_0 M_1] \nu_0}{2\lambda_0 \nu_0^T M_0 \nu_0} \tag{5.107}$$

5-28

providing the first ω correction.

Continuing this procedure to the next level, the next ω correction can be calculated using the same procedure from Equation 5.104:

$$\omega_2 = \frac{\nu_0^T \left[K_2 + i\left(\omega_0 C_2 + \omega_1 C_1\right) - \lambda_0 \left(\omega_1^2 M_0 + 2\omega_1 M_1 + M_2\right)\right] \nu_0}{2\lambda_0 \nu_0^T M_0 \nu_0} \tag{5.108}$$

The damped response frequencies can then be computed through Equation 5.16. Further expansion of this method, to include forced response is introduced in the next chapter.

This chapter introduced the Method of Integral Multiple Scales as a new method for solving some dynamic systems which can be represented in Lagrangian form. After presenting a short analytical beam-string example, this method was applied through a new finite element approach. By using a new set of parametric shape functions based on beam-strings developed in Appendix B, the power of this method was revealed. Both shape function sets can be regarded as C^1 class because they represent both displacements and displacement rates, while allowing extremely small bending stiffness. A 'Linear' set, incapable of modeling internal curvature, was compared to a 'Cubic' set, which does allow for internal curvature. Applying these shape functions to the beam-string example in both static and dynamic analysis indicated the supremacy of the 'Cubic' set. Based on the results of this chapter, this method can be used to analyze more complicated non-linear systems of interest.

VI. Nonlinear Finite Element Solutions

The Method of Integral Multiple Scales (MIMS) was introduced in Chapter V as a method to model dynamic systems which can be represented in Lagrangian form. The linear beam example clearly shows the ability of this method to produce adequate solutions. While the simple beam did provide interesting insight into the method itself, the real power of the method can be better presented through nonlinear applications, such as those systems analytically solved in Chapters III and IV. In this chapter, these analytical solutions are expanded.

6.1 Nonlinear Beam-String

The nonlinear piezoelectric beam analytically solved in Chapter III can be analyzed using a finite element approach based on the Method of Integral Multiple Scales (MIMS) introduced in Chapter V. Equations 3.1 through 3.7, neglecting the spring boundary conditions, are used here to derive the system Lagrangian.

6.1.1 System Derivation.

In Chapter III, the equations of motion were derived prior to scaling. To apply MIMS, the Lagrangian must be scaled. Referring to Figure 3.1, ds and dx are the deformed and undeformed beam infinitesimal lengths, respectively, and related through the following vector equation:

$$d\vec{s} = \langle 1 + u_{,x}, w_{,x} \rangle dx \tag{6.1}$$

and, after expansion, results in the following scalar equation:

$$ds = \left(1 + u_{,x} + \frac{1}{2} w_{,x}^2 + u_{,x}^2 + \frac{1}{8} w_{,x}^4 + \frac{1}{2} u_{,x} w_{,x}^2 \ldots \right) dx \tag{6.2}$$

6-1

Applying this to the energy formulation, the Lagrangian can then be formed

$$
\begin{aligned}
\mathbb{L} = \int_{\mathcal{V}} \Bigg[&\frac{1}{2}\rho \left(u_{,t}^2 + w_{,t}^2 \right) - \\
&\frac{1}{2}E \left(u_{,x} + \frac{1}{2}w_{,x}^2 + \frac{1}{2}u_{,x}w_{,x}^2 - \frac{1}{8}w_{,x}^4 \right)^2 + \\
&Ezw_{,xx} \left(u_{,x} + \frac{1}{2}w_{,x}^2 + \frac{1}{2}u_{,x}w_{,x}^2 - \frac{1}{8}w_{,x}^4 \right) - \\
&Ez^2w_{,xx}^2 - E\epsilon_0 \left(u_{,x} + \frac{1}{2}w_{,x}^2 + \frac{1}{2}u_{,x}w_{,x}^2 - \frac{1}{8}w_{,x}^4 \right) + \\
&E\epsilon_0 zw_{,xx} + \frac{N_0}{A} \left(u_{,x} + \frac{1}{2}w_{,x}^2 + \frac{1}{2}u_{,x}w_{,x}^2 - \frac{1}{8}w_{,x}^4 \right) - \\
&\frac{N_0}{A}zw_{,xx} \Bigg] d\mathcal{V} + \int_x P \left(w + u_{,x}w - w_{,x}u \right) dx
\end{aligned}
\tag{6.3}
$$

where

$$
\epsilon_0 = \frac{d_{31}V}{t} + \alpha T.
\tag{6.4}
$$

Equations 3.6 are again used to reduce this three-dimensional system to a single dimension. The resulting Lagrangian is

$$
\begin{aligned}
\mathbb{L} = \int_x \Bigg[&\frac{1}{2}\rho A \left(u_{,t}^2 + w_{,t}^2 \right) - \\
&\frac{1}{2}EA \left(u_{,x} + \frac{1}{2}w_{,x}^2 + \frac{1}{2}u_{,x}w_{,x}^2 - \frac{1}{8}w_{,x}^4 \right)^2 + \\
&EZw_{,xx} \left(u_{,x} + \frac{1}{2}w_{,x}^2 + \frac{1}{2}u_{,x}w_{,x}^2 - \frac{1}{8}w_{,x}^4 \right) - \\
&EIw_{,xx}^2 - EA_\epsilon \left(u_{,x} + \frac{1}{2}w_{,x}^2 + \frac{1}{2}u_{,x}w_{,x}^2 - \frac{1}{8}w_{,x}^4 \right) + \\
&EZ_\epsilon w_{,xx} + N_0 \left(u_{,x} + \frac{1}{2}w_{,x}^2 + \frac{1}{2}u_{,x}w_{,x}^2 - \frac{1}{8}w_{,x}^4 \right) - \\
&N_z w_{,xx} + P \left(w + u_{,x}w - w_{,x}u \right) \Bigg] dx.
\end{aligned}
\tag{6.5}
$$

6-2

Equations 3.15 can now be applied and the scaled non-linear laminated piezothermoelectric beam's Lagrangian is

$$
\begin{aligned}
\mathbb{L} = \int_0^1 \Bigg[& \frac{1}{2}\left(u_{,t}^2 + w_{,t}^2\right) - \\
& \frac{1}{2}\eta_{-1}\left(u_{,x} + \frac{1}{2}w_{,x}^2 + \frac{1}{2}u_{,x}w_{,x}^2 - \frac{1}{8}w_{,x}^4\right)^2 + \\
& EZ_2 w_{,xx}\left(u_{,x} + \frac{1}{2}w_{,x}^2 + \frac{1}{2}u_{,x}w_{,x}^2 - \frac{1}{8}w_{,x}^4\right) - \\
& \varepsilon^2 w_{,xx}^2 - (1 - EA_{\epsilon 2})\left(u_{,x} + \frac{1}{2}w_{,x}^2 + \frac{1}{2}u_{,x}w_{,x}^2 - \frac{1}{8}w_{,x}^4\right) + \\
& EZ_{\epsilon 3} w_{,xx} - N_z w_{,xx} + P_2\left(w + u_{,x}w - w_{,x}u\right) \Bigg] dx.
\end{aligned}
\tag{6.6}
$$

where the subscript numbering indicates the specific parameter's relative order based on the order os ε. With the correctly scaled Lagrangian available, MIMS can be applied.

As previously used in Chapter V, the boundary layer areas are introduced through the stretching variables (or spatial scales):

$$
\begin{aligned}
u(x,t) &\to u(\eta, \xi, \zeta, t; \varepsilon) \\
w(x,t) &\to w(\eta, \xi, \zeta, t; \varepsilon)
\end{aligned}
\tag{6.7}
$$

where $\eta = x$, $\xi = \frac{x}{\varepsilon}$, and $\zeta = \frac{1-x}{\varepsilon}$. Applying the chain rule to $x = x(\eta, \xi, \zeta; \varepsilon)$, the differentials are transformed

$$
\frac{d}{dx} = \frac{\partial}{\partial \eta} + \frac{1}{\varepsilon}\left[\frac{\partial}{\partial \xi} - \frac{\partial}{\partial \zeta}\right]
\tag{6.8}
$$

$$
\frac{d^2}{dx^2} = \frac{\partial^2}{\partial \eta^2} + \frac{2}{\varepsilon}\left[\frac{\partial^2}{\partial \xi \partial \eta} - \frac{\partial^2}{\partial \zeta \partial \eta}\right] + \frac{1}{\varepsilon^2}\left[\frac{\partial^2}{\partial \xi^2} + \frac{\partial^2}{\partial \zeta^2} - 2\frac{\partial^2}{\partial \xi \partial \zeta}\right].
\tag{6.9}
$$

Substituting the expansions (also introducing temporal scaling)

$$t = \omega\tau \tag{6.10}$$

$$T_n = \varepsilon^n\tau \tag{6.11}$$

$$\omega = \omega_0 + \varepsilon\omega_1 + \varepsilon^2\omega_2 + \cdots \tag{6.12}$$

$$N(\eta,\xi,\zeta;\varepsilon) = N_0(\eta,\xi,\zeta) + \varepsilon N_1(\eta,\xi,\zeta) + \varepsilon^2 N_2(\eta,\xi,\zeta) + \cdots \tag{6.13}$$

$$N_u(\eta,\xi,\zeta;\varepsilon) = N_{u0}(\eta,\xi,\zeta) + \varepsilon N_{u1}(\eta,\xi,\zeta) + \varepsilon^2 N_{u2}(\eta,\xi,\zeta) + \cdots \tag{6.14}$$

$$d(t;\varepsilon) = \varepsilon^2 d_2(t) + \varepsilon^3 d_3(t) + \varepsilon^4 d_4(t) + \cdots \tag{6.15}$$

$$d_u(t;\varepsilon) = \varepsilon^3 d_{u3}(t) + \varepsilon^4 d_{u4}(t) + \varepsilon^5 d_{u5}(t) + \cdots \tag{6.16}$$

$$u(\eta,\xi,\zeta,t;\varepsilon) = N_u(\eta,\xi,\zeta;\varepsilon)d_u(t;\varepsilon) \tag{6.17}$$

$$w(\eta,\xi,\zeta,t;\varepsilon) = N(\eta,\xi,\zeta;\varepsilon)d(t;\varepsilon) \tag{6.18}$$

where $\omega_0 = 1$ as the original system was effectively scaled by ω_0, into Equation 6.6 produces a multiple scales Lagrangian expansion. Separating the resulting expansion into ε-order groupings, produces a Laurent series of Lagrangians of increasing order:

$$\mathbb{L} = \varepsilon^{-2}\mathbb{L}_{-2} + \varepsilon^{-1}\mathbb{L}_{-1} + \mathbb{L}_0 + \varepsilon\mathbb{L}_1 + \varepsilon^2\mathbb{L}_2 + \cdots \tag{6.19}$$

Once again, selecting the order of precision is equivalent to selecting an element ($\mathbb{L}_i$) in the energy expansion. Applying Euler's equations to the selected Lagrangian element produces the system of equations which will produce the desired solution. The functions produced through the application of Euler's equations to $\mathbb{L}_n$ exists in the set of functions produced through the application of Euler's equations to $\mathbb{L}_m$, where $m > n$.

Applying Euler's equations to $\mathbb{L}_2$ produces the following decoupled system of equations:

$$K_{-2}d_2 = 0 \tag{6.20}$$

$$K_{-2}d_3 = -K_{-1}d_2 \tag{6.21}$$

$$K_{-2}d_4 = -K_{-1}d_3 - \Gamma_0 - M_0 d_{3,00} - K_0 d_0 \tag{6.22}$$

$$\begin{aligned} K_{-2}d_5 = {} & -K_{-1}d_4 - \Gamma_1 - M_0 d_{4,00} - K_0 d_3 \\ & -2M_0\left(\omega_1 d_{0,00} + d_{0,01}\right) - M_1 d_{0,00} - K_1 d_0 \end{aligned} \tag{6.23}$$

$$\begin{aligned} K_{-2}d_6 = {} & -K_{-1}d_5 - \Gamma_2 - M_0 d_{5,00} - K_0 d_3 \\ & -2M_0\left(\omega_1 d_{3,00} + d_{3,01}\right) - M_1 d_{3,00} - K_1 d_3 \\ & -M_0\left[d_{2,11} + d_{2,02} + 4\omega_1 d_{2,01} + \left(\omega_1^2 + 2\omega_2\right) d_{2,00}\right] \\ & -2M_1\left(\omega_1 d_{2,00} + d_{2,01}\right) - M_2 d_{2,00} - K_2 d_2 \end{aligned} \tag{6.24}$$

$$M_{u0} d_{u3,00} = 0 \tag{6.25}$$

where K_i represents system stiffness matrices, M_i and M_{u0} represents system mass matrices, and Γ_i represents system forcing. Additional equations of import are:

$$\begin{aligned} N_{u3,\xi} &= N_{u3,\zeta} \\ N_{u4,\xi} &= N_{u4,\zeta} \\ N_{u5,\xi} &= N_{u5,\zeta} \\ N_{u6,\xi} &= N_{u6,\zeta} \end{aligned} \tag{6.26}$$

Equations 6.20 and 6.21 are the first two solvability equations. As discussed in Chapter V, these drive the choice of shape functions necessary. Equations 6.26 presents an additional set of solvability conditions in this analysis. These indicate no axial boundary layer effects exist, to this level, based on the assumptions and scaling choices made earlier in this analysis. Additionally, the axial displacements are not

present in the transverse displacement equations at the level of expansion presented. Therefore, the axial displacements will not be considered in the remaining portion of this beam analysis. This parallels the results found in Chapter III.

The various system matrices can be calculated by applying either of the shape functions presented in Appendix B. The resulting matrices are:

$$
\begin{aligned}
K_{-2} &= 0 \\
K_{-1} &= 0 \\
K_0 &= \int_x F_1^T F_1 + G_1^T G_1 dx \\
K_1 &= \int_x F_1^T F_2 + F_2^T F_1 + G_1^T G_2 + G_2^T G_1 dx \\
K_2 &= \int_x F_2^T F_2 + F_1^T F_3 + F_3^T F_1 + G_2^T G_2 + G_1^T G_3 + G_3^T G_1 + EA_{\epsilon 2} G_1^T G_1 dx
\end{aligned}
\tag{6.27}
$$

$$
\begin{aligned}
M_0 &= \int_x N_0^T N_0 dx \\
M_1 &= \int_x N_0^T N_1 + N_1^T N_0 dx \\
M_2 &= \int_x N_1^T N_1 + N_0^T N_2 + N_2^T N_0 dx
\end{aligned}
\tag{6.28}
$$

The forcing vectors are similarly produced:

$$
\begin{aligned}
\Gamma_0 &= \int_x -P N_0^T dx \\
\Gamma_1 &= \int_x \left(N_{z3} - EZ_{\epsilon 3} \right) F_1^T - P N_1^T dx \\
\Gamma_2 &= \int_x \left(N_{z3} - EZ_{\epsilon 3} \right) F_2^T - P N_2^T dx
\end{aligned}
\tag{6.29}
$$

As discussed in Chapter III, the actuation manifests itself through an axial strain term $(EA_{\epsilon 2})$ and a boundary moment term $(EZ_{\epsilon 3})$. The axial term modifies the system stiffness and the boundary term acts as an applied forcing term. Removal

of the piezothermal terms produces the same equations as the linear system produced in Chapter V.

The multiple scales integral can be transformed to the scaled variables as

$$\int_{x_1}^{x_2} f(x)dx = \int_0^{\frac{x_2-x_1}{\epsilon}} \int_0^{\frac{x_2-x_1}{\epsilon}} \int_{x_1}^{x_2} f(\eta, \xi, \zeta)d\eta \epsilon d\xi \epsilon d\zeta. \tag{6.30}$$

The undamped dynamic system of equations is then:

$$M_0 d_{2,00} + K_0 d_2 = -\Gamma_0 \tag{6.31}$$

$$M_0 d_{3,00} + K_0 d_3 = -\Gamma_1 - (2\omega_1 M_0 + M_1) d_{2,00} - 2M_0 d_{2,01} - K_1 d_2 \tag{6.32}$$

$$\begin{aligned} M_0 d_{4,00} + K_0 d_4 = {} & -\Gamma_2 - (2\omega_1 M_0 + M_1) d_{3,00} - 2M_0 d_{3,01} - K_1 d_3 \\ & - \left[\left(\omega_1^2 + 2\omega_2 \right) M_0 + 2\omega_1 M_1 + M_2 \right] d_{2,00} \\ & -2 \left(2\omega_1 M_0 + M_1 \right) d_{2,01} - M_0 d_{2,11} - 2M_0 d_{2,02} - K_2 d_2 \end{aligned} \tag{6.33}$$

which represents the finite element equations of motion of the non-linear piezoelectric beam string. Including damping terms, discussed in Chapter V, results in the damped dynamic system of equations for a non-linear piezoelectric beam string:

$$M_0 d_{2,00} + K_0 d_2 = -\Gamma_0 \tag{6.34}$$

$$\begin{aligned} M_0 d_{3,00} + K_0 d_3 = {} & -\Gamma_1 - (2\omega_1 M_0 + M_1) d_{2,00} - 2M_0 d_{2,01} \\ & -K_1 d_2 - C_1 d_{2,0} \end{aligned} \tag{6.35}$$

$$\begin{aligned} M_0 d_{4,00} + K_0 d_4 = {} & -\Gamma_2 - (2\omega_1 M_0 + M_1) d_{3,00} - 2M_0 d_{3,01} \\ & - \left[\left(\omega_1^2 + 2\omega_2 \right) M_0 + 2\omega_1 M_1 + M_2 \right] d_{2,00} \\ & -K_1 d_3 - C_1 d_{3,0} - C_2 d_{2,0} - C_1 d_{2,1} \\ & -2 \left(2\omega_1 M_0 + M_1 \right) d_{2,01} - M_0 d_{2,11} - 2M_0 d_{2,02} - K_2 d_2 \end{aligned} \tag{6.36}$$

Additional effects can be introduced with increasing Lagrangian order selection. This system can now be used to analyze problem solutions unattainable through analytical methods.

Equation 6.15 is a function of ε, but this value is based on the global dimensions of the beam. To more directly produce a finite element solution, as presented in Chapter V, this value can be integrated into the system matrices. Beginning with Equation 6.15, the equivalent displacement equation is:

$$\hat{d} = \hat{d}_2 + \hat{d}_3 + \hat{d}_4 \tag{6.37}$$

where

$$\begin{aligned}
\hat{d}_2 &= \varepsilon^2 d_2 \\
\hat{d}_3 &= \varepsilon^3 d_3 \\
\hat{d}_4 &= \varepsilon^4 d_4,
\end{aligned} \tag{6.38}$$

Equations 6.31 through 6.33 can be rescaled:

$$\hat{M}_0 \hat{d}_{2,00} + \hat{K}_0 \hat{d}_2 \;=\; -\hat{\Gamma}_0 \tag{6.39}$$

$$\begin{aligned}
\hat{M}_0 \hat{d}_{3,00} + \hat{K}_0 \hat{d}_3 \;=\; &-\hat{\Gamma}_1 - \left(2\hat{\omega}_1 \hat{M}_0 + \hat{M}_1\right) \hat{d}_{2,00} - 2\hat{M}_0 \hat{d}_{2,01} \\
&-\hat{C}_1 \hat{d}_{2,0} - \hat{K}_1 \hat{d}_2
\end{aligned} \tag{6.40}$$

$$\begin{aligned}
\hat{M}_0 \hat{d}_{4,00} + \hat{K}_0 \hat{d}_4 \;=\; &-\hat{\Gamma}_2 - \left(2\hat{\omega}_1 \hat{M}_0 + \hat{M}_1\right) \hat{d}_{3,00} - 2\hat{M}_0 \hat{d}_{3,01} \\
&-\hat{C}_1 \hat{d}_{3,0} - \hat{K}_1 \hat{d}_3 \\
&- \left[\left(\hat{\omega}_1^2 + 2\hat{\omega}_2\right) \hat{M}_0 + 2\hat{\omega}_1 \hat{M}_1 + \hat{M}_2\right] \hat{d}_{2,00} \\
&-2\left(2\hat{\omega}_1 \hat{M}_0 + \hat{M}_1\right) \hat{d}_{2,01} - \hat{M}_0 \hat{d}_{2,11} - 2\hat{M}_0 \hat{d}_{2,02} \\
&-\hat{C}_2 \hat{d}_{2,0} - \hat{C}_1 \hat{d}_{2,1} - \hat{K}_2 \hat{d}_2
\end{aligned} \tag{6.41}$$
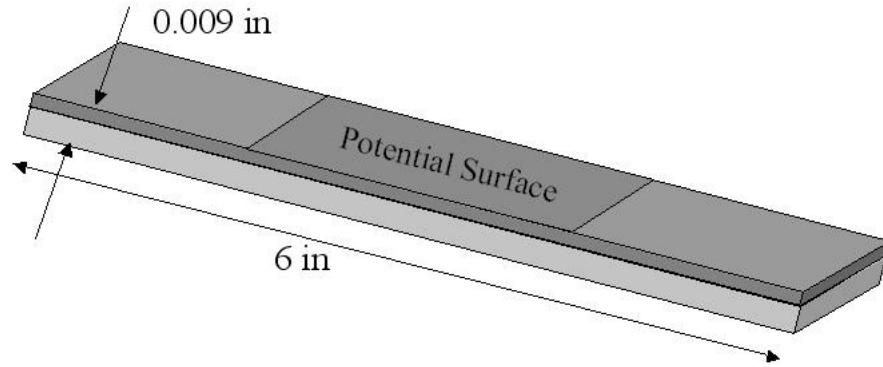
Figure 6.1   Piezoelastic Laminated Beam Configuration

Property	Kapton	PVDF
Young's Modulus (E)	406 ksi	261 ksi
Thickness Ratio (t)	0.006 in	0.003 in

Table 6.1   Linear Beam Element Properties

and

$$
\begin{aligned}
&\hat{M}_0 = M_0 && \hat{K}_0 = K_0 && && \hat{\Gamma}_0 = \varepsilon^2 \Gamma_0 && \hat{\omega}_0 = \omega_0 \\
&\hat{M}_1 = \varepsilon M_1 && \hat{K}_1 = \varepsilon K_1 && \hat{C}_1 = \varepsilon C_1 && \hat{\Gamma}_1 = \varepsilon^3 \Gamma_1 && \hat{\omega}_1 = \varepsilon \omega_1 \\
&\hat{M}_2 = \varepsilon^2 M_2 && \hat{K}_2 = \varepsilon^2 K_2 && \hat{C}_2 = \varepsilon^2 C_2 && \hat{\Gamma}_2 = \varepsilon^4 \Gamma_2 && \hat{\omega}_2 = \varepsilon^2 \omega_2
\end{aligned}
\tag{6.42}
$$

The response frequencies are now:

$$
\hat{\omega} = \hat{\omega}_0 + \hat{\omega}_1 + \hat{\omega}_2 \tag{6.43}
$$

The solution methodology is identical to that presented in Chapter V. Each level is solved in succession to produce an increasingly more accurate prediction.

6.1.2   Static Shaping.   A piezoelastic laminated beam shown in Figure 6.1 was modelled with the properties listed in Table 6.1. Using an etched electrode covering the center third of the beam, the shape presented in Figure 6.2 results from only electrical potential application ($d_{31}V = 10^{-7}$). Each plot is the

المنارة للاستشارات

www.manaraa.com
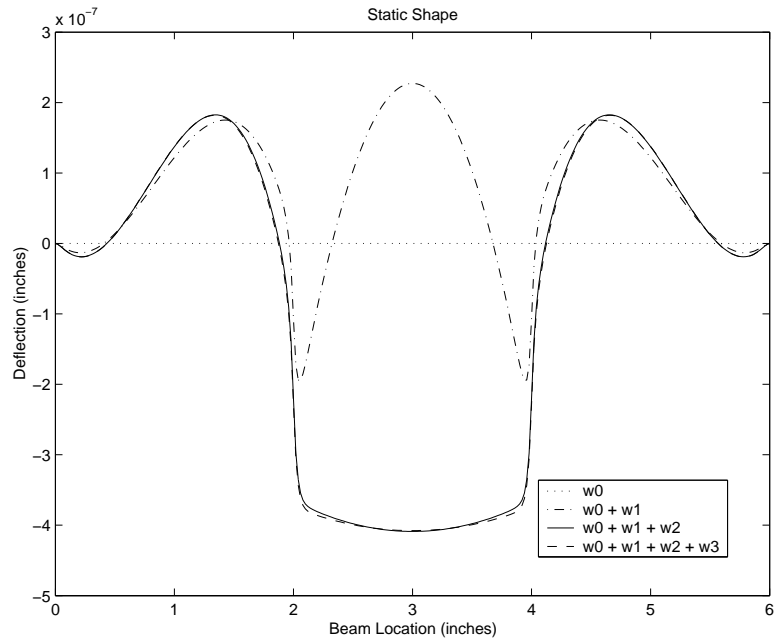
Figure 6.2   Piezoelastic Laminated Beam Corrections
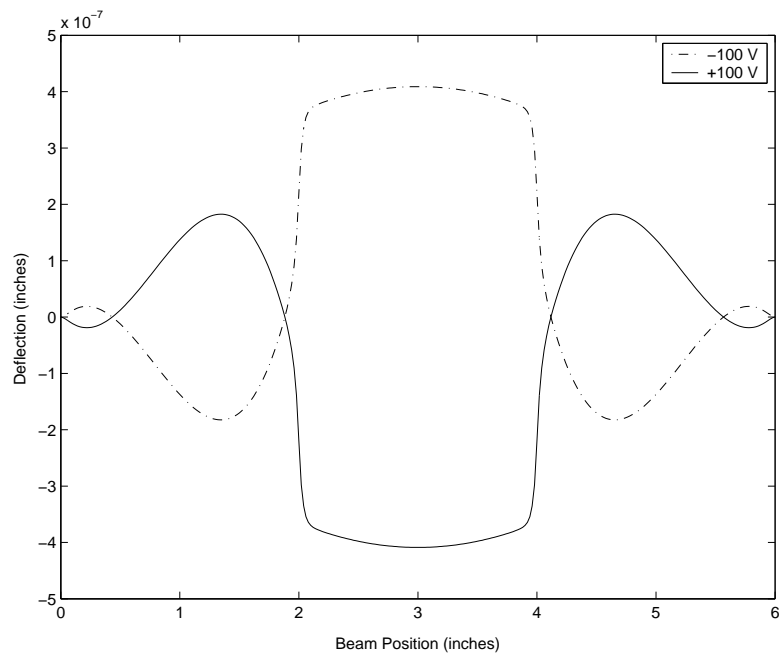
Figure 6.3   Piezoelastic Laminated Beam (+/-) Deflections

6-10

result of successive solution orders. There is no deflection from the first order solution due to the lack of any forcing term at that level. Notice the significant change in shape through the two subsequent orders. The second order solution provides initial peizoelectric moments, while the third order solution corrects the result through the additional axial forcing terms. The addition of the fourth order correction clearly shows a modest improvement to the predicted shape. Due to the significant increase in computational effort necessary to provide the small correction, further analysis can assume an adequate approximation considering only the first two correction terms. Figure 6.3 illustrates the expected symmetric behavior resulting from opposite actuation voltages.

The electrical interface regions are of particular interest. Modeling these regions of step changes with standard finite elements requires significantly increased grid densities. These standard modeling techniques are required to avoid the singularities existing in this region. The method presented here overcomes this problem and produces results more closely aligned with experimental observations (17).

6.2   *Axisymmetric Plate-Membrane*

The nonlinear axisymmetric piezoelectric plate analytically solved in Chapter IV can also be analyzed using a finite element approach based on the Method of Integral Multiple Scales (MIMS) introduced in Chapter V.

6.2.1   System Derivation.   Equations 4.1 through 4.8, neglecting the spring boundary condition, are used here to derive the system Lagrangian. In Chapter IV, the equations of motion were derived prior to scaling. To apply MIMS,

the Lagrangian must be scaled.

$$
\begin{aligned}
\mathbb{L} = \int_{\mathcal{V}} \Bigg[&\frac{1}{2}\rho\left(u_{,t}^2 + v_{,t}^2 + w_{,t}^2\right) - \\
&\frac{E}{1-\nu^2}\epsilon_{0\theta}\left[\left(u_{,r} + \frac{1}{2}w_{,r}^2\right) + \nu\frac{1}{r}u\right] + \frac{Ez}{1-\nu^2}\epsilon_{0\theta}\left[w_{,rr} + \nu\frac{1}{r}w_{,r}\right] - \\
&\frac{E}{1-\nu^2}\epsilon_{0r}\left[\frac{1}{r}u + \nu\left(u_{,r} + \frac{1}{2}w_{,r}^2\right)\right] + \frac{Ez}{1-\nu^2}\epsilon_{0r}\left[\frac{1}{r}w_{,r} + \nu w_{,rr}\right] + \\
&\frac{2E}{1+\nu}\epsilon_{0z}\left[\frac{1}{r}v - v_{,r}\right] - \frac{E}{1+\nu}\left[\frac{1}{r}v - v_{,r}\right]^2 - \\
&\frac{1}{2}\frac{E}{1-\nu^2}\left(\left[u_{,r} + \frac{1}{2}w_{,r}^2\right]\left[\left(u_{,r} + \frac{1}{2}w_{,r}^2\right) + \nu\frac{1}{r}u\right]\right) - \\
&\frac{1}{2}\frac{E}{1-\nu^2}\left(\frac{1}{r}u\left[\frac{1}{r}u + \nu\left(u_{,r} + \frac{1}{2}w_{,r}^2\right)\right]\right) + \\
&\frac{1}{2}\frac{Ez}{1-\nu^2}\left(w_{,rr}\left[\left(u_{,r} + \frac{1}{2}w_{,r}^2\right) + \nu\frac{1}{r}u\right]\right) + \\
&\frac{1}{2}\frac{Ez}{1-\nu^2}\left(\left[u_{,r} + \frac{1}{2}w_{,r}^2\right]\left[w_{,rr} + \nu\frac{1}{r}w_{,r}\right]\right) + \\
&\frac{1}{2}\frac{Ez}{1-\nu^2}\left(\frac{1}{r}w_{,r}\left[\frac{1}{r}u + \nu\left(u_{,r} + \frac{1}{2}w_{,r}^2\right)\right] + \frac{1}{r}u\left[\frac{1}{r}w_{,r} + \nu w_{,rr}\right]\right) - \\
&\frac{1}{2}\frac{Ez^2}{1-\nu^2}\left(w_{,rr}\left[w_{,rr} + \nu\frac{1}{r}w_{,r}\right] + \frac{1}{r}w_{,r}\left[\frac{1}{r}w_{,r} + \nu w_{,rr}\right]\right) + \\
&\frac{N_{0r}}{H}\left[u_{,r} + \frac{1}{2}w_{,r}^2\right] - \frac{N_{rz}}{H}w_{,rr} + \frac{N_{0\theta}}{H}\frac{1}{r}u - \frac{N_{\theta z}}{H}\frac{1}{r}w_{,r}\Bigg]d\mathcal{V} + \\
&\int_{r} P\left(w + u_{,r}w - w_{,r}u\right)dr
\end{aligned}
\tag{6.44}
$$

where

$$
\epsilon_{0r} = \epsilon_{0\theta} = \frac{d_{31}V}{t} + \alpha T \tag{6.45}
$$

$$
N_{0r} = N_{0\theta} \tag{6.46}
$$

$$
N_{rz} = N_{\theta z} = 0. \tag{6.47}
$$

These parameters were chosen assuming symmetric edge loading and bidirectional thermoelectric properties.

Applying through-the-thickness integration using Equations 4.9, and the independent variable and displacement scaling rules in Equations 4.18,the system can be collapsed to the one-dimensional problem of interest (assuming symmetric actuation and pretension, and the remaining scaling rules from Equation 4.18):

$$
\begin{aligned}
\mathbb{L} = \int_r \Bigg[&\frac{1}{2} \left[\frac{1}{\eta^2} \left(u_{,t}^2 + v_{,t}^2 \right) + w_{,t}^2 \right] \\
&- \widehat{EH}_{\epsilon z} \left[\frac{1}{r} v - v_{,r} \right] + \widehat{EH}_\epsilon \left[\left(u_{,r} + \frac{1}{r} u \right) + \frac{1}{2} w_{,r}^2 \right] \\
&- (1 - \hat{\nu}) \left[\frac{1}{r} v - v_{,r} \right]^2 - \hat{\nu} \left[\frac{1}{r} u \left(u_{,r} + \frac{1}{2} w_{,r}^2 \right) \right] \\
&- \frac{1}{2} \left[u_{,r}^2 + \frac{1}{r^2} u^2 + w_{,r}^2 \right] - \left[\frac{1}{r} u + u_{,r} + \frac{1}{2} u_{,r} w_{,r}^2 - \frac{1}{8} w_{,r}^4 \right] \\
&- \frac{1}{2} \epsilon^2 \left(w_{,rr}^2 + \frac{1}{r^2} w_{,r}^2 \right) - \widehat{D}_{12} \left(\frac{1}{2} w_{,r} w_{,rr} \right) \\
&+ EZ_{11} \left[w_{,rr} \left(u_{,r} + \frac{1}{2} w_{,r}^2 \right) + \frac{1}{r^2} u w_{,r} \right] \\
&+ EZ_{12} \left[\frac{1}{r} u w_{,rr} + \frac{1}{r} w_{,r} \left(u_{,r} + \frac{1}{2} w_{,r}^2 \right) \right] \\
&+ \left(N_z - \widehat{EZ}_\epsilon \right) \left[\frac{1}{r} w_{,r} + w_{,rr} \right] - P \left[w + \frac{1}{\eta} \left(u_{,r} w - w_{,r} u \right) \right] \Bigg] dr
\end{aligned}
\tag{6.48}
$$

where

$$
\begin{aligned}
EH_{\epsilon\theta} &= EH_{\epsilon r} \\
EZ_{\epsilon\theta} &= EZ_{\epsilon r} \\
\widehat{EH}_\epsilon &= EH_{\epsilon 11} + EH_{\epsilon 12} \\
\widehat{EZ}_\epsilon &= EZ_{\epsilon 11} + EZ_{\epsilon 12} \\
\hat{\nu} &= \frac{EH_{12}}{EH_{11}}.
\end{aligned}
\tag{6.49}
$$

6-13

Using the same method previously presented, the boundary layer areas are introduced through the stretching variables (or spatial scales):

$$u(x,t) \rightarrow u(\eta, \xi, \zeta, t; \varepsilon)$$
$$v(x,t) \rightarrow v(\eta, \xi, \zeta, t; \varepsilon) \tag{6.50}$$
$$w(x,t) \rightarrow w(\eta, \xi, \zeta, t; \varepsilon)$$

where $\eta = x$, $\xi = \frac{x}{\varepsilon}$, and $\zeta = \frac{1-x}{\varepsilon}$. Applying the chain rule to $x = x(\eta, \xi, \zeta; \varepsilon)$, the differentials are transformed:

$$\frac{d}{dx} = \frac{\partial}{\partial \eta} + \frac{1}{\varepsilon}\left[\frac{\partial}{\partial \xi} - \frac{\partial}{\partial \zeta}\right] \tag{6.51}$$

$$\frac{d^2}{dx^2} = \frac{\partial^2}{\partial \eta^2} + \frac{2}{\varepsilon}\left[\frac{\partial^2}{\partial \xi \partial \eta} - \frac{\partial^2}{\partial \zeta \partial \eta}\right] + \frac{1}{\varepsilon^2}\left[\frac{\partial^2}{\partial \xi^2} + \frac{\partial^2}{\partial \zeta^2} - 2\frac{\partial^2}{\partial \xi \partial \zeta}\right] \tag{6.52}$$

Substituting the expansions (introducing temporal scaling)

$$t = \omega\tau \tag{6.53}$$

$$T_n = \varepsilon^n \tau \tag{6.54}$$

$$\omega = \omega_0 + \varepsilon\omega_1 + \varepsilon^2\omega_2 + \cdots \tag{6.55}$$

$$N(\eta, \xi, \zeta; \varepsilon) = N_0(\eta, \xi, \zeta) + \varepsilon N_1(\eta, \xi, \zeta) + \varepsilon^2 N_2(\eta, \xi, \zeta) + \cdots \tag{6.56}$$

$$N_v(\eta, \xi, \zeta; \varepsilon) = N_{v0}(\eta, \xi, \zeta) + \varepsilon N_{v1}(\eta, \xi, \zeta) + \varepsilon^2 N_{v2}(\eta, \xi, \zeta) + \cdots \tag{6.57}$$

$$N_u(\eta, \xi, \zeta; \varepsilon) = N_{u0}(\eta, \xi, \zeta) + \varepsilon N_{u1}(\eta, \xi, \zeta) + \varepsilon^2 N_{u2}(\eta, \xi, \zeta) + \cdots \tag{6.58}$$

$$d(t; \varepsilon) = \varepsilon^2 d_2(t) + \varepsilon^3 d_3(t) + \varepsilon^4 d_4(t) + \cdots \tag{6.59}$$

$$d_v(t; \varepsilon) = \varepsilon^3 d_{v3}(t) + \varepsilon^4 d_{v4}(t) + \varepsilon^5 d_{v5}(t) + \cdots \tag{6.60}$$

$$d_u(t; \varepsilon) = \varepsilon^3 d_{u3}(t) + \varepsilon^4 d_{u4}(t) + \varepsilon^5 d_{u5}(t) + \cdots \tag{6.61}$$

$$w(\eta, \xi, \zeta, t; \varepsilon) = N(\eta, \xi, \zeta; \varepsilon)d(t; \varepsilon) \tag{6.62}$$

$$v(\eta, \xi, \zeta, t; \varepsilon) = N_v(\eta, \xi, \zeta; \varepsilon)d_v(t; \varepsilon) \tag{6.63}$$

$$u(\eta, \xi, \zeta, t; \varepsilon) = N_u(\eta, \xi, \zeta; \varepsilon)d_u(t; \varepsilon) \tag{6.64}$$

6-14

where $\omega_0 = 1$ as the original system was effectively scaled by ω_0, into Equation 6.48 produces a multiple scales Lagrangian expansion. Separating the resulting expansion into ε-order groupings, produces the now familiar Lagrangian expansion:

$$\mathbb{L} = \varepsilon^{-2}\mathbb{L}_{-2} + \varepsilon^{-1}\mathbb{L}_{-1} + \mathbb{L}_0 + \varepsilon\mathbb{L}_1 + \varepsilon^2\mathbb{L}_2 + \cdots \tag{6.65}$$

Once again, selecting the order of precision is equivalent to selecting an element in the energy expansion. Applying Euler's equations to the selected Lagrangian element produces the system of equations to produce the desired solution. The functions produced through the application of Euler's equations to $\mathbb{L}_n$ exists in the set of functions produced through the application of Euler's equations to $\mathbb{L}_m$, where $m > n$.

Again, the in-plane displacements are negligible to the order in this analysis. Additionally, the axial displacements are not present in the transverse displacement equations at the level of expansion presented. Therefore, the axial displacements will not be considered in the remaining portion of this axisymmetric membrane analysis.

The system matrices can be calculated by applying either of the shape functions presented in Appendix B. Applying the cubic C^1 shape functions and simplifying, the familiar resulting system is (damping terms added):

$$\begin{aligned}
M_0 d_{2,00} + K_0 d_2 &= \Gamma_0 \tag{6.66}\\
M_0 d_{3,00} + K_0 d_3 &= \Gamma_1 - 2M_0\left(\omega_1 d_{2,00} + d_{2,01}\right) - M_1 d_{2,00} - K_1 d_2 - C_1 d_{2,0} \tag{6.67}\\
M_0 d_{4,00} + K_0 d_4 &= -\Gamma_2 - 2M_0\left(\omega_1 d_{3,00} + d_{3,01}\right) - M_1 d_{3,00} - K_1 d_3 - C_1 d_{3,0} \tag{6.68}\\
&\quad -M_0\left[d_{2,11} + 2d_{2,02} + 4\omega_1 d_{2,01} + \left(\omega_1^2 + 2\omega_2\right)d_{2,00}\right]\\
&\quad -2M_1\left(\omega_1 d_{2,00} + d_{2,01}\right) - M_2 d_{2,00} - K_2 d_2 - C_1 d_{2,1} - C_2 d_{2,0}
\end{aligned}$$

The integral in cylindrical coordinates is

$$\int_A dA = \int_A r d\theta dr, \tag{6.69}$$

but with axisymmetric assumptions, it becomes

$$\int_A dA = 2\pi \int_r r dr \tag{6.70}$$

which results in the following multiple scales integral

$$\int_{r_1}^{r_2} f(r) r dr = \int_0^{\frac{r_2-r_1}{\epsilon}} \int_0^{\frac{r_2-r_1}{\epsilon}} \int_{r_1}^{r_2} f(\eta,\xi,\zeta) \eta d\eta \epsilon d\xi \epsilon d\zeta. \tag{6.71}$$

For simplicity, the following notation will be used to represent the multiple scales integral

$$\int_{ms} f(\eta,\xi,\zeta) d_{ms} = \int_0^{\frac{r_2-r_1}{\epsilon}} \int_0^{\frac{r_2-r_1}{\epsilon}} \int_{r_1}^{r_2} f(\eta,\xi,\zeta) \eta d\eta \epsilon d\xi \epsilon d\zeta. \tag{6.72}$$

The system stiffness matrices can now be computed through the following

$$K_0 = 2\pi \int_{ms} \left[G_1^T G_1 + F_1^T F_1 \right] d_{ms} \tag{6.73}$$

$$K_1 = 2\pi \int_{ms} \left[G_1^T G_2 + G_2^T G_1 + F_1^T F_2 + F_2^T F_1 \right] + \frac{1}{\eta} \widehat{D}_{12} \left[G_1^T F_1 + F_1^T G_1 \right] d_{ms} \tag{6.74}$$

$$\begin{aligned} K_2 = 2\pi \int_{ms} & \left[G_2^T G_2 + G_1^T G_3 + G_3^T G_1 + F_2^T F_2 + F_1^T F_3 + F_3^T F_1 \right] \\ & + \frac{1}{\eta} \widehat{D}_{12} \left[G_1^T F_2 + F_2^T G_1 + F_1^T G_2 + G_2^T F_1 \right] \\ & + \frac{1}{\eta^2} \left[G_1^T G_1 \right] - EH_{\epsilon 2} \left[G_1^T G_1 \right] d_{ms} \end{aligned} \tag{6.75}$$

where

$$\begin{aligned} F_i &= [N_{i,\xi\xi} + N_{i,\zeta\zeta} - N_{i,\xi\zeta} + 2\left(N_{i-1,\zeta\eta} - N_{i-1,\xi\eta}\right) + N_{i-2,\eta\eta}] \\ G_i &= [N_{i,\xi} - N_{i,\zeta}] + N_{i-1,\eta}. \end{aligned} \tag{6.76}$$

6-16

The system mass matrices are computed through

$$M_0 = 2\pi \int_{ms} \left[N_0^T N_0 \right] d_{ms} \tag{6.77}$$

$$M_1 = 2\pi \int_{ms} \left[N_0^T N_1 + N_1^T N_0 \right] d_{ms} \tag{6.78}$$

$$M_2 = 2\pi \int_{ms} \left[N_1^T N_1 + N_0^T N_2 + N_2^T N_0 \right] d_{ms}. \tag{6.79}$$

The forcing vectors are similarly produced:

$$
\begin{aligned}
\Gamma_0 &= 2\pi \int_{ms} -P N_0^T d_{ms} \\
\Gamma_1 &= 2\pi \int_{ms} \left[\left(N_{z3} - \widehat{EZ}_{\epsilon 3} \right) F_1^T - P N_1^T \right] d_{ms} \\
\Gamma_2 &= 2\pi \int_{ms} \left[\left(N_{z3} - \widehat{EZ}_{\epsilon 3} \right) \left(F_2^T + \frac{1}{\eta} G_1^T \right) - P N_2^T \right] d_{ms}
\end{aligned} \tag{6.80}
$$

Again, the actuation manifests itself through an axial strain term $(EA_{\epsilon 2})$ and a boundary moment term $(EZ_{\epsilon 3})$ which are evident here. The axial term modifies the system stiffness and the boundary term acts as an applied forcing term. This system can be used to analyze problem solutions unattainable through analytical methods.

Two piezoelastic laminated membrane patterns are considered and shown in Figure 6.4 with the properties in Table 6.2. The first pattern consists of an electrode etching equally splitting the radius. The second pattern has three concentric electrode etchings of equal radial lengths. More etching patterns are obviously possible, but these can provide the necessary initial insight for more complicated design considerations. These patterns will indicate the effect of increasing the electrode area as well as providing concentric rings of potential surface allowing different potentials. Both shaping and dynamic response studies can be performed.
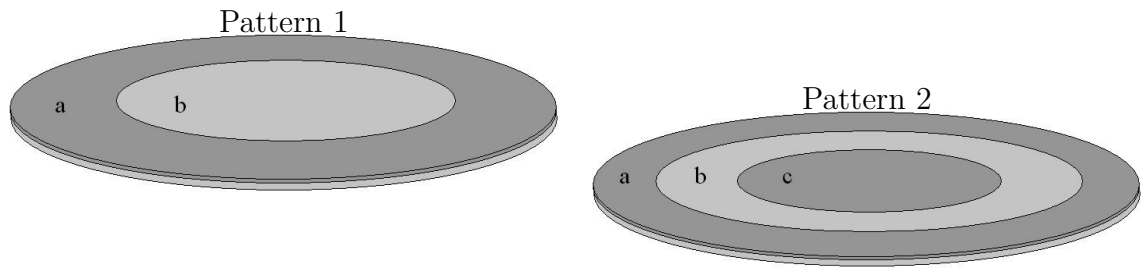
Figure 6.4   Piezoelastic Laminated Membrane Etching Patterns

Property	Kapton	PVDF
Young's Modulus (E)	406 ksi	261 ksi
Thickness Ratio (t)	0.006 in	0.003 in

Table 6.2   Membrane Element Properties

6.2.2   Static Shaping.   Chapter IV presented the use of Zernike coefficients as a good mechanism to compare the effects of shape modifications. Due to the extremely small displacements present in the membranes modelled, a reflected wavefront aberration can be approximated as twice the surface displacement. Appendix A discusses the mapping method between wavefront aberrations and Zernike coefficients.

Several configurations are presented in Table 6.3 where the sign indicates the relative voltage potential in each area. The selected grid density, as in any finite element method, plays an important role in the accuracy of the solution. Figure 6.5 presents the result of increasing the number of elements applied to a pressurized membrane. It's clear increasing the number of elements improves the apparent solution, as expected. Figure 6.6 illustrates the result of the piezoelectric effects when configuration 0 is concerned. The membrane cups, causing noticeable deflection.

Figure 6.7 presents a graphic of the shape deflection of each remaining configuration, when only piezoelectric actuation is considered. The effect of the actuation in each pattern area is clearly evident.

Figures 6.8 through 6.12 display the effects of varying edge tension, pressure, and electrical potential for each indicated configuration. While the effects are directly

6-18

Configuration	Pattern	Area a	Area b	Area c
0	1	+	+	
1	1	0	+	
2	2	0	+	+
3	2	0	+	-
4	2	0	+	0

Table 6.3   Membrane Configurations
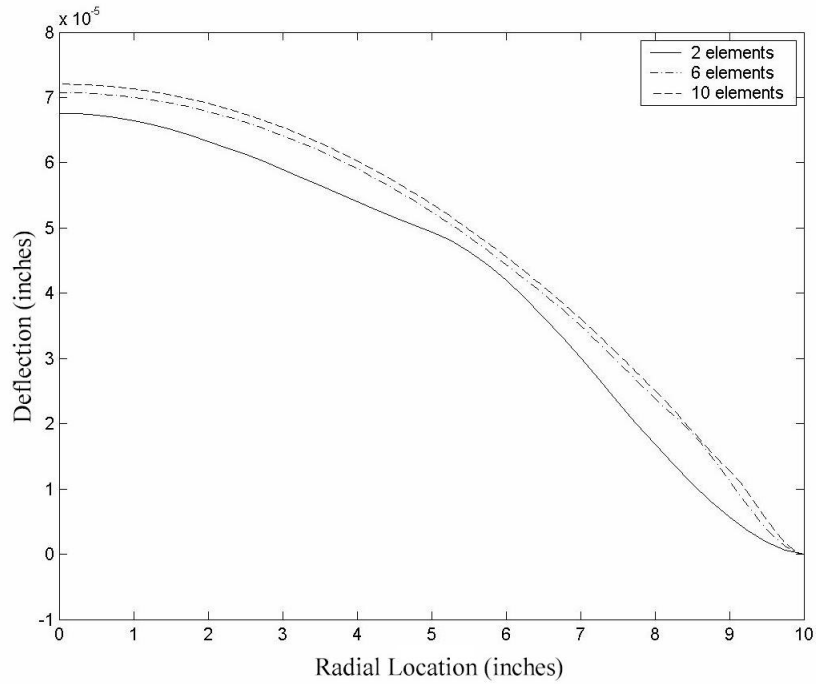
Figure 6.5   Configuration 0 Grid Density Effects (Pressurized)

proportional to the voltage applied, regardless of pattern, the effect due to increasing tension seems to drop off. This is expected, based on previously published analytical and experimental results (34, 44).

The center graphs for each configuration present the result of various tension per thickness values. The extreme left portion of these graphs are suspected numerical breakdowns due to 'boundary layer' encroachment rather than a true mechanical phenomenon.

6-19
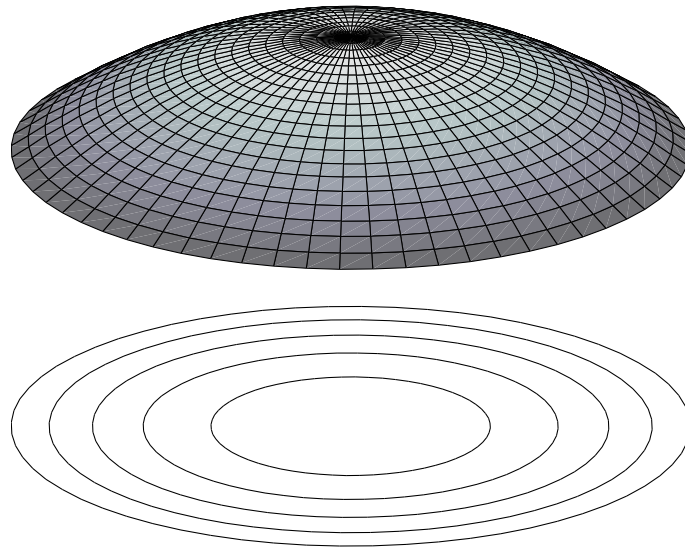
Figure 6.6   Configuration 0 Piezoactuation Effects (Unpressurized)
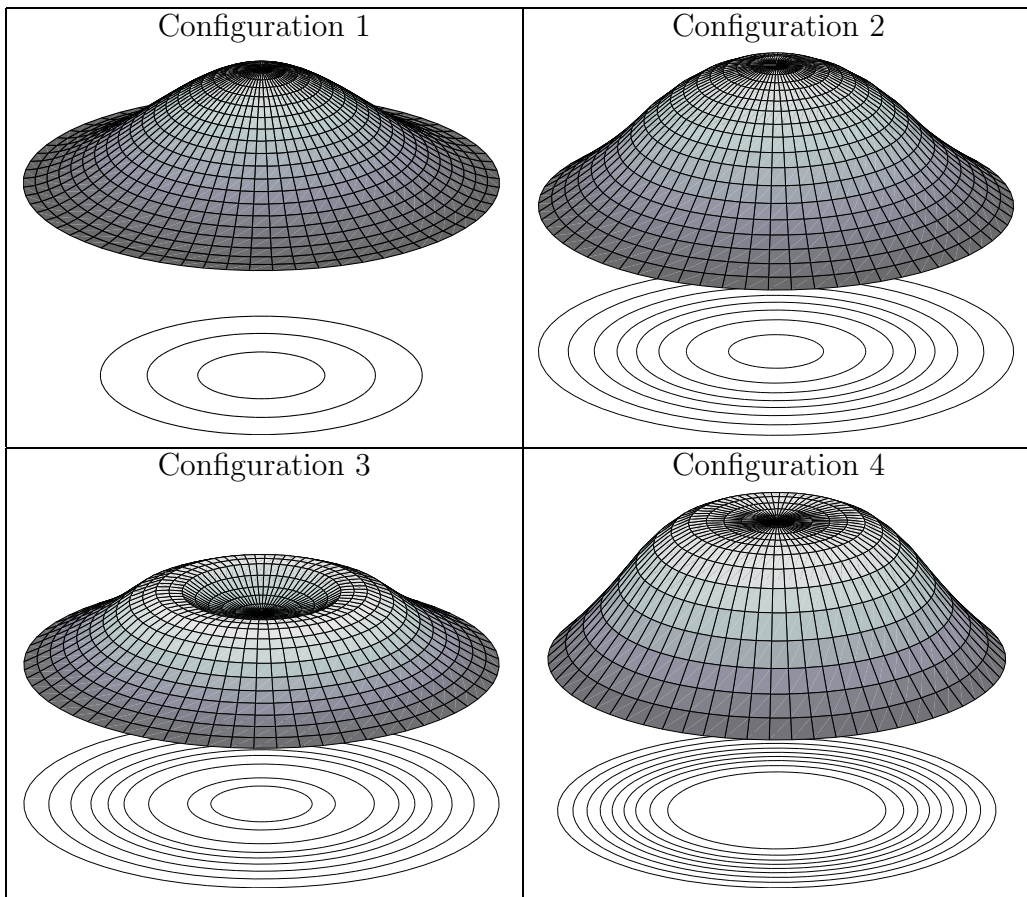
Figure 6.7   Unpressurized Piezoactuated Displacement Shapes
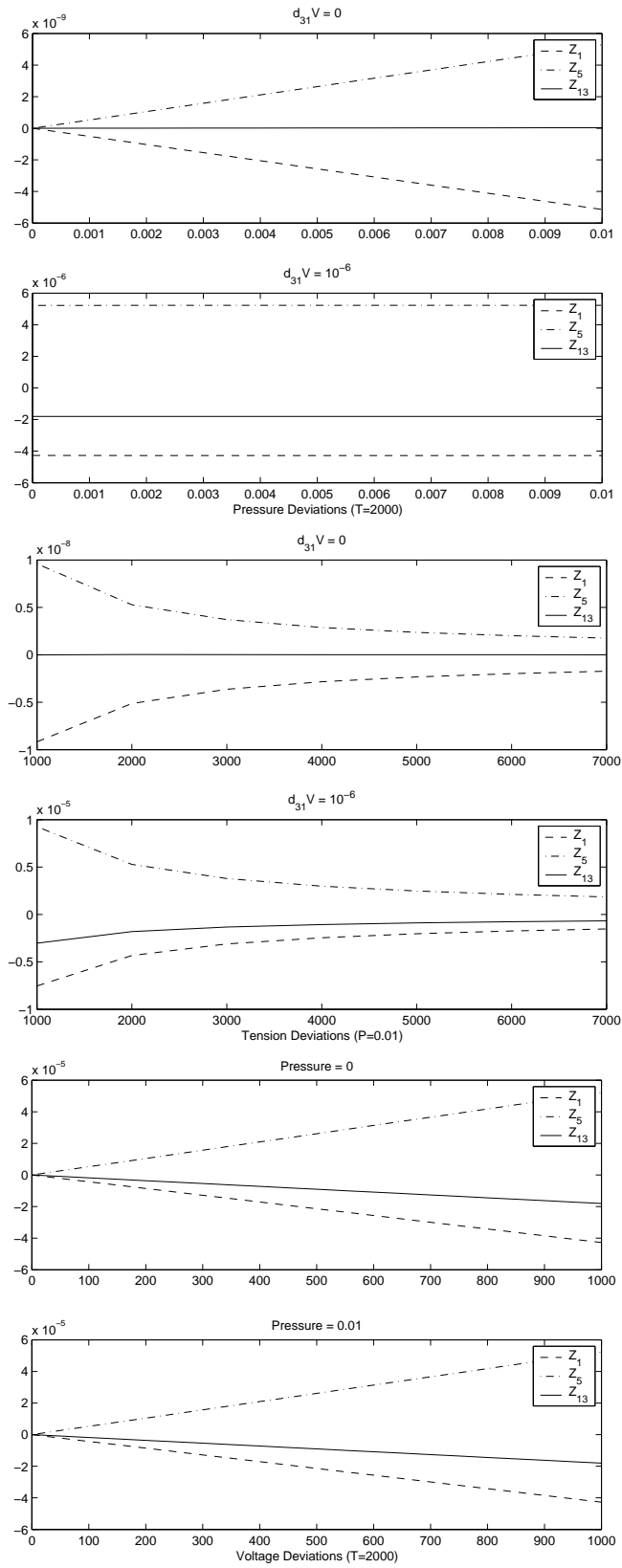
Figure 6.8   Configuration 0 Zernike Modifications (10 Elements)

6-21
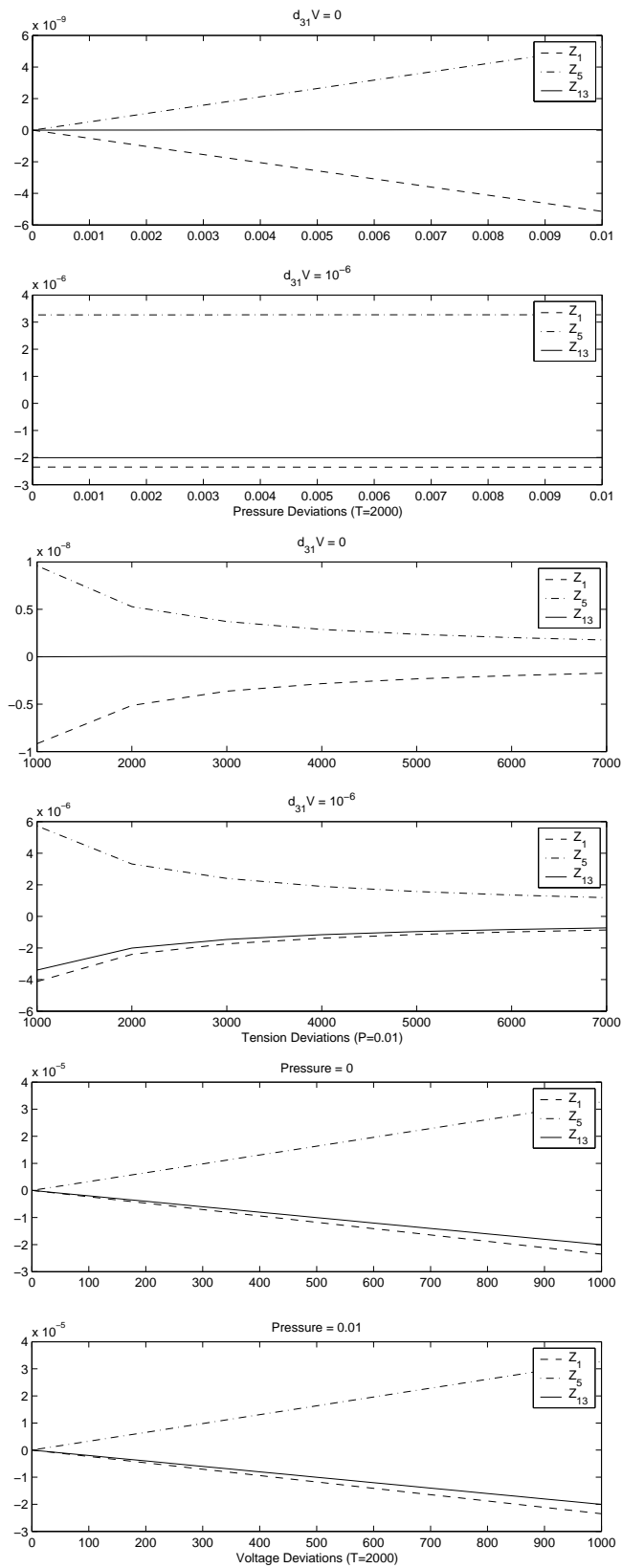
Figure 6.9   Configuration 1 Zernike Modifications (10 Elements)

6-22
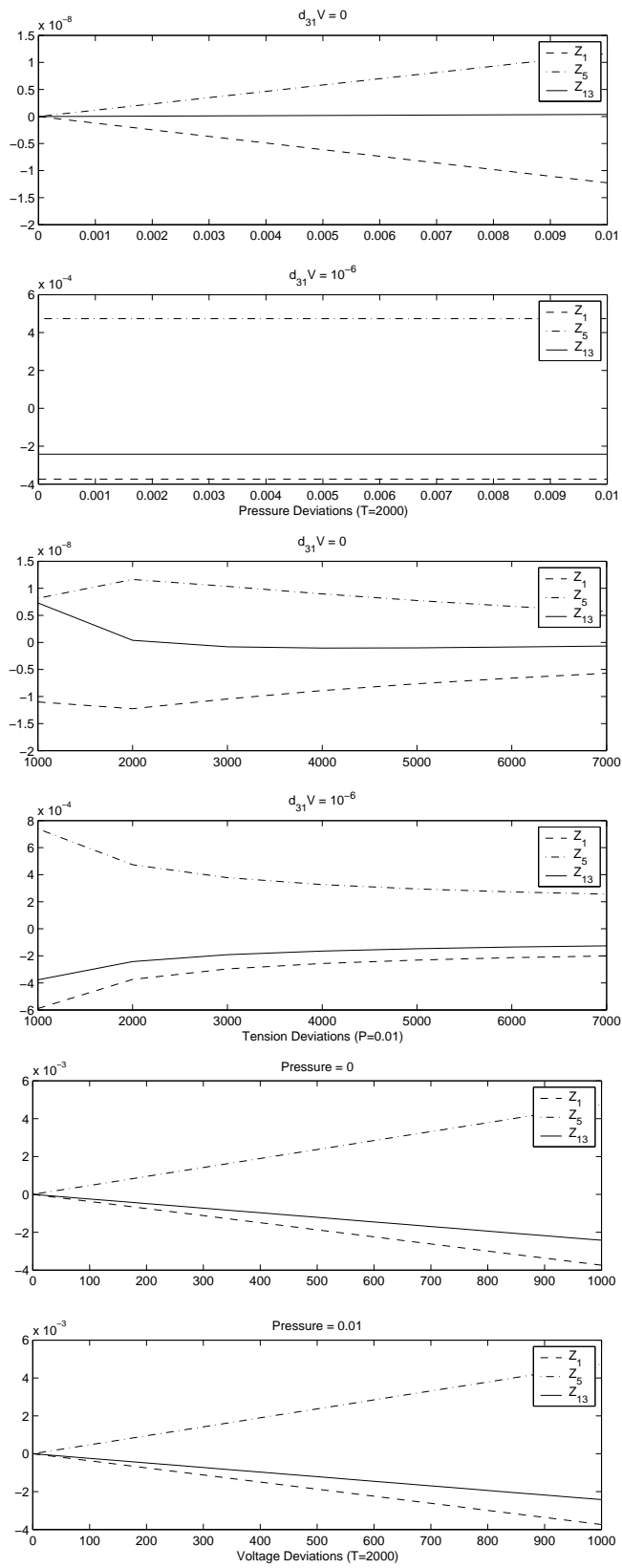
Figure 6.10   Configuration 2 Zernike Modifications (9 Elements)

6-23
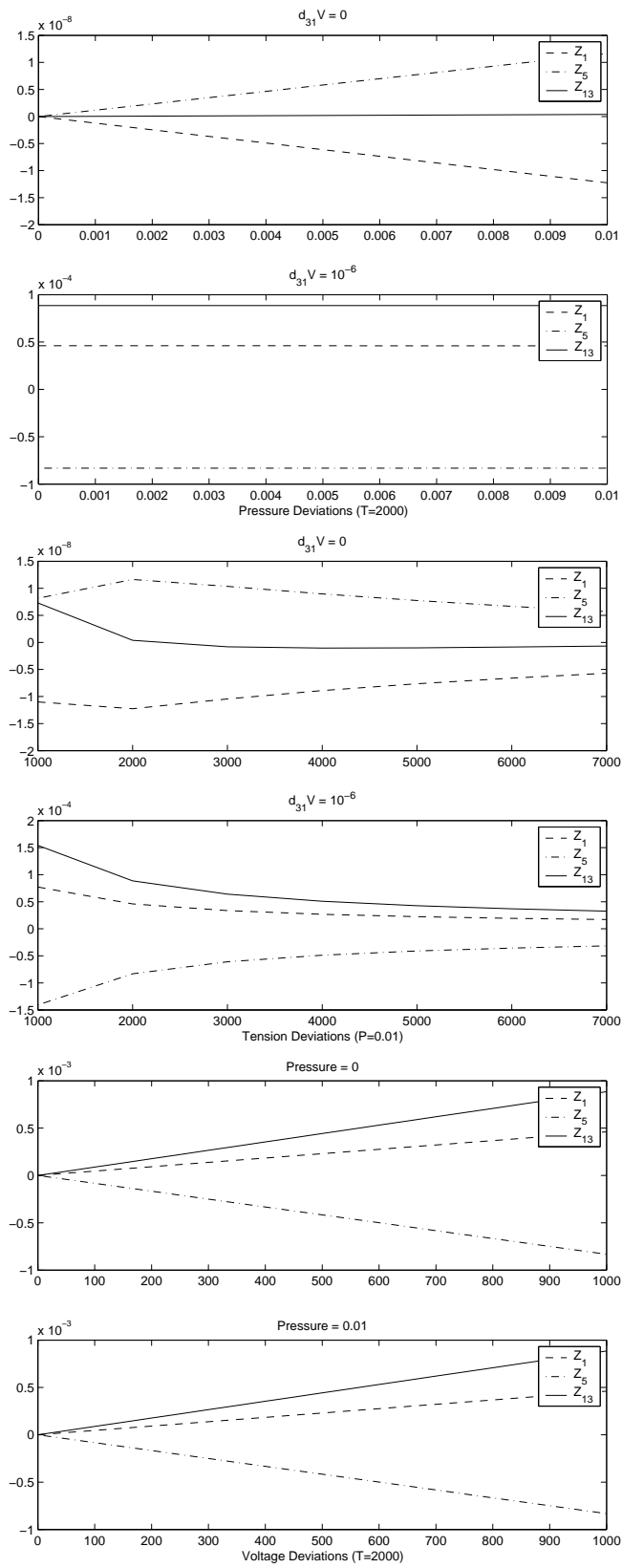
Figure 6.11   Configuration 3 Zernike Modifications (9 Elements)

6-24
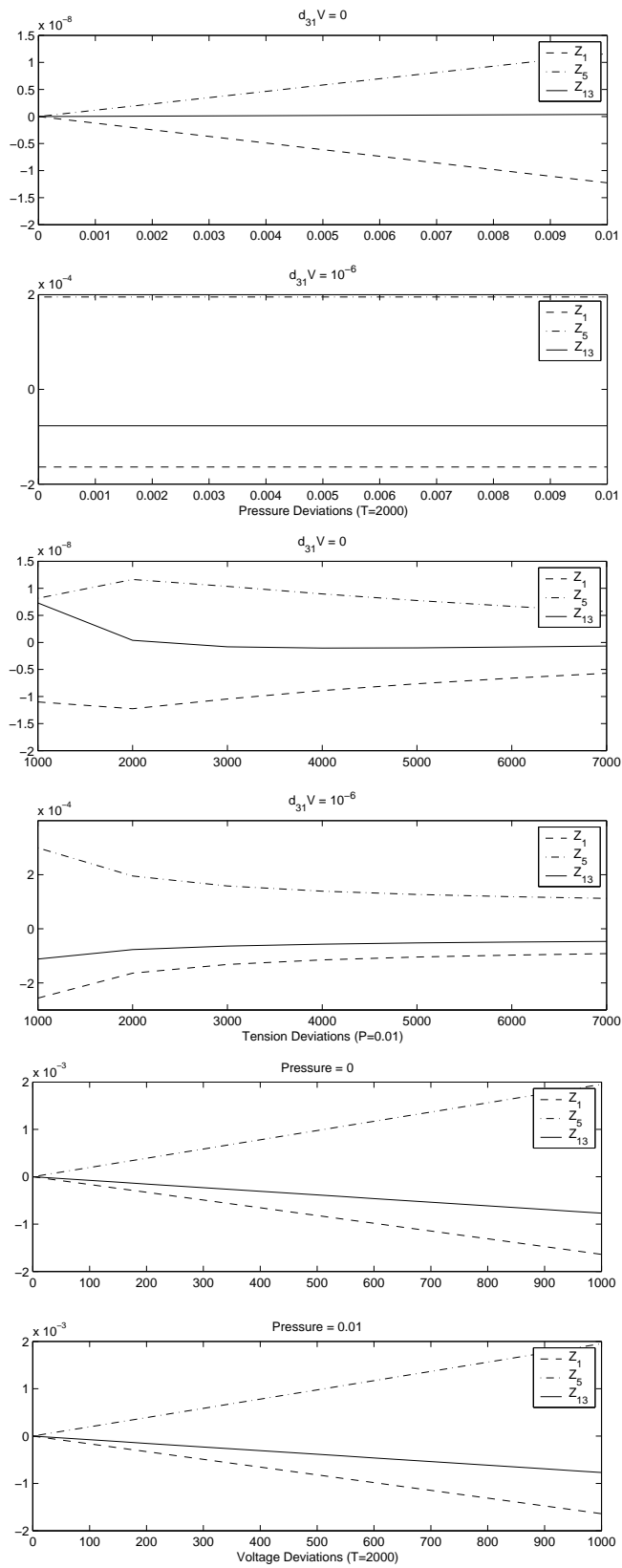
Figure 6.12   Configuration 4 Zernike Modifications (9 Elements)

6-25
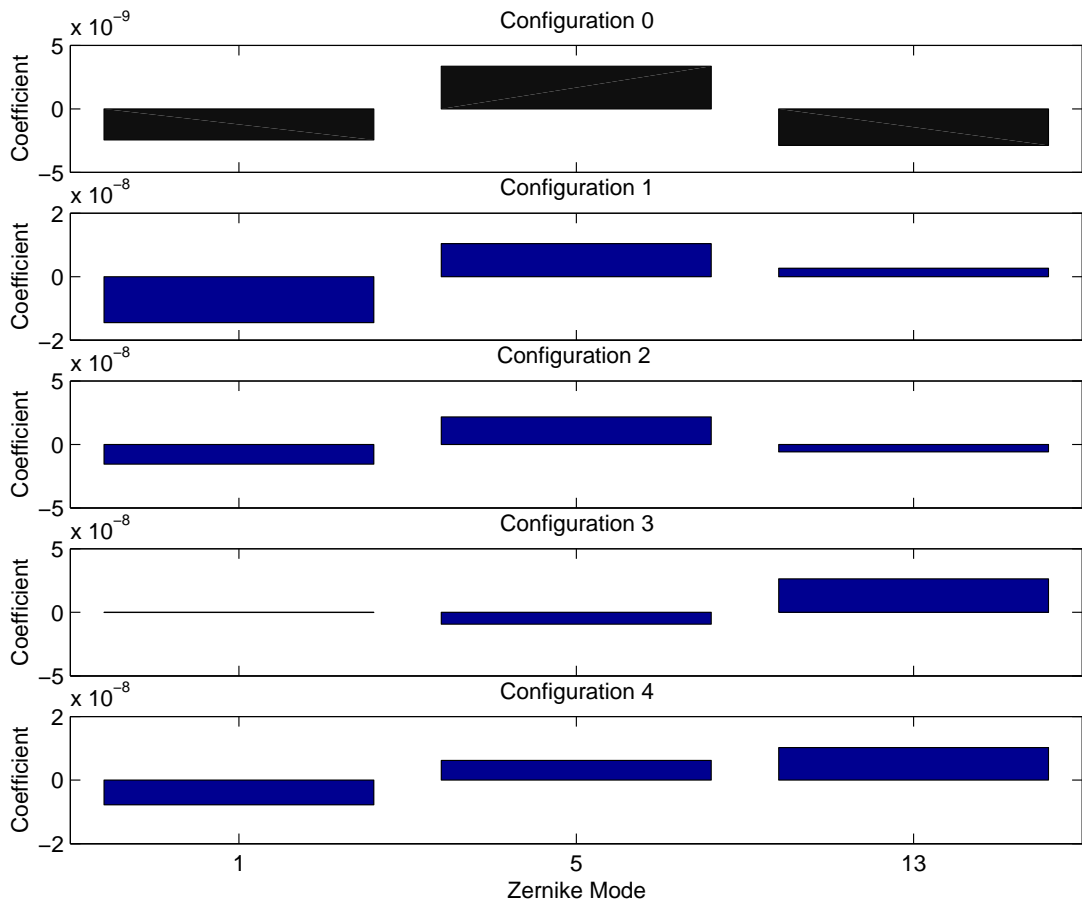
Figure 6.13   Configuration Zernike Coefficient Comparisons

Figure 6.13 illustrates the effective difference between each configuration under a 2000 lb/in tension load and applying a potential of $d_{31}V = 10^{-8}$. The effect of pattern placement seems to have greatest effect on Zernike Modes 1 and 13.

6.2.3   Natural Response.   The top graph in Figure 6.14 displays the effects of varying edge tension on the dynamic mode shapes. Notice similar results to those discussed in the previous section. Edge tension changes will have negligible effects over the global wavefront.

The bottom two graphs in Figure 6.14 display the effects of varying edge tension on the natural frequencies. Since the tension has a direct effect on the natural frequency, these are normalized to the fundamental mode. As the tension is increased,

6-26
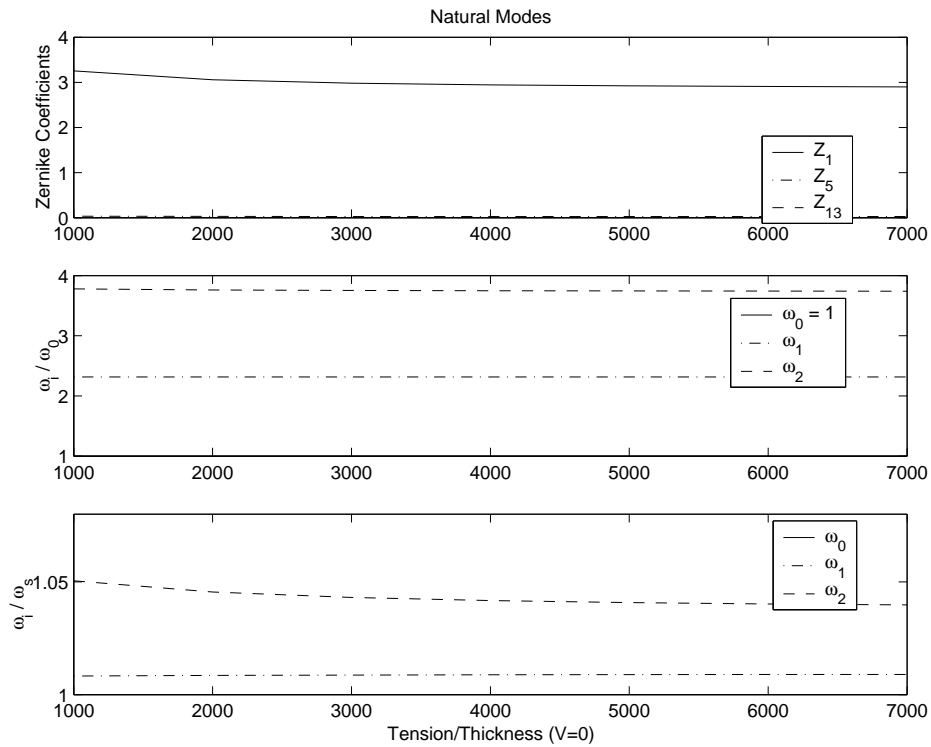
Figure 6.14   Mode Shape Zernike Changes

the frequencies approach the corresponding pure membrane modal frequencies. The middle graph presents the normalized frequency, while the lower represents the ratio of the computed frequencies to pure circular membrane frequencies. This is expected since as the tension gets very large, the 'smallness' parameter in the analysis approaches zero. This, in effect, eliminates the plate-like behavior, leaving purely membrane response.

6.2.4   Forced Response.   The forced response of an unpressurized membrane mirror is of particular interest. Removing the frequency expansion (ω_i),

the system becomes:

$$M_0 d_{2,00} + K_0 d_2 \ = \ -\hat{\Gamma}_0 \tag{6.81}$$

$$M_0 d_{3,00} + K_0 d_3 \ = \ -\hat{\Gamma}_1 - M_1 d_{2,00} - 2M_0 d_{2,01}$$
$$-K_1 d_2 - C_1 d_{2,0} \tag{6.82}$$

$$M_0 d_{4,00} + K_0 d_4 \ = \ -\hat{\Gamma}_2 - 2M_1 d_{3,00} - 2M_0 d_{3,01}$$
$$-M_2 d_{2,00} - 4M_1 d_{2,01} - M_0 d_{2,11} - 2M_0 d_{2,02}$$
$$-C_1 d_{3,0} - C_2 d_{2,0} - C_1 d_{2,1} - K_1 d_3 - K_2 d_2 \tag{6.83}$$

where periodic excitation is applied producing:

$$\hat{\Gamma}_0 \ = \ 0 \tag{6.84}$$

$$\hat{\Gamma}_1 \ = \ \Gamma_1 e^{i(\omega_k T_0 + \delta T_1)} \tag{6.85}$$

$$\hat{\Gamma}_2 \ = \ \Gamma_2 e^{i(\omega_k T_0 + \delta T_1)} \tag{6.86}$$

and the mass, stiffness and damping matrices are as previously defined. The ω_k term is the center frequency to be aligned with a specific mode, and δ term is inserted as a detuning parameter to allow analysis near that specific mode. Assuming periodic response

$$d_m = a_m \nu_m (T_1, T_2, ...) e^{i\omega T_0}, \tag{6.87}$$

Equation 6.81 represents a linear eigenvalue problem,

$$[K_0 - \lambda M_0] \nu_2 = 0 \tag{6.88}$$

where $\lambda = \omega^2$. Solutions to this equation are a set of eigenvalue, mode shape pairs (λ_j, ν_{2j}) which define the 1st order natural response of the system. Applying this result to the next level (Equation 6.82), the solution can can be attained.

6-28

Inserting Equation 6.87 into Equation 6.82:

$$a_3 \left[K_0 - \lambda M_0 \right] \nu_3 e^{i\omega T_0} = - \Gamma_1 e^{i(\omega_k T_0 + \delta T_1)}$$
$$- a_2 \left[K_1 + i\omega_j C_1 - \lambda_j M_1 \right] \nu_{2j} e^{i\omega_j T_0} \quad (6.89)$$
$$- 2i a_2 \omega_j M_0 \nu_{2j,1} e^{i\omega_j T_0}$$

For this system to balance correctly, $\omega = \omega_j = \omega_k$, removing all but the kth mode from the 1st order solution. The resulting equation becomes:

$$a_3 \left[K_0 - \lambda_k M_0 \right] \nu_3 = - \Gamma_1 e^{i\delta T_1}$$
$$- a_2 \left[K_1 + i\omega_k C_1 - \lambda_k M_1 \right] \nu_{2k} - 2i a_2 \omega_k M_0 \nu_{2k,1} \quad (6.90)$$

Further, ν_{2j} can only be a function of T_1 through the following relationship:

$$\nu_{2k} = \hat{\nu}_{2k}(T_2) e^{i\delta T_1} \quad (6.91)$$

for the system to balance correctly, leaving:

$$a_3 \left[K_0 - \lambda_k M_0 \right] \nu_3 = - \Gamma_1 - a_2 \left[K_1 + i\omega_k C_1 - \lambda_k M_1 - 2\delta\omega_k M_0 \right] \nu_{2k} \quad (6.92)$$

The right-hand-side must lie in the null-space of the adjoint of the left-hand-side. Since the left-hand-side is self-adjoint, this simply means the right-hand-side must be orthogonal to the solutions from Equation 6.88:

$$\nu_{2k}^T \left(\Gamma_1 + a_2 \left[K_1 + i\omega_k C_1 - \lambda_k M_1 - 2\delta\omega_k M_0 \right] \nu_{2k} \right) \quad (6.93)$$

The only unknown here is the amplitude of the first order response:

$$a_2 = \frac{-\nu_{2k}^T \Gamma_1}{\nu_{2k}^T \left[K_1 + i\omega_k C_1 - \lambda_k M_1 - 2\delta\omega_k M_0 \right] \nu_{2k}} \quad (6.94)$$
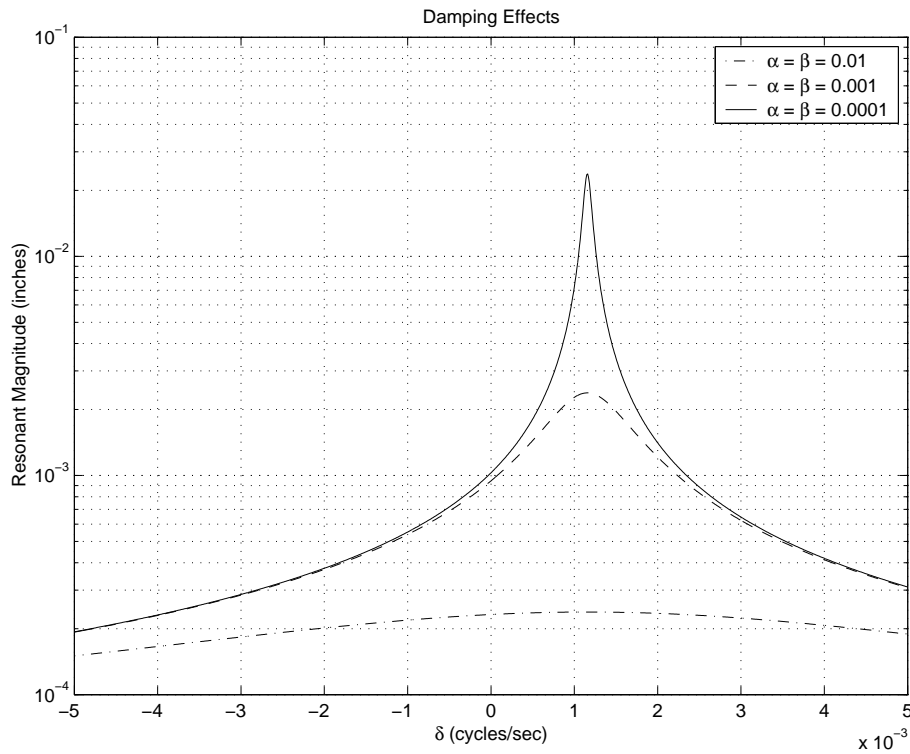
Figure 6.15   Membrane Forced Response (Damping Effects)

Applying this value back into Equation 6.92, the right-hand-side now resides only in the space remaining after removal of ν_{2k}. Because the left-hand-side of Equation 6.92, with λ_k, spans all but the space of ν_{2k}, there is a unique solution. This equation becomes:

$$a_3 \left[K_0 - \lambda_k M_0 \right] \nu_3 = B_1 \qquad (6.95)$$

where B_1 is the constant vector resulting from the insertion of the known a_2 into Equation 6.92. Solving for the a_3 terms produces the contributory responses of each mode other than ω_k. Using this method, the forced response can be approximated.

Applying this to the previously described unpressurized membrane, Figure 6.15 shows an effective shift of the first mode, regardless of damping. The damping values were chosen to illustrate the effect, not to imply actual known values. Additionally,

6-30

it's clear significantly higher deflections are possible dynamically than statically. This could imply, while a piezopolymer laminate may have limited effect for static shape corrections due to the local effects it produces, dynamically the system can provide a much stronger response. This would mean a laminate design may provide good active vibration control over the large surface area of the reflector.

6.3 Very Large Reflectors
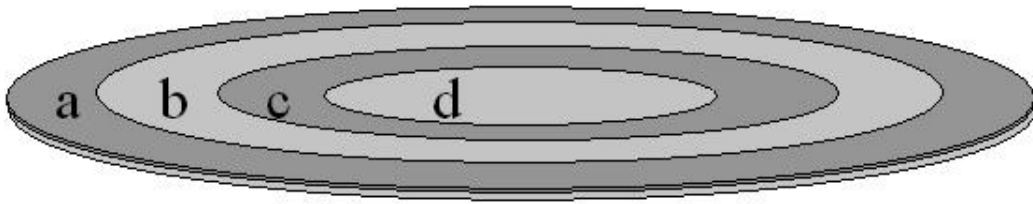
Figure 6.16   Very Large Membrane Pattern

No additional limitations have presented themselves when applying this system to a very large reflector. The pattern of 4 concentric rings of equal radial lengths shown in Figure 6.16, with actuation values defined in Table 6.4, is an example of the actuation configuration which can be created. Using the same material properties previously used and described in 6.2, while only changing the radial length to 210 inches, Figure 6.17 presents a graphic of the result of applying the graduated voltage potential to a 10 meter class reflector.

Area	$d_{31}V$
a	10^{-7}
b	$\frac{2}{3}10^{-7}$
c	$\frac{1}{3}10^{-7}$
d	0

Table 6.4   Actuation Voltages

With the significant decrease in thickness to radius ratio, the model was able to produce reasonable results with only 82 degrees of freedom. As a result, the center portion of the membrane mirror was able to produce a deflection of approximately

6-31
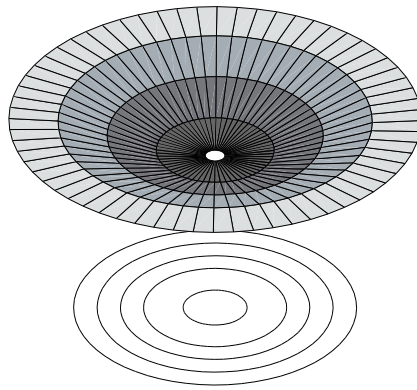
Figure 6.17   Very Large Membrane Shape

0.3 in. No attempt to optimize or find the regions where this model would break down was attempted.

This chapter presented the use of the Method of Integral Multiple Scales (MIMS) applied to nonlinear beams and axisymmetric plates. MIMS was applied through a finite element methodology producing results for systems more complicated than analytical solutions can support. A nonlinear beam-string and an axisymmetric circular membrane were modelled allowing partial electrode coverage. The partial coverage allows design flexibility to tailor the distribution to the requirement to be satisfied.

VII. Summary and Recommendations

7.1 Summary

The research herein introduced a new method to analyze piezothermoelastic laminated membranes to optical precision. The current analytical and computational analysis tools available to an analyst are either limited to homogenous materials, unable to adequately model a laminated membrane, or fundamentally based on materials of significantly higher stiffness, all resulting is significant error when optical precision is considered. A finite element approach was developed which provides extreme precision, when compared to standard tools available. This new methodology, based on the Method of Integral Multiple Scales, first introduced herein, can provide asymptotic solutions for systems containing 'small' parameters.

Chapter II presented a broad background illustrating the technical challenges addressed with this research. The Directed Energy Directorate of Air Force Research Laboratory (AFRL/DE), in concert with a variety of private industry partners, continue in their attempt to produce an inflatable optical space reflector. Focusing on static shaping, material and manufacturing limitations continue to be eliminated.

While the accuracy of a post deployment optical reflector may be achievable one day, the ability to compensate for dynamic effects resulting from the thermal environment and vibration control resulting from maneuvering requirements demand some form of active control. Most control methodologies have concentrated on edge control strategies. These methods appear far too limited for actual implementation as the effect dissipated quickly from the edge. A global method is required.

When considering optical reflectors, the ability to control the surface can be related to the reflected wavefront. From a systems point-of-view, additional technol-

ogy can be brought to bare, reducing the precision required. Real-Time Holography (RTH) is one example of a post-processing technique which may be able to correct hundreds of wavelengths of error. This significantly reduces the necessary precision of the reflector itself.

The idea of laminating layers of piezoelectric polymers on the inflatable surface is not new. These materials can modify the shape through a direct relationship between an applied actuation voltage and the material's strain. The area of actuation can be controlled by the pattern of electrode coverage on the material. Analytic solutions, however are incapable of providing solutions for realistic designs.

Finite element methods, an important structural analysis tool, can't provide accurate solutions for these systems. The weak bending stiffness and dramatically different thickness and length dimensions cause significant computational challenges. Specialized packages have been developed, providing sufficient analysis tools for simplified designs. The Finite Element Analysis of Inflatable Membrane (FAIM) and Axisymmetric Membrane (AM) codes were two such tools.

FAIM provided geometrical and material nonlinear analysis capabilities for an isotropic material, but didn't account for in-plane displacements. AM was an attempt to correct this limitation, but again assumed isotropic material and only axisymmetric designs.

Significant research has been directed toward piezothermoelastic material modeling, but are not capable of modeling membranes effectively. The vast majority of these efforts have focused on ceramic piezoelectric materials. A new modeling technique is needed allowing for the analysis of a piezothermoelastic laminated membrane.

Chapter III presented the introductory concepts through a thorough development of an analytical solution of a piezothermoelectric beam-string representing a

www.manaraa.com

cross-section of an electrically actuated inflatable structural element. The localized nature of the applied forces are clearly exhibited as small boundary layer effects.

The geometrically nonlinear equations of motion for a planar beam-string were derived from basic energy principles. The laminate effects were included by collapsing the through-the-thickness parameters to effective forces and moments acting on the beam. Using three perturbation techniques, 2nd order solutions were developed producing static shaping as well as forced response predictions for a thin piezothermoelastic laminated beam.

Chapter IV further expanded this development to a circular plate-membrane model. A circular piezothermoelastic membrane of per-layer isotropic material was modelled. The equations of motion for the laminate in cylindrical coordinates were derived. Using the methodology developed in Chapter III, the solution for an axisymmetric piezothermoelastic membrane was produced. The effects actuating forces have on a reflected wavefront were discussed through the presentation or Zernike coefficient values. Since optical reflectors are the ultimate goal, this method provided a better comparison.

Chapter V presented the development of a new finite element method using asymptotic expansion theory. The Method of Integral Multiple Scales (MIMS) was introduced, and a linear beam model was to illustrate this novel method. A static solution method as well as dynamic response were discussed, including damping effects. The result of this method was compared to both an independently produced analytical prediction as well as a standard finite element method prediction. MIMS produced a predicted solution over three orders of magnitude more accurate than the standard finite element methodology.

Chapter VI expanded this method into the solution of nonlinear problems of concern in this research. MIMS was applied to the nonlinear beam and circular plate problems presented in Chapters III and IV. It was discovered that the method itself is not altered for nonlinear problems. While a nonlinear first order equation is often

the result in a perturbation approach, due to the parameters in the problem studied herein, no such problem occurred. All levels continue to produce linear equations.

Due to the actuation applied, MIMS was expanded to investigate the forced response of the laminated axisymmetric membrane. It was observed that significantly higher response amplitude resulted from dynamic actuation than from static. This implies possible use for active vibration control. Additionally, a very large 10 meter class antenna was modelled, indicating surface deflections of thousands of wavelengths of deflection is available for such a large reflector.

MIMS may not be limited to just energy-based Lagrangian; it was only studied for that specific application here. The concept might be applicable to a wider range of applications. It can, however, clearly add to the structural analysis toolkit of an analyst when structures with very low bending stiffness are concerned, such as an inflatable structure.

Inflatable space structures has been an enabling technology for almost fifty years. From ECHO I to the Inflatable Antenna Experiment (IAE), various solutions have relied on this technology, as do future systems such as the Next Generation Space Telescope (NGST). The goal of using inflatable structures as optical reflectors pushes the industry's limitations far beyond its current capabilities. The information contained herein should provide additional analysis tools useful in moving closer toward that goal.

7.2   Recommendations for Future Research

1. As with all mathematical or computational results, experimental validation is the only true measure of accuracy. Current manufacturing limitations hinder the creation of the membranes studied in this research.

   (a) Expanding Wagner's research (17) to include multiple axisymmetric rings can verify correct model shaping predictions.

(b) Further experimental research should be focused on dynamic response and active damping within a vacuum.

2. The assumed orders of magnitude for the parameters used in the mechanics development herein were specifically tailored to the problem at hand. Significant research opportunities exist expanding these assumptions for broader applications.

3. The new Method of Integral Multiple Scales (MIMS) clearly appears to be rich with future research directions. The wealth of reference material relating to multiple scales should be applied toward MIMS in an effort to evaluate its functional space.

4. MIMS appears most appropriate when applied through a finite element procedure. This application has many research paths. A couple are mentioned here:

   (a) Using the methods presented herein, triangular and rectangular element methodologies should be produced to support arbitrary geometries. This would allow analysis of framing designs using tubular structures, or even large scale sheets such as solar sails.

   (b) Analysis of arbitrary circular piezothermoelastic membrane reflectors through the finite element method would allow the creation of a comprehensive design capability.

5. The methodology presented herein required each element to have the same ε value. To be truly useful as a general purpose methodology, the relaxation of this requirement should be studied.

   (a) Directly relating the global 'smallness' parameter to the elemental expansion parameter in the shape functions could allow varying element sizes.

   (b) Further expanding this approach, the method should be expanded to handle different types of elements.

7-5

Through the development of these contributions, a comprehensive set of analytical and numerical solutions are presented to aid in the further development of inflatable optical reflectors. The introduction of MIMS promises far-reaching impact as a solution methodology for many areas beyond the specific application herein.

Appendix A. Structural Modes vs. Optical Modes

Optical membrane reflectors are often analyzed from a purely structural point-of-view. From a systems view, the structural response is important, but only to the extent that it impacts the overall mission. An optical reflector, whether a thin membrane or a glass mirror, is only as good as the wavefront produced. Mechanical analysis of a circular membrane includes the dynamic vibration modes, while an optical analysis would include the wavefront aberrations.

In this appendix, vibration modes of a circular membrane are introduced as well as a common mathematical wavefront definition using a series of orthogonal Zernike functions. A section is also included which presents a method to map structural shapes to these Zernike polynomials. A direct mapping is only available for continuous functions. Using intermediate functions, based on Zernike functions, the mapping can be accomplished.

A.1 Vibration Modes

Circular membrane displacement can be represented mathematically, after scaling, by the two-dimensional wave equation:

$$\frac{\partial^2}{\partial t^2} w(r, \theta, t) - \nabla^2 w(r, \theta, t) = 0 \tag{A.1}$$

where

$$\nabla^2 = \frac{\partial^2}{\partial r^2} + \frac{1}{r}\frac{\partial}{\partial r} + \frac{1}{r^2}\frac{\partial^2}{\partial \theta^2}. \tag{A.2}$$

The solution to this equation, found in any advanced mathematics textbook, results in a system of orthonormal circular membrane vibration mode shapes in terms of

A-1

Bessel functions (70):

$$W_{0n}\left(r,\theta\right) = A_{0n}\mathrm{J}_0\left(\beta_{0n}r\right), \qquad n = 1, 2, \dots$$

$$W_{mnc}\left(r,\theta\right) = A_{mnc}\mathrm{J}_m\left(\beta_{mn}r\right)\cos m\theta, \quad m, n = 1, 2, \dots \qquad (A.3)$$

$$W_{mns}\left(r,\theta\right) = A_{mns}\mathrm{J}_m\left(\beta_{mn}r\right)\sin m\theta, \quad m, n = 1, 2, \dots$$

or in normalized dimensional form:

$$W_{0n}\left(r,\theta\right) = \frac{1}{\sqrt{\pi\rho a}\mathrm{J}_1(\beta_{0n}a)}\mathrm{J}_0\left(\beta_{0n}r\right), \qquad n = 1, 2, \dots$$

$$W_{mnc}\left(r,\theta\right) = \frac{\sqrt{2}}{\sqrt{\pi\rho a}\mathrm{J}_{m+1}(\beta_{mn}a)}\mathrm{J}_m\left(\beta_{mn}r\right)\cos m\theta, \quad m, n = 1, 2, \dots \qquad (A.4)$$

$$W_{mns}\left(r,\theta\right) = \frac{\sqrt{2}}{\sqrt{\pi\rho a}\mathrm{J}_{m+1}(\beta_{mn}a)}\mathrm{J}_m\left(\beta_{mn}r\right)\sin m\theta, \quad m, n = 1, 2, \dots$$

These modes are orthogonal through the relationship:

$$\int_0^{2\pi}\int_0^1 W_{m,j}(r,\theta)W_{m,k}(r,\theta)r\,dr\,d\theta = \delta_{ij} \qquad (A.5)$$

over the unit circle, where δ_{ij} is the kronecker delta.

The $\beta_m n$ values represent the zeros of the corresponding Bessel function J_m. Figure A.1 illustrates a few of these modes for given values of m and n. The double images for m values over zero correspond to the sine and cosine shapes in Equation A.4.

A.2   Optical Modes

If the transverse displacement of the circular membrane is very small, this distortion can be treated as half of the distortion imparted on a wavefront after reflection. Circular wavefronts, however, are often represented by different families of orthogonal functions. The Zernike polynomial series is a commonly used set (71).

n:m	0	1	2	3
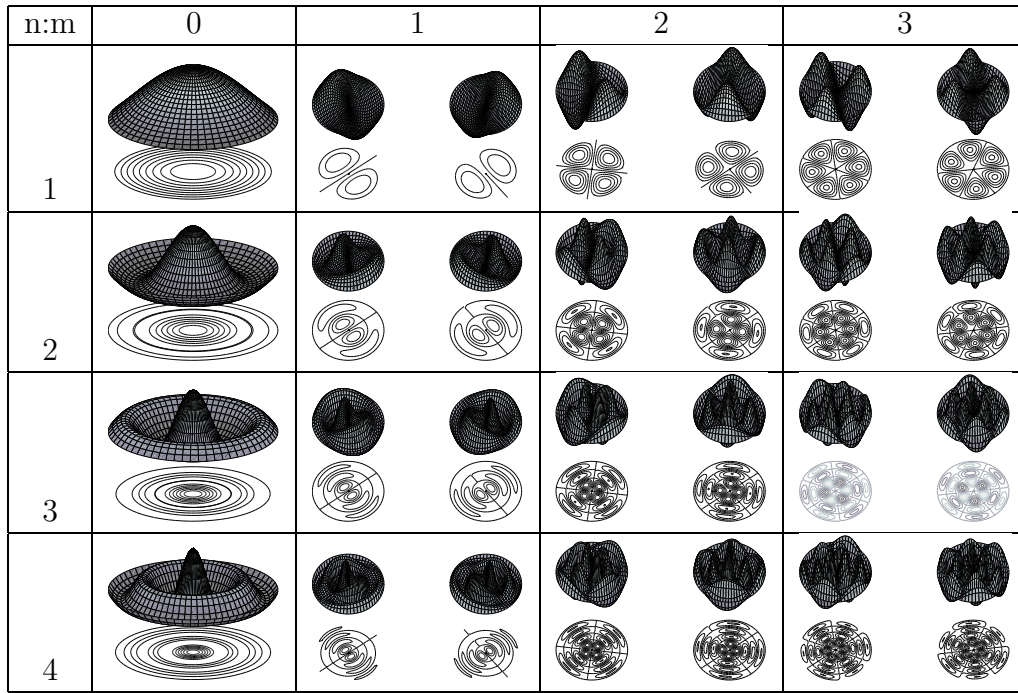
Figure A.1   Membrane Vibration Modes

This family allows the wavefront distortion to be defined as:

$$w(\rho,\theta) = \sum_{n=0}^{k}\sum_{m=0}^{n} A_{mn}U_{mn}(\rho,\theta) = \sum_{r=0}^{L} A_r U_r(\rho,\theta) \tag{A.6}$$

where L represents the maximum power. The relationship between r and n, m can be represented by:

$$r = \frac{n(n+1)}{2} + m + 1 \tag{A.7}$$

which is not a unique mapping, but is used here. The Zernike 'modes', U_{nm}, are represented by

$$U_{nm}(\rho,\theta) = R_{mn}(\rho)\left[\frac{\sin}{\cos}\right](n-2m)\theta \tag{A.8}$$

where

$$R_{mn}(\rho) = \sum_{s=0}^{m}(-1)^s \frac{(n-s)!}{s!(m-s)!(n-m-s)!}\rho^{(n-2s)}. \tag{A.9}$$

A-3

n:m	0	1	2	3	4
0					
1					
2					
3					
4					
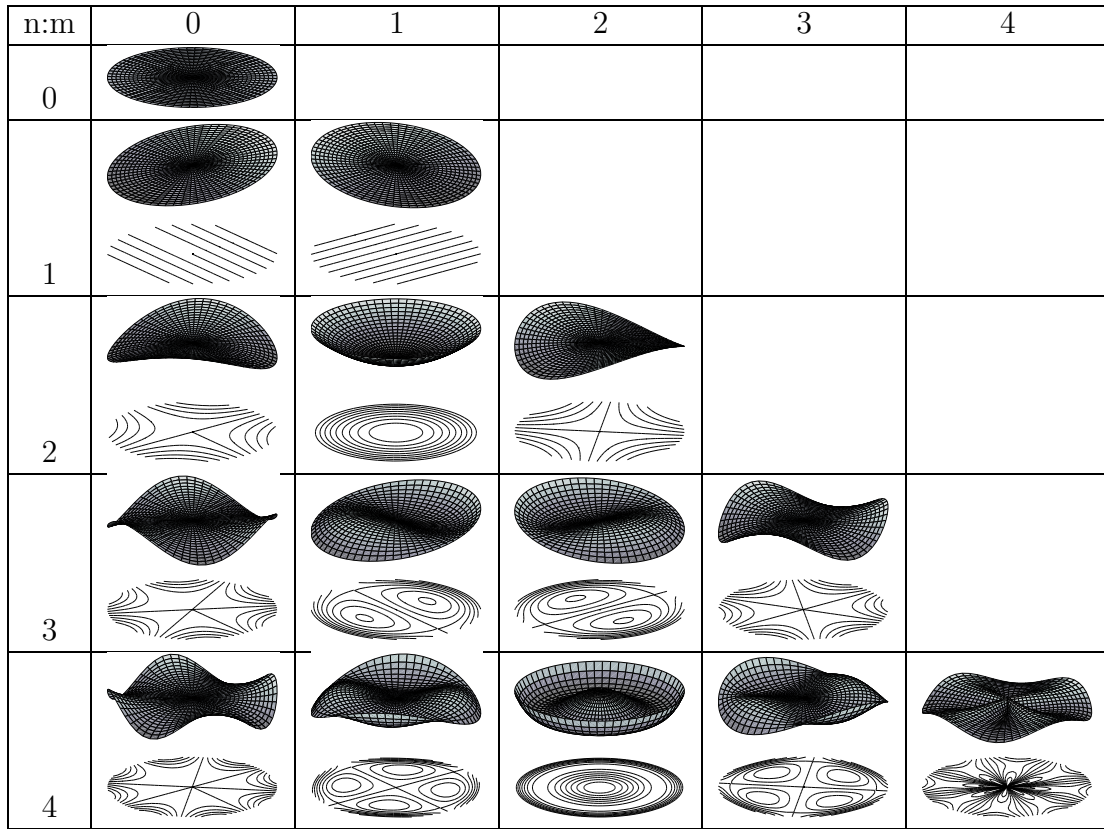
Figure A.2   Zernike Modes

When $n - 2m > 0$, the antisymmetric function (sin) is used. When $n - 2m < 0$, the symmetric function (cos) is used. Note: Only positive powers of ρ are maintained.

These modes are orthogonal through the relationship:

$$\int_0^{2\pi} \int_0^1 U_{mj}(\rho, \theta) U_{mk}(\rho, \theta) \rho d\rho d\theta = \frac{\pi}{2(n+1)} \delta_{jk} \tag{A.10}$$

over the unit circle.

Figure A.2 illustrates the Zernike modes for given m and n values. The upper three-dimensional plot in each cell represents an actual planar wavefront if an aberration of the corresponding Zernike function exists. Under each plot is a contour plot of the surface indicating the type of pattern such a wavefront would produce in an interferometer. A cursory comparison between figures A.1 and A.2 indicates a

A-4

n	m	r	w_{01}	w_{02}	w_{03}	w_{04}	w_{05}	w_{06}	Z_r
0	0	1	1.728	-0.494	0.25	-0.158	0.110	-0.084	1
1	0	2	0	0	0	0	0	0	$\rho \sin(\theta)$
1	1	3	0	0	0	0	0	0	$\rho \cos(\theta)$
2	0	4	0	0	0	0	0	0	$\rho^2 sin(2\theta)$
2	1	5	-1.986	-1.090	0.672	-0.446	0.32	-0.244	$2\rho^2 - 1$
2	2	6	0	0	0	0	0	0	$\rho^2 \cos(2\theta)$
3	0	7	0	0	0	0	0	0	$\rho^3 \sin(3\theta)$
3	1	8	0	0	0	0	0	0	$(3\rho^3 - 2\rho) \sin(\theta)$
3	2	9	0	0	0	0	0	0	$(3\rho^3 - 2\rho) \cos(\theta)$
3	3	10	0	0	0	0	0	0	$\rho^3 \cos(3\theta)$
4	0	11	0	0	0	0	0	0	$\rho^4 \sin(4\theta)$
4	1	12	0	0	0	0	0	0	$(4\rho^4 - 3\rho^2) \sin(2\theta)$
4	2	13	0.272	2.34	0.134	-0.396	0.378	-0.326	$6\rho^4 - 6\rho^2 + 1$
4	3	14	0	0	0	0	0	0	$(4\rho^4 - 3\rho^2) \cos(2\theta)$
4	4	15	0	0	0	0	0	0	$\rho^4 \cos(4\theta)$

Table A.1   Zernike Decomposition of Symmetric Vibration Modes

relationship should exist. A mapping between vibration modes and Zernike modes can therefore easily be created through application of orthogonality principles.

Table A.1 presents the decomposition of the first few vibration modes. As expected, the w_{0n} vibration modes only affect the purely radial Zernike modes. Likewise the harmonic modes are mapped to like Zernike harmonics. While continuous wavefront definitions can be directly correlated through the previous orthogonality relationships, a direct correlation between arbitrary discretized wavefronts and Zernike polynomial coefficients is not quite as straight forward.

A.3   Numerical Wavefront Zernike Polynomial Determination

Determination of the Zernike polynomial coefficients representing the circular wavefront aberrations using a least-squares method requires intermediate orthogonal polynomials. The remainder of this section is modified slightly from Malacara (71).

A-5

Given N measured points with coordinates (ρ_n, θ_n) and corresponding wavefront displacements W'_n measured with respect to a closed analytical function $W(\rho, \theta)$, the discrete variance v^2 can be defined as:

$$v^2 = \frac{1}{N} \sum_{n=1}^{N} [W'_n - W(\rho_n, \theta_n)] \tag{A.11}$$

In the case considered here, the analytic function can be represented as a linear combination of predefined functions, $V_r(\rho, \theta)$, to be defined later:

$$W(\rho_n, \theta_n) = \sum_{r=1}^{L} B_r V_r(\rho_n, \theta_n) \tag{A.12}$$

The best least squares fit is then calculated by minimizing the variation:

$$\frac{\partial v}{\partial B_p} = 0 \tag{A.13}$$

where $p = 1, 2, \ldots, L$, which produces:

$$\sum_{r=1}^{L} B_r \sum_{n=1}^{N} V_r(\rho_n, \theta_n) V_p(\rho_n, \theta_n) = \sum_{n=1}^{N} W'_n V_p(\rho_n, \theta_n) = 0 \tag{A.14}$$

Requiring V_r to satisfy the following orthogonality condition:

$$\frac{\sum_{n=1}^{N} V_r(\rho_n, \theta_n) V_p(\rho_n, \theta_n)}{\sum_{n=1}^{N} V_p^2(\rho_n, \theta_n)} = \delta_{rp} \tag{A.15}$$

where δ_{rp} is the kronecker delta. Using this relationship, the coefficients B_r can be calculated:

$$B_r = \frac{\sum_{n=1}^{N} W'_n V_p(\rho_n, \theta_n)}{\sum_{n=1}^{N} V_p^2(\rho_n, \theta_n)} \tag{A.16}$$

A-6

Using Gram-Schmidt Orthogonalization, the intermediate polynomials can be computed using the following relationship:

$$V_r(\rho, \theta) = U_r(\rho, \theta) + \sum_{s=1}^{r-1} D_{rs} V_s(\rho, \theta) \tag{A.17}$$

where $r = 1, 2, \ldots, L$. Using the orthogonality principle (Equation A.15, we can derive the D_{rs} coefficients:

$$D_{rs} = -\frac{\sum_{n=1}^{N} U_r(\rho_n, \theta_n) V_p(\rho_n, \theta_n)}{\sum_{n=1}^{N} V_p^2(\rho_n, \theta_n)} \tag{A.18}$$

where $r = 2, 3, \ldots, L$ and $p = 1, 2, \ldots, r-1$.

A corresponding linear combination of Zernike polynomials:

$$W(\rho, \theta) = \sum_{r=1}^{L} A_r U_r(\rho, \theta) \tag{A.19}$$

can now be defined using the coefficient definition:

$$A_r = B_r + A_q D_{qs} \tag{A.20}$$

where $r = 1, 2, \ldots, L$, $q = r + 1$, and $A_z = 0 \forall z < 0$. Based on his procedure, Zernike polynomial coefficients for arbitrary wavefronts can be computed.

Appendix B. Asymptotic Shape Functions

Application of the finite element method to a given problem is a balance between required output precision and computational resources available. The finite element method involves substituting an assumed shape function/unknown displacement pair for all dependent variables to be approximated. The simple one dimensional string or rod model may use C^0 elements since the functions defining their motion are functions of only position. An example of a C_0 shape function vector is (65):

$$N(x)^T = \begin{pmatrix} \frac{L-s}{L} \\ \frac{L-s}{L} \end{pmatrix} \tag{B.1}$$

The linear nature of this function means values are linearly interpolated. Elements created from this class of shape functions can not model nodal slopes, but may produce adequate results through post-processing adjustments. C^0 elements, however, are not adequate if the boundary conditions will be imposed through displacement rates. More complicated C^1 shape functions can be applied, but increase element matrix size, and therefore computational speed can dramatically decrease. An example of a standard C^1 shape function vector is (65):

$$N(x)^T = \begin{pmatrix} 1 - \frac{3x^2}{L^2} + \frac{2x^3}{L^3} \\ x - \frac{2x^2}{L} + \frac{x^3}{L^2} \\ \frac{3x^2}{L^2} - \frac{2x^3}{L^3} \\ -\frac{x^2}{L} + \frac{x^3}{L^2} \end{pmatrix} \tag{B.2}$$

If a beam-string solution requires C^1 class shape functions, but is far too flexible and causes locking problems when using standard C^1 shape functions, another

method is necessary. In an attempt to provide a better solution method, elements which behave as beam-strings can better represent an extremely flexible structure.

B.1 Linear C^1 Beam String Shape Functions

A simple beam-string of unit length with smallness parameter ε can be defined by the scaled static equation of motion:

$$\varepsilon^2 \frac{d^4 N}{dx^4} - \frac{d^2 N}{dx^2} = 0 \tag{B.3}$$

with boundary conditions

$$N(0) = \alpha \quad \frac{dN}{dx}\Big|_{x=0} = \beta \quad N(1) = \gamma \quad \frac{dN}{dx}\Big|_{x=1} = \delta. \tag{B.4}$$

From Chapter III, a beam-string solution can be constructed using the method of matched asymptotic expansions. The outer and inner solutions have the form:

$$\begin{aligned}
N^o(\eta) &= \sum_{i=0}^{n} \varepsilon^i \left[a_{i0} + a_{i1}\eta \right] \\
N^i(\xi) &= \sum_{i=0}^{n} \varepsilon^i \left[b_{i0} + b_{i1}\xi + b_{i2}\mathrm{e}^{-\xi} \right] \\
N^I(\zeta) &= \sum_{i=0}^{n} \varepsilon^i \left[c_{i0} + c_{i1}\zeta + c_{i2}\mathrm{e}^{-\zeta} \right]
\end{aligned} \tag{B.5}$$

where the boundary conditions now become:

$$\begin{aligned}
N_0(0) = \alpha \quad & \frac{dN_0}{d\xi}\Big|_{\xi=0} = 0 \quad N_0(1) = \gamma \quad & \frac{dN_0}{d\zeta}\Big|_{\zeta=0} = 0 \\
N_1(0) = 0 \quad & \frac{dN_1}{d\xi}\Big|_{\xi=0} = \beta \quad N_1(1) = 0 \quad & \frac{dN_1}{d\zeta}\Big|_{\zeta=0} = -\delta \\
N_j(0) = 0 \quad & \frac{dN_j}{d\xi}\Big|_{\xi=0} = 0 \quad N_j(1) = 0 \quad & \frac{dN_j}{d\zeta}\Big|_{\zeta=0} = 0
\end{aligned} \tag{B.6}$$

for all $j > 1$, where $\eta = x$, $\xi = \frac{x}{\varepsilon}$ and $\zeta = \frac{1-x}{\varepsilon}$. Applying boundary conditions to the inner solutions, then matching to the outer solutions, of each order i in succession

Shape Function	$w(0)$	$w_{,x}(0)$	$w(1)$	$w_{,x}(1)$
Boundary Condition	α	β	γ	δ
N_1	1	0	0	0
N_2	0	1	0	0
N_3	0	0	1	0
N_4	0	0	0	1

Table B.1   Linear C^1 Shape Function Boundary Conditions

results in the following asymptotic beam-string solution:

$$
\begin{aligned}
N(\eta, \xi, \zeta; \varepsilon) =& \alpha + (\gamma - \alpha)\, \eta \\
&+ \varepsilon \left[(\alpha - \gamma + \beta) + (2\gamma - 2\alpha - \beta - \delta)\, \eta \right. \\
&+ \left. (\gamma - \alpha - \beta)\, \mathrm{e}^{-\xi} + (\alpha - \gamma + \delta)\, \mathrm{e}^{-\zeta} \right] \\
&+ \varepsilon^2 \left[(2\alpha - 2\gamma + \beta - \delta) + (4\gamma - 4\alpha - 2\beta - 2\delta)\, \eta \right. \\
&+ \left. (2\gamma - 2\alpha - \beta - \delta)\, \mathrm{e}^{-\xi} + (2\alpha - 2\gamma + \beta + \delta)\, \mathrm{e}^{-\zeta} \right] \\
&+ \varepsilon^3 \left[(4\alpha - 4\gamma + 2\beta - 2\delta) + (8\gamma - 8\alpha - 4\beta - 4\delta)\, \eta \right. \\
&+ \left. (4\gamma - 4\alpha - 2\beta - 2\delta)\, \mathrm{e}^{-\xi} + (4\alpha - 4\gamma + 2\beta + 2\delta)\, \mathrm{e}^{-\zeta} \right] + \cdots
\end{aligned}
\tag{B.7}
$$

where

$$
\begin{aligned}
\alpha &= w(0) & \gamma &= w(1) \\
\beta &= w_{,x}(0) & \delta &= w_{,x}(1)
\end{aligned}
$$

Assuming an element behaves as a beam-string, this function can provide the base for elemental shape functions. A shape functions set provides a mapping between the unknown nodal displacements and the predicted surface shape. Applying the boundary conditions in Table B.1 to Equation B.7 produces the following shape

B-3
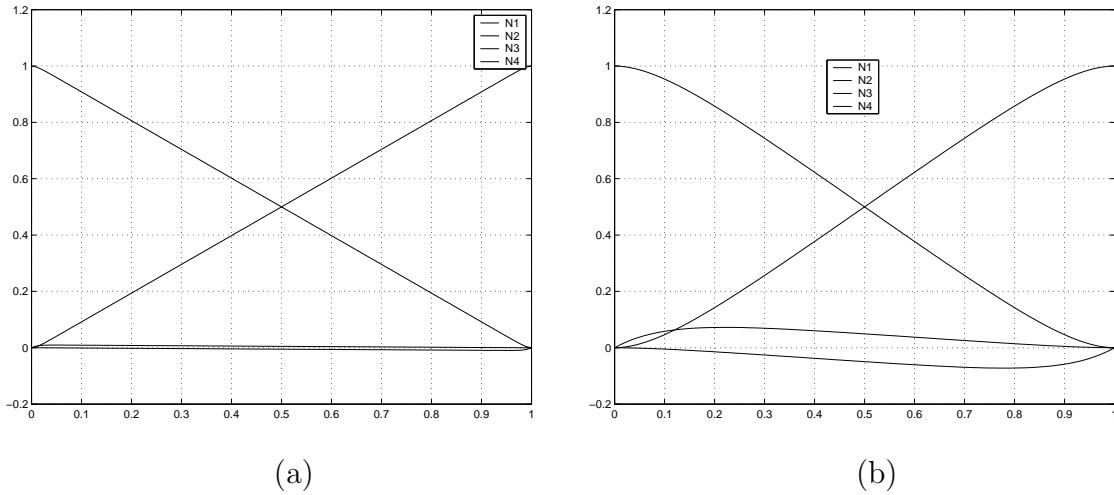
Figure B.1   Linear C^1 Shape Functions: (a) $\varepsilon = 0.01$ (b) $\varepsilon = 0.1$

function vector:

$$
N^T = \begin{pmatrix} N_1 \\ N_2 \\ N_3 \\ N_4 \end{pmatrix} = \begin{pmatrix} 1 - \eta \\ 0 \\ \eta \\ 0 \end{pmatrix} + \varepsilon \begin{pmatrix} 1 - 2\eta - \mathrm{e}^{-\xi} + \mathrm{e}^{-\zeta} \\ 1 - \eta - \mathrm{e}^{-\xi} \\ -1 + 2\eta + \mathrm{e}^{-\xi} - \mathrm{e}^{-\zeta} \\ -\eta + \mathrm{e}^{-\zeta} \end{pmatrix}
$$

$$
+ \varepsilon^2 \begin{pmatrix} 2 - 4\eta - 2\mathrm{e}^{-\xi} + 2\mathrm{e}^{-\zeta} \\ 1 - 2\eta - \mathrm{e}^{-\xi} + \mathrm{e}^{-\zeta} \\ -2 + 4\eta + 2\mathrm{e}^{-\xi} - 2\mathrm{e}^{-\zeta} \\ 1 - 2\eta - \mathrm{e}^{-\xi} + \mathrm{e}^{-\zeta} \end{pmatrix} \tag{B.9}
$$

$$
+ \varepsilon^3 \begin{pmatrix} 4 - 8\eta - 4\mathrm{e}^{-\xi} + 4\mathrm{e}^{-\zeta} \\ 2 - 4\eta - 2\mathrm{e}^{-\xi} + 2\mathrm{e}^{-\zeta} \\ -4 + 8\eta + 4\mathrm{e}^{-\xi} - 4\mathrm{e}^{-\zeta} \\ 2 - 4\eta - 2\mathrm{e}^{-\xi} + 2\mathrm{e}^{-\zeta} \end{pmatrix} + \cdots
$$

A plot of these shape functions (Figure B.1) illustrates the behavior of these functions. The shape functions plotted on the left and right are as a result of selecting ε values of 0.01 and 0.1, respectively. As ε approaches zero, N approaches

B-4

the standard string-type element. It should be clear, at this point, that while this element may be able to support nodal slopes, it is unable to model curvature away from its boundary.

B.2 Cubic C^1 Beam String Shape Functions

In an attempt to allow the element to more closely represent the true nature of the material, an internal node can be added, allowing for internal curvature. This introduces two additional degrees of freedom, which can be compensated for with two additional unknowns. This allows a cubic outer region.

Placing an internal node at the half way point, a simple beam-string of unit length with smallness parameter ε can be calculated much the same as in the previous section. The new boundary conditions; however, now must satisfy the internal node values with boundary conditions

$$
\begin{array}{ccc}
N(0) = \alpha & N(1) = \gamma & N(1/2) = \psi \\
\frac{dN}{dx}\big|_{x=0} = \beta & \frac{dN}{dx}\big|_{x=1} = \delta & \frac{dN}{dx}\big|_{x=1/2} = \phi.
\end{array}
\tag{B.10}
$$

The outer and inner solutions have the form

$$
\begin{aligned}
N^o(\eta) &= \sum_{i=0}^{n} \varepsilon^i \left[a_{i0} + a_{i1}\eta + a_{i2}\eta^2 + a_{i3}\eta^3 \right] \\
N^i(\xi) &= \sum_{i=0}^{n} \varepsilon^i \left[b_{i0} + b_{i1}\xi + b_{i2}\mathrm{e}^{-\xi} \right] \\
N^I(\zeta) &= \sum_{i=0}^{n} \varepsilon^i \left[c_{i0} + c_{i1}\zeta + c_{i2}\mathrm{e}^{-\zeta} \right]
\end{aligned}
\tag{B.11}
$$

B-5

with boundary conditions:

$$N_0(0) = \alpha \quad \frac{dN_0}{d\xi}|_{\xi=0} = 0 \quad N_0(1) = \gamma \quad \frac{dN_0}{d\zeta}|_{\zeta=0} = 0 \quad N_0(1/2) = \psi \quad \frac{dN_0}{d\eta}|_{\eta=1/2} = 0$$

$$N_1(0) = 0 \quad \frac{dN_1}{d\xi}|_{\xi=0} = \beta \quad N_1(1) = 0 \quad \frac{dN_1}{d\zeta}|_{\zeta=0} = -\delta \quad N_1(1/2) = 0 \quad \frac{dN_1}{d\eta}|_{\eta=1/2} = \phi$$

$$N_j(0) = 0 \quad \frac{dN_j}{d\xi}|_{\xi=0} = 0 \quad N_j(1) = 0 \quad \frac{dN_j}{d\zeta}|_{\zeta=0} = 0 \quad N_j(1/2) = 0 \quad \frac{dN_j}{d\eta}|_{\eta=1/2} = 0$$

$$(B.12)$$

for all $j > 1$, where $\eta = x$, $\xi = \frac{x}{\varepsilon}$ and $\zeta = \frac{1-x}{\varepsilon}$. Applying boundary conditions to the inner solutions, then matching to the outer solutions, of each order i in succession results in the following asymptotic beam-string solution

$$
\begin{aligned}
N(\eta,\xi,\zeta;\hat{\varepsilon}) = {} & \alpha + (\gamma - 5\alpha + 4\psi - 2\phi)\eta + (8\alpha - 4\gamma - 4\psi + 6\phi)\eta^2 + (4\gamma - 4\alpha - 4\phi)\eta^3 \\
& + \varepsilon[(5\alpha - \gamma + \beta - 4\psi + 2\phi) + (10\gamma - 26\alpha - 5\beta - \delta + 16\psi - 12\phi)\eta \\
& + (44\alpha - 28\gamma + 8\beta + 4\delta - 16\psi + 24\phi)\eta^2 + (24\gamma - 24\alpha - 4\beta - 4\delta - 16\phi)\eta^3 \\
& + (\gamma - 5\alpha - \beta + 4\psi - 2\phi)e^{-\xi} + (\alpha - 5\gamma + \delta + 4\psi + 2\phi)e^{-\zeta}] \\
& + \varepsilon^2[(26\alpha - 5\gamma + 5\beta + \delta - 16\psi + 12\phi) + (76\gamma - 140\alpha - 26\beta - 10\delta + 64\psi - 72\phi)\eta \\
& + (248\alpha - 184\gamma + 44\beta + 28\delta - 64\psi + 144\phi)\eta^2 + (144\gamma - 144\alpha - 24\beta - 24\delta - 96\phi)\eta^3 \\
& + (10\gamma - 26\alpha - 5\beta - \delta + 16\psi - 12\phi)e^{-\xi} + (10\alpha - 26\gamma + 5\delta + \beta + 16\psi + 12\phi)e^{-\zeta}] \\
& + \varepsilon^3[(140\alpha - 76\gamma + 26\beta + 10\delta - 64\psi + 72\phi) + (520\gamma - 776\alpha - 140\beta - 76\delta + 256\psi - 432\phi)\eta \\
& + (1424\alpha - 1168\gamma + 248\beta + 184\delta - 256\psi + 864\phi)\eta^2 + (864\gamma - 864\alpha - 144\beta - 144\delta - 576\phi)\eta^3 \\
& + (76\gamma - 140\alpha - 26\beta - 10\delta + 64\psi - 72\phi)e^{-\xi} + (76\alpha - 140\gamma + 26\delta + 10\beta + 64\psi + 72\phi)e^{-\zeta}] + \cdots
\end{aligned}
$$

$$(B.13)$$

where

$$\alpha = w(0) \quad \gamma = w(1) \quad \psi = w(1/2)$$

$$\beta = w_{,x}(0) \quad \delta = w_{,x}(1) \quad \phi = w_{,x}(1/2)$$

B-6

Shape Function	$w(0)$	$w_{,x}(0)$	$w(1)$	$w_{,x}(1)$	$w(1/2)$	$w_{,x}(1/2)$
Boundary Condition	α	β	γ	δ	ψ	ϕ
N_1	1	0	0	0	0	0
N_2	0	1	0	0	0	0
N_3	0	0	1	0	0	0
N_4	0	0	0	1	0	0
N_5	0	0	0	0	1	0
N_6	0	0	0	0	0	1

Table B.2   Cubic C^1 Shape Function Boundary Conditions

Applying the boundary conditions in Table B.2 to Equation B.13 produces the following shape function vector:

$$
N^T = \begin{pmatrix} N_1 \\ N_2 \\ N_3 \\ N_4 \\ N_5 \\ N_6 \end{pmatrix} = \begin{pmatrix} 1 - 5\eta + 8\eta^2 - 4\eta^3 \\ 0 \\ \eta - 4\eta^2 + 4\eta^3 \\ 0 \\ 4\eta - 4\eta^2 \\ -2\eta + 6\eta^2 - 4\eta^3 \end{pmatrix}
$$

$$
+ \varepsilon \begin{pmatrix} 5 - 26\eta + 44\eta^2 - 24\eta^3 - 5\mathrm{e}^{-\xi} + \mathrm{e}^{-\zeta} \\ 1 - 5\eta + 8\eta^2 - 4\eta^3 - \mathrm{e}^{-\xi} \\ -1 + 10\eta - 28\eta^2 + 24\eta^3 + \mathrm{e}^{-\xi} - 5\mathrm{e}^{-\zeta} \\ -\eta + 4\eta^2 - 4\eta^3 + \mathrm{e}^{-\zeta} \\ -4 + 16\eta - 16\eta^2 + 4\mathrm{e}^{-\xi} + 4\mathrm{e}^{-\zeta} \\ 2 - 12\eta + 24\eta^2 - 16\eta^3 - 2\mathrm{e}^{-\xi} + 2\mathrm{e}^{-\zeta} \end{pmatrix} \qquad (B.15)
$$

$$
+ \varepsilon^2 \begin{pmatrix} 26 - 140\eta + 248\eta^2 - 144\eta^3 - 26\mathrm{e}^{-\xi} + 10\mathrm{e}^{-\zeta} \\ 5 - 26\eta + 44\eta^2 - 24\eta^3 - 5\mathrm{e}^{-\xi} + \mathrm{e}^{-\zeta} \\ -10 + 76\eta - 184\eta^2 + 144\eta^3 + 10\mathrm{e}^{-\xi} - 26\mathrm{e}^{-\zeta} \\ 1 - 10\eta + 28\eta^2 - 24\eta^3 - \mathrm{e}^{-\xi} + 5\mathrm{e}^{-\zeta} \\ -16 + 64\eta - 64\eta^2 + 16\mathrm{e}^{-\xi} + 16\mathrm{e}^{-\zeta} \\ 12 - 72\eta + 144\eta^2 - 96\eta^3 - 12\mathrm{e}^{-\xi} + 12\mathrm{e}^{-\zeta} \end{pmatrix} + \cdots
$$
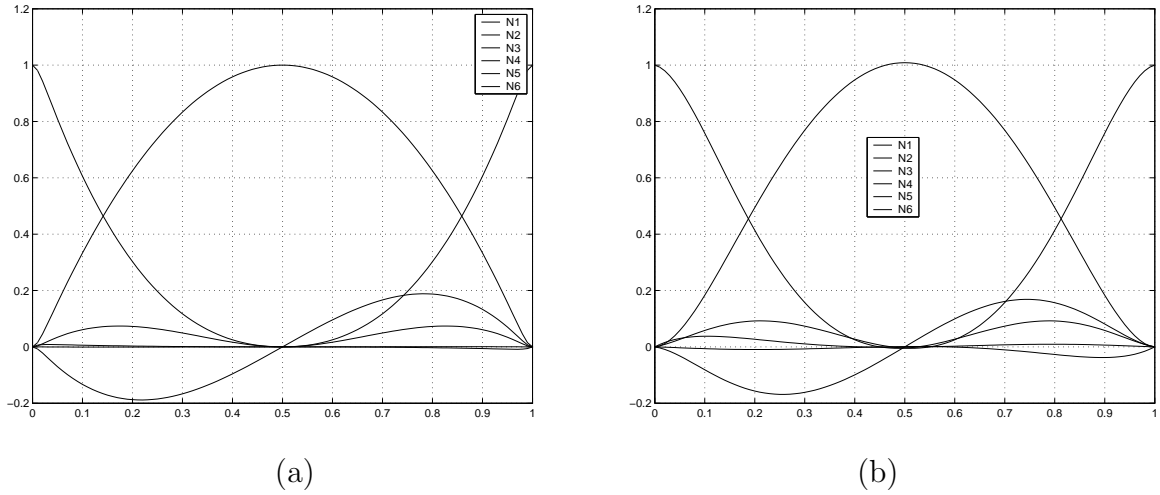
Figure B.2   Cubic C^1 Shape Functions: (a) $\varepsilon = 0.01$ (b) $\varepsilon = 0.1$

A plot of these shape functions (Figure B.2) illustrates the behavior of these functions. The shape functions plotted on the left and right are as a result of selecting ε values of 0.01 and 0.1, respectively. This element can support nodal slopes, and allows some curvature away from the boundary. It should also be noted that the shape functions themselves are expansions in orders of ε, which can be included early in a perturbation finite element development. These shape functions can be used for analysis where C^0 elements are not enough, but standard C^1 elements are too stiff.

B-8

Appendix C. Computer Routines

The computer routines are available on the comprehensive CD containing this document. Mathematica routines produce the Lagrangians, equations of motion, perturbation expansions and finite element matrix definitions. Many analytical solutions are produced using MathCAD worksheets.

Finite element routines were all implemented through MATLAB routines. The linear beam-string set of functions are provided here. The similar nonlinear functions are on the CD.

C.1 Linear Beam-String

C.1.1 Matlab Routines.

C.1.1.1 BS3FEM. BS3FEM is the main finite element routine. The user passes the elemental values as described in the header, and, depending on parameters, either a static or dynamic evaluation is performed. The routines called by BS3FEM follow.

```
function [vr,dr]=bs3fem(order, p, nodes, thick, dens, youngs, verbose, dyn, mode, mx)
% bs3fem - Finite Element simulation of beam-string
% written by : Capt James Rogers, USAF, AFIT
%
%   order   = order of perturbation levels terms to include (0 to 3)
%   p       = pressure differential per unit length applied to beam
%   nodes   = distance from left end of each element interface
%   thick   = thickness of beam
%   dens    = beam material density (mass/L^3)
%   youngs  = Material's Young's Modulus (F/L^2)
%   verbose = 0: No Plots Produced
%             1: All Plots Created
%   dyn     = 0: Static Only
%             1: Dynamic \/ \/ \/ \/
%   mode    = 0: Clamped Results Returned
%             1: Free Results Returned
%   mx      = maximum modes returned
%
%   vr      = Eigenvectors (Dynamic)
%             Analytic/Total Static FEM/
%             Only 1st Level FEM Solutions (Static)
%   dr      = Eigenvalues (Dynamic)
```

```
%               = Corresponding Axial Locations (Static)
%

num=length(nodes)-1;
len = nodes(length(nodes));

% Compute element values ans store in element structure
for i=1:num
    els(i).len  = nodes(i+1)-nodes(i);
    els(i).t    = dens*(els(i).len)^2/youngs;
    els(i).eps  = sqrt(((thick/(els(i).len))^2)/12);
    els(i).ps   = p*els(i).len/youngs/thick;
end

disp=3; %nodes per element
dpn=2;  %displacements per node

%Some presized matrices for use later
kg0=zeros(dpn*((disp-1)*num+1),dpn*((disp-1)*num+1));
mg0=zeros(dpn*((disp-1)*num+1),dpn*((disp-1)*num+1));
pg0=zeros(dpn*((disp-1)*num+1),1);
w0=zeros(dpn*((disp-1)*num+1),1);

if order > 0
    kg1=zeros(dpn*((disp-1)*num+1),dpn*((disp-1)*num+1));
    mg1=zeros(dpn*((disp-1)*num+1),dpn*((disp-1)*num+1));
    pg1=zeros(dpn*((disp-1)*num+1),1);
    w1=zeros(dpn*((disp-1)*num+1),1);
    if order > 1
        kg2=zeros(dpn*((disp-1)*num+1),dpn*((disp-1)*num+1));
        mg2=zeros(dpn*((disp-1)*num+1),dpn*((disp-1)*num+1));
        pg2=zeros(dpn*((disp-1)*num+1),1);
        w2=zeros(dpn*((disp-1)*num+1),1);
    end
end

chunk=100;
ds=zeros(chunk*num+1,order+1);
x=zeros(chunk*num+1,1);
ws=zeros(chunk*num+1,order+2);
if order > 0
    we=zeros(chunk*num+1,order);
end

%Build System Matrices
for i=1:num
    nodeids=[(disp-1)*i-(disp-2), (disp-1)*i+(disp-2), (disp-1)*i];
    kg0=BuildStiffness(kg0,K0b(els(i).eps,els(i).len),nodeids);
    mg0=BuildMass(mg0,M0b(els(i).eps,els(i).len),nodeids);
    pg0=BuildForce(pg0,els(i).ps*P0b(els(i).eps,els(i).len),nodeids);
    if order > 0
        kg1=BuildStiffness(kg1,els(i).eps*K1b(els(i).eps,els(i).len),nodeids);
        mg1=BuildMass(mg1,els(i).eps*M1b(els(i).eps,els(i).len),nodeids);
        pg1=BuildForce(pg1,els(i).ps*els(i).eps*P1b(els(i).eps,els(i).len),nodeids);
        if order > 1
            kg2=BuildStiffness(kg2,els(i).eps^2*K2b(els(i).eps,els(i).len),nodeids);
            mg2=BuildMass(mg2,els(i).eps^2*M2b(els(i).eps,els(i).len),nodeids);
            pg2=BuildForce(pg2,els(i).ps*els(i).eps^2*P2b(els(i).eps,els(i).len),nodeids);
        end
    end
end

%Clamped-Clamped System Matrices
m0c=mg0(dpn+1:dpn*(disp-1)*num,dpn+1:dpn*(disp-1)*num);
k0c=kg0(dpn+1:dpn*(disp-1)*num,dpn+1:dpn*(disp-1)*num);
```

C-2

```matlab
if order > 0
    m1c=mg1(dpn+1:dpn*(disp-1)*num,dpn+1:dpn*(disp-1)*num);
    k1c=kg1(dpn+1:dpn*(disp-1)*num,dpn+1:dpn*(disp-1)*num);
    if order > 1
        m2c=mg2(dpn+1:dpn*(disp-1)*num,dpn+1:dpn*(disp-1)*num);
        k2c=kg2(dpn+1:dpn*(disp-1)*num,dpn+1:dpn*(disp-1)*num);
    end
end

%Static solution
w0(dpn+1:dpn*(disp-1)*num)=k0c\pg0(dpn+1:dpn*(disp-1)*num);
if order > 0
    w1(dpn+1:dpn*(disp-1)*num)=-k0c\(k1c*w0(dpn+1:dpn*(disp-1)*num)+...
        pg1(dpn+1:dpn*(disp-1)*num));
    if order > 1
        w2(dpn+1:dpn*(disp-1)*num)=-k0c\(k1c*w1(dpn+1:dpn*(disp-1)*num)+...
            k2c*w0(dpn+1:dpn*(disp-1)*num)+pg2(dpn+1:dpn*(disp-1)*num));
    end
end
start=0;
for i=1:num
    nodeids=[(disp-1)*i-(disp-2), (disp-1)*i+(disp-2), (disp-1)*i];
    d0=GetDisplacements(w0,dpn,nodeids);
    if order > 0
        d1=GetDisplacements(w1,dpn,nodeids);
        if order > 1
            d2=GetDisplacements(w2,dpn,nodeids);
        end
    end
    for j=0:chunk
        ws((i-1)*chunk+j+1,2)=bs3shape(d0,(j/chunk),els(i).eps);
        if order > 0
            ws((i-1)*chunk+j+1,3)=bs3shape(d0+d1,(j/chunk),els(i).eps);
            if order > 1
                ws((i-1)*chunk+j+1,4)=bs3shape(d0+d1+d2,(j/chunk),els(i).eps);
            end
        end
        x((i-1)*chunk+j+1)=start + (j/chunk)*els(i).len;
    end
    start=start+els(i).len;
end

%Analytic Solution
eps=sqrt(((thick/len)^2)/12);
pa=p*len/youngs/thick;

for i=1:chunk*num+1
    xl=x(i)/len;
    ws(i,1)=len*(pa/2)*((xl-xl^2) - eps*(1-exp(-xl/eps)-exp((xl-1)/eps)));
    if order > 0
        we(i,1)=ws(i,1)-ws(i,2);
        if order > 1
            we(i,2)=we(i,1)-ws(i,3);
        end
    end
end

if dyn == 0 %Static Requested
    if verbose > 0
        figure
        plot(x,ws);
        title('Static Shape');
        if order == 0
            legend('Analytical','w0');
        elseif order == 1
```

```matlab
            legend('Analytical','w0', 'w0 + w1');
        elseif order == 2
            legend('Analytical','w0', 'w0 + w1', 'w0 + w1 + w2');
        end

        figure
        plot(x,ws(:,1),'-.',x, ws(:,order+2),'-');
        title('Static Shape');
        legend('Analytical Solution','FEM Solution');

        figure
        plot(x,ws(:,1)-ws(:,order+2));
        title('Static Shape Error');

        if order > 0
            figure
            plot(x,we);
            title('Shape Errors');
            if order == 1
                legend('W1 Correction');
            elseif order == 2
                legend('W1 Correction','W2 Correction');
            end
        end
    end

    dr = x;
    vr = ws;
    return
else  %Dynamic Requested

    % Presized Matrices
    v0=zeros(dpn*((disp-1)*num+1),dpn*((disp-1)*num+1));
    d0=zeros(dpn*((disp-1)*num+1),dpn*((disp-1)*num+1));
    if order > 0
        v1=zeros(dpn*((disp-1)*num+1),dpn*((disp-1)*num+1));
        d1=zeros(dpn*((disp-1)*num+1),dpn*((disp-1)*num+1));
        if order > 1
            v2=zeros(dpn*((disp-1)*num+1),dpn*((disp-1)*num+1));
            d2=zeros(dpn*((disp-1)*num+1),dpn*((disp-1)*num+1));
        end
    end

    if mode == 0 %Clamped Mode Requested

        % Compute Eigenvectors/Values of 0th order system
        [v0(dpn+1:dpn*(disp-1)*num,dpn+1:dpn*(disp-1)*num),...
                d0(dpn+1:dpn*(disp-1)*num,dpn+1:dpn*(disp-1)*num)]=eig(k0c,m0c);
        [vc0,dc0]=sorteigs(v0,d0,0,mx);
        omega=sqrt(dc0);
        if order>0
            %Get 1st Order Correction
            for i=1:mx
                omega1(i)=(vc0(:,i)'*(kg1-dc0(i)*mg1)*vc0(:,i));
                if omega1(i) ~= 0
                    omega1(i)=omega1(i)/(2*dc0(i)*vc0(:,i)'*mg0*vc0(:,i));
                    omega(i)=omega(i)+omega1(i);
                end
            end
            if order>1
                %Get Second Order Correction
                for i=1:mx
                    omega2(i)=(vc0(:,i)'*(kg2-dc0(i)*(omega1(i)^2*mg0+2*omega1(i)*mg1+mg2))*vc0(:,i));
                    if omega2(i) ~= 0
                        omega2(i)=omega2(i)/(2*dc0(i)*vc0(:,i)'*mg0*vc0(:,i));
```

C-4

```
                omega(i)=omega(i)+omega2(i);
            end
        end
    end
end

if verbose>0
 if length(dc0)>0
        figure;
        plot3shape(vc0,dpn,els);
        title('Clamped V0 Modes');
    figure;
    bar(dc0);
        title('Clamped D0 - Eigenvalues');
 end

    if order > 0
        figure;
        bar(omega1)
        title('1st Order Frequency Corrections');

        if order > 1
            figure;
            bar(omega2)
            title('2nd Order Frequency Corrections');
        end
    end
    figure
    bar(omega/omega(1));
        title('Normalized Frequencies: \omega/\omega_0');
end
vr = vc0;
dr = omega;
elseif mode == 1

    %Free-Free
    [v0,d0]=eig(kg0,mg0);
    [vf0,df0]=sorteigs(v0,d0,1,mx);
    omega=sqrt(df0);
    if order > 0
        for i=1:mx
            omega1(i)=(vf0(:,i)'*(kg1-df0(i)*mg1)*vf0(:,i));
            if omega1(i) ~= 0
                omega1(i)=omega1(i)/(2*df0(i)*vf0(:,i)'*mg0*vf0(:,i));
                omega(i)=omega(i)+omega1(i);
            end
        end
        if order>1
            for i=1:mx
                omega2(i)=(vf0(:,i)'*(kg2-df0(i)*(omega1(i)^2*mg0+2*omega1(i)*mg1+mg2))*vf0(:,i));
                if omega2(i) ~= 0
                    omega2(i)=omega2(i)/(2*df0(i)*vf0(:,i)'*mg0*vf0(:,i));
                    omega(i)=omega(i)+omega2(i);
                end
            end
        end
    end

    if verbose>0
        if order > 0
          if length(df0)>0
                figure;
                plot3shape(vf0,dpn,els);
                title('Free V0 Modes');
             figure;
```

C-5

```
                bar(df0);
                title('Free D0 - Eigenvalues');
            end

              figure;
               bar(omega1)
               title('1st Order Frequency Corrections');

               if order > 1
                   figure;
                   bar(omega2)
                   title('2nd Order Frequency Corrections');

               end
           end
           figure
           bar(real(omega/omega(1)));
           title('Normailized Frequencies: \omega/\omega_0');
       end
       vr = vf0;
       dr = omega;
    end
end
```

C.1.1.2 BUILDSTIFFNESS. BUILDSTIFFNESS packages the elemental stiffness matrix into the global matrix depending on the node identities included.

```
function [kg]=BuildStiffness(kg, ke, nodelist)
% Build Stiffness -- Add element stiffness to global stiffness
%   kg = global stiffness matrix
%   ke = element stiffness matrix
%   nodelist = vector of node ids used to place elemental values in kg

% disp represents the number of displacement variables per node
disp=max(size(ke))/max(size(nodelist));

for i=1:max(size(nodelist))
    for j=1:max(size(nodelist))
        kg((nodelist(i)-1)*disp+1:nodelist(i)*disp,(nodelist(j)-1)*disp+1:nodelist(j)*disp)=...
            kg((nodelist(i)-1)*disp+1:nodelist(i)*disp,(nodelist(j)-1)*disp+1:nodelist(j)*disp)+...
            ke((i-1)*disp+1:i*disp,(j-1)*disp+1:j*disp);
    end
end
```

C.1.1.3 BUILDMASS. BUILDMASS packages the elemental mass matrix into the global matrix depending on the node identities included.

```
function [mg]=BuildMass(mg, me, nodelist)
% Build Mass -- Add element mass to global mass
%   mg = global mass matrix
%   me = element mass matrix
%   nodelist = vector of node ids used to place elemental values in mg

% disp represents the number of displacement variables per node
disp=max(size(me))/max(size(nodelist));

for i=1:max(size(nodelist))
    for j=1:max(size(nodelist))
        mg((nodelist(i)-1)*disp+1:nodelist(i)*disp,(nodelist(j)-1)*disp+1:nodelist(j)*disp)=...
```

C-6

```
        mg((nodelist(i)-1)*disp+1:nodelist(i)*disp,(nodelist(j)-1)*disp+1:nodelist(j)*disp)+...
        me((i-1)*disp+1:i*disp,(j-1)*disp+1:j*disp);
    end
end
```

C.1.1.4 BUILDFORCE. BUILDFORCE packages the elemental forcing matrix into the global matrix depending on the node identities included.

```
function [fg]=BuildForce(fg, fe, nodelist)
% Build Force -- Add element force to global force
%   fg = global force vector
%   fe = element force vector
%   nodelist = vector of node ids used to place elemental values in fg

% disp represents the number of displacement variables per node
disp=max(size(fe))/max(size(nodelist));

for i=1:max(size(nodelist))
    fg((nodelist(i)-1)*disp+1:nodelist(i)*disp)=...
        fg((nodelist(i)-1)*disp+1:nodelist(i)*disp)+fe((i-1)*disp+1:i*disp);
end
```

C.1.1.5 SORTEIGS. SORTEIGS is just a small routine which organizes the provided eigensystem depending on the caller's request.

```
function [vo,do]=sorteigs(vi,di,zer,mx)
% SortEigs returns ordered eigensystem requested
%
% vi    :   eigenvectors
% di    :   eigenvalues
%
% zer   :   0 include only positive definite results
%           1 include positive semi-definite results
%          -1 include all
%
% mx    :   Maximun requested
%
if nargin ~= 4
    mx = length(di);
end
eigs=diag(di);
cnt=0;
tot=0;
do=[];
vo=[];
if zer >= 0
    %count total positives
    for i=1:length(eigs)
      if isreal(eigs(i))
          if zer==0
              if eigs(i)>0
                  tot=tot+1;
              end
          else
              if eigs(i)>=0
                  tot=tot+1;
              end
          end
      end
    end
```

C-7

```
else
    tot=length(eigs);
end
if tot > 0
d=zeros(tot,1);
    v=zeros(max(size(vi)),tot);

    if zer>=0
     %find valid eigenstructure
        for i=1:length(eigs)
            if isreal(eigs(i))
                if zer == 0
                 if eigs(i)>0
                   cnt=cnt+1;
                    v(:,cnt)=vi(:,i);
                        d(cnt)=eigs(i);
                    end
                else
                if eigs(i)>=0
                        cnt=cnt+1;
                        v(:,cnt)=vi(:,i);
                        d(cnt)=eigs(i);
                    end
                end
            end
         end
        end
    else
        d=eigs;
        v=vi;
        cnt=tot;
    end

   %order from smallest eigenvalue to largest
for i=1:cnt-1
   for j=1:cnt-i
      if d(j)>d(j+1)
         tmp=d(j);
         d(j)=d(j+1);
         d(j+1)=tmp;
         tv=v(:,j);
         v(:,j)=v(:,j+1);
         v(:,j+1)=tv;
      end
   end
end
    if zer < 0
   vo=v;
       do=d;
   else
     if cnt>mx
        vo=v(:,1:mx);
            do=d(1:mx);
       else
        vo=v;
            do=d;
     end
    end
end
```

C.1.2   Element Matrices.

C.1.2.1   K0b.   K0b computes the 0th order elemental stiffness matrix.

```
function [K]=K0b(eps,L)
K=[(L*(47 + 30*eps*(-6 + 13*L)))/15 ...
   eps*L*(-1 + 5*L) ...
   -(L*(7 + 30*eps*(-6 + 5*L)))/15 ...
   eps*(-1 + L)*L ...
(-8*L*(1 + 6*eps*L))/3 ...
   (4*L*(1 + 5*eps*(-1 + 3*L)))/5; ...

eps*L*(-1 + 5*L) ...
   eps*L^2 ...
   -(eps*(-1 + L)*L) ...
   0 ...
   -4*eps*L^2 ...
   2*eps*L^2; ...

-(L*(7 + 30*eps*(-6 + 5*L)))/15 ...
   -(eps*(-1 + L)*L) ...
   (L*(47 + 30*eps*(-6 + 13*L)))/15 ...
   eps*(1 - 5*L)*L ...
   (-8*L*(1 + 6*eps*L))/3 ...
   (-4*L*(1 + 5*eps*(-1 + 3*L)))/5; ...

eps*(-1 + L)*L ...
   0 ...
   eps*(1 - 5*L)*L ...
   eps*L^2 ...
   4*eps*L^2 ...
   2*eps*L^2; ...

(-8*L*(1 + 6*eps*L))/3 ...
   -4*eps*L^2 ...
   (-8*L*(1 + 6*eps*L))/3 ...
   4*eps*L^2 ...
   (16*L*(1 + 6*eps*L))/3 ...
   0; ...

   (4*L*(1 + 5*eps*(-1 + 3*L)))/5 ...
   2*eps*L^2 ...
   (-4*L*(1 + 5*eps*(-1 + 3*L)))/5 ...
   2*eps*L^2 ...
   0 ...
   (4*L*(1 + 10*eps*L))/5];
```

C.1.2.2   K1b.   K1b computes the 1st order elemental stiffness matrix.

```
function [K]=K1b(eps,L)
K=[-32*eps + (484/15 - 144*eps)*L + 280*eps*L^2 ...
   -4*eps + (47/15 - 18*eps)*L + 52*eps*L^2 ...
   -32*eps + (-164/15 + 144*eps)*L - 152*eps*L^2 ...
   4*eps + (7/15 - 18*eps)*L + 20*eps*L^2 ...
   (-64*(-3*eps + L + 6*eps*L^2))/3 ...
   12*L*(1 + 6*eps*(-1 + 2*L)); ...

-4*eps + (47/15 - 18*eps)*L + 52*eps*L^2 ...
   2*eps*L*(-1 + 5*L) ...
   -4*eps + (-7/15 + 18*eps)*L - 20*eps*L^2 ...
   2*eps*(-1 + L)*L ...
```

C-9

```
      (-8*(-3*eps + L + 12*eps*L^2))/3 ...
      (4*L*(1 + 10*eps*(-1 + 3*L)))/5; ...

    -32*eps + (-164/15 + 144*eps)*L - 152*eps*L^2 ...
     -4*eps + (-7/15 + 18*eps)*L - 20*eps*L^2 ...
    -32*eps + (484/15 - 144*eps)*L + 280*eps*L^2 ...
     4*eps + (-47/15 + 18*eps)*L - 52*eps*L^2 ...
 (-64*(-3*eps + L + 6*eps*L^2))/3 ...
     -12*L*(1 + 6*eps*(-1 + 2*L)); ...

 4*eps + (7/15 - 18*eps)*L + 20*eps*L^2 ...
    2*eps*(-1 + L)*L ...
    4*eps + (-47/15 + 18*eps)*L - 52*eps*L^2 ...
    2*eps*L*(-1 + 5*L) ...
    (8*(-3*eps + L + 12*eps*L^2))/3 ...
    (4*L*(1 + 10*eps*(-1 + 3*L)))/5; ...

 (-64*(-3*eps + L + 6*eps*L^2))/3 ...
    (-8*(-3*eps + L + 12*eps*L^2))/3 ...
    (-64*(-3*eps + L + 6*eps*L^2))/3 ...
    (8*(-3*eps + L + 12*eps*L^2))/3 ...
    (128*(-3*eps + L + 6*eps*L^2))/3 ...
    0; ...

 12*L*(1 + 6*eps*(-1 + 2*L)) ...
    (4*L*(1 + 10*eps*(-1 + 3*L)))/5 ...
    -12*L*(1 + 6*eps*(-1 + 2*L)) ...
    (4*L*(1 + 10*eps*(-1 + 3*L)))/5 ...
    0 ...
    (32*L*(1 + 5*eps*(-1 + 3*L)))/5];
```

C.1.2.3   K2b.   K2b computes the 2nd order elemental stiffness matrix.

```
function [K]=K2b(eps,L)
K=[-256*eps + 64/L + (1292/5 - 1296*eps)*L + 2328*eps*L^2 ...
    -48*eps + (484/15 - 180*eps)*L + 420*eps*L^2 ...
    -256*eps - 32/L + (4*(-163 + 1620*eps)*L)/5 - 1560*eps*L^2 ...
    48*eps + (164/15 - 180*eps)*L + 228*eps*L^2 ...
    (-32*(1 - 16*eps*L + 4*L^2 + 24*eps*L^3))/L ...
    (48*(5 - 3*(-4 + 25*eps)*L^2 + 135*eps*L^3))/(5*L); ...

 -48*eps + (484/15 - 180*eps)*L + 420*eps*L^2 ...
    -8*eps + (47/15 - 24*eps)*L + 78*eps*L^2 ...
    -48*eps + (-164/15 + 180*eps)*L - 228*eps*L^2 ...
    8*eps + (7/15 - 24*eps)*L + 30*eps*L^2 ...
    (-32*(-9*eps + 2*L + 18*eps*L^2))/3 ...
    12*L*(1 + 2*eps*(-4 + 9*L)); ...

 -256*eps - 32/L + (4*(-163 + 1620*eps)*L)/5 - 1560*eps*L^2 ...
    -48*eps + (-164/15 + 180*eps)*L - 228*eps*L^2 ...
    -256*eps + 64/L + (1292/5 - 1296*eps)*L + 2328*eps*L^2 ...
    48*eps + (-484/15 + 180*eps)*L - 420*eps*L^2 ...
    (-32*(1 - 16*eps*L + 4*L^2 + 24*eps*L^3))/L ...
    (-48*(5 - 3*(-4 + 25*eps)*L^2 + 135*eps*L^3))/(5*L); ...

  48*eps + (164/15 - 180*eps)*L + 228*eps*L^2 ...
   8*eps + (7/15 - 24*eps)*L + 30*eps*L^2 ...
   48*eps + (-484/15 + 180*eps)*L - 420*eps*L^2 ...
   -8*eps + (47/15 - 24*eps)*L + 78*eps*L^2 ...
 (32*(-9*eps + 2*L + 18*eps*L^2))/3 ...
    12*L*(1 + 2*eps*(-4 + 9*L)); ...
```

C-10

```
    (-32*(1 - 16*eps*L + 4*L^2 + 24*eps*L^3))/L ...
    (-32*(-9*eps + 2*L + 18*eps*L^2))/3 ...
    (-32*(1 - 16*eps*L + 4*L^2 + 24*eps*L^3))/L ...
    (32*(-9*eps + 2*L + 18*eps*L^2))/3 ...
    (64*(1 - 16*eps*L + 4*L^2 + 24*eps*L^3))/L ...
    0; ...

(48*(5 - 3*(-4 + 25*eps)*L^2 + 135*eps*L^3))/(5*L) ...
    12*L*(1 + 2*eps*(-4 + 9*L)) ...
    (-48*(5 - 3*(-4 + 25*eps)*L^2 + 135*eps*L^3))/(5*L) ...
    12*L*(1 + 2*eps*(-4 + 9*L)) ...
    0 ...
    (48*(5 + (7 - 40*eps)*L^2 + 90*eps*L^3))/(5*L)];
```

C.1.2.4   M0b.   M0b computes the 0th order elemental mass matrix.

```
function [M]=M0b(eps,L)
M=[(3*L^3)/35 0 L^3/70 0 L^3/15 -L^3/70;
   0 0 0 0 0 0;
   L^3/70 0 (3*L^3)/35 0 L^3/15 L^3/70;
   0 0 0 0 0 0;
   L^3/15 0 L^3/15 0 (8*L^3)/15 0;
   -L^3/70 0 L^3/70 0 0 (2*L^3)/105];
```

C.1.2.5   M1b.   M1b computes the 1st order elemental mass matrix.

```
function [M]=M1b(eps,L)
M=[(-4*eps*L^2)/3 + (29*L^3)/35 ...
   -(eps*L^2)/6 + (3*L^3)/35 ...
   -(L^2*(140*eps + 3*L))/105 ...
   ((35*eps - 3*L)*L^2)/210 ...
   (-2*L^2*(10*eps + L))/15 ...
   (2*L^3)/35; ...

-(eps*L^2)/6 + (3*L^3)/35 ...
   0 ...
   (L^2*(-35*eps + 3*L))/210 ...
   0 ...
   (L^2*(-10*eps + L))/15 ...
   -L^3/70; ...

-(L^2*(140*eps + 3*L))/105 ...
   (L^2*(-35*eps + 3*L))/210 ...
   (-4*eps*L^2)/3 + (29*L^3)/35 ...
   (eps*L^2)/6 - (3*L^3)/35 ...
   (-2*L^2*(10*eps + L))/15 ...
   (-2*L^3)/35; ...

((35*eps - 3*L)*L^2)/210 ...
   0 ...
   (eps*L^2)/6 - (3*L^3)/35 ...
   0 ...
   -(L^2*(-10*eps + L))/15 ...
   -L^3/70; ...

(-2*L^2*(10*eps + L))/15 ...
   (L^2*(-10*eps + L))/15 ...
   (-2*L^2*(10*eps + L))/15 ...
   -(L^2*(-10*eps + L))/15 ...
   (-16*L^2*(-10*eps + L))/15 ...
   0; ...
```

C-11

```
(2*L^3)/35 ...
  -L^3/70 ...
  (-2*L^3)/35 ...
  -L^3/70 ...
  0 ...
  (-4*L^3)/35];
```

C.1.2.6   M2b.   M2b computes the 2nd order elemental mass matrix.

```
function [M]=M2b(eps,L)
M=[-10*eps^2*L + (7*eps*L^2)/3 + (219*L^3)/35 ...
   -(eps^2*L) + (eps*L^2)/2 + (29*L^3)/35 ...
   26*eps^2*L - (47*eps*L^2)/3 - (51*L^3)/35 ...
   -5*eps^2*L + (5*eps*L^2)/2 + L^3/35 ...
   (-8*L*(30*eps^2 + 5*eps*L + 4*L^2))/15 ...
   (6*L*(-10*eps^2 + 5*eps*L + L^2))/5; ...

-(eps^2*L) + (eps*L^2)/2 + (29*L^3)/35 ...
   (eps*L^2)/6 + (3*L^3)/35 ...
   5*eps^2*L - (5*eps*L^2)/2 - L^3/35 ...
   -(eps^2*L) + (eps*L^2)/3 - L^3/70 ...
   (-2*L*(30*eps^2 + 15*eps*L + L^2))/15 ...
-2*eps^2*L + eps*L^2 + (2*L^3)/35; ...

   26*eps^2*L - (47*eps*L^2)/3 - (51*L^3)/35 ...
   5*eps^2*L - (5*eps*L^2)/2 - L^3/35 ...
   -10*eps^2*L + (7*eps*L^2)/3 + (219*L^3)/35 ...
   eps^2*L - (eps*L^2)/2 - (29*L^3)/35 ...
   (-8*L*(30*eps^2 + 5*eps*L + 4*L^2))/15 ...
(-6*L*(-10*eps^2 + 5*eps*L + L^2))/5; ...

   -5*eps^2*L + (5*eps*L^2)/2 + L^3/35 ...
   -(eps^2*L) + (eps*L^2)/3 - L^3/70 ...
   eps^2*L - (eps*L^2)/2 - (29*L^3)/35 ...
   (eps*L^2)/6 + (3*L^3)/35 ...
   (2*L*(30*eps^2 + 15*eps*L + L^2))/15 ...
-2*eps^2*L + eps*L^2 + (2*L^3)/35; ...

   (-8*L*(30*eps^2 + 5*eps*L + 4*L^2))/15 ...
   (-2*L*(30*eps^2 + 15*eps*L + L^2))/15 ...
   (-8*L*(30*eps^2 + 5*eps*L + 4*L^2))/15 ...
   (2*L*(30*eps^2 + 15*eps*L + L^2))/15 ...
   (-16*L*(-30*eps^2 - 35*eps*L + L^2))/15 ...
   0; ...

   (6*L*(-10*eps^2 + 5*eps*L + L^2))/5 ...
   -2*eps^2*L + eps*L^2 + (2*L^3)/35 ...
   (-6*L*(-10*eps^2 + 5*eps*L + L^2))/5 ...
   -2*eps^2*L + eps*L^2 + (2*L^3)/35 ...
0 ...
   (-4*L*(70*eps^2 - 35*eps*L + L^2))/35];
```

C.1.2.7   P0b.   P0b computes the 0th order elemental forcing matrix.

```
function [P]=P0b(eps,L)
   P=[L^3/6; 0; L^3/6; 0; (2*L^3)/3; 0];
```

C-12

C.1.2.8 P1b.
P1b computes the 1st order elemental forcing matrix.

```
function [P]=P1b(eps,L)
   P=[(2*L^2*(-6*eps + L))/3; (L^2*(-6*eps + L))/6; (2*L^2*(-6*eps + L))/3;
      -(L^2*(-6*eps + L))/6; (-4*L^2*(-6*eps + L))/3; 0];
```

C.1.2.9 P2b.
P2b computes the 2nd order elemental forcing matrix.

```
function [P]=P2b(eps,L)
   P=[(8*L^2*(-6*eps + L))/3; (2*L^2*(-6*eps + L))/3;
      (8*L^2*(-6*eps + L))/3; (-2*L^2*(-6*eps + L))/3;
      (-16*L^2*(-6*eps + L))/3; 0];
```

Bibliography

1. Fang, H. and Lou, M.C. *Analytical Characterization of Space Inflatable Structures - An Overview*. Technical Report AIAA 99-1272, AIAA, 1999.

2. Freeland, R.E., Bilyeu, G.D., Veal, G.R. and Mikulas, M.M. "Inflatable Deployable Space Structures Technology Summary," *IAF Paper 98-I.5.01, 49th International Astronautical Congress, Melbourne, Australia* September 28 - October 2 1998.

3. Palisoc, A., Veal, G., Cassapakis, C., Greschik, G. and Mikulas, M.M. "Geometry Attained by Pressurized Membranes," *Space Telescopes and Instruments V, Kona Hawaii, SPIE 3356*:747–757 March 25-28 1998.

4. Cassapakis, C. and Thomas, M. "Inflatable Structures Technology Development Overview," *AIAA Paper 95-3738, AIAA 1995 Space Programs and Technologies Conference, Huntsville, Alabama* September 26-28 1995.

5. Freeland, R.E. and Veal, G.R. "Significance of the Inflatable Antenna Experiment Technology," *AIAA Paper 98-2104* 1998.

6. Beauchamp, P.M. and Rodgers, D.H. "New Concepts for Inflatable Structures Applied to Spaceborne Radars," *AIAA Paper 95-3795* 1995.

7. Inc., L'Garde, "www.lgarde.com," September 28 1999.

8. Satter, C.M. and Freeland, R.E. "Inflatable Structures Technology Applications and Requirements," *AIAA Paper 95-3737, AIAA 1995 Space Programs and Technologies Conference, Huntsville, Alabama* September 26-28 1995.

9. NASA, "ngst.gsfc.nasa.gov," September 28 1999.

10. Technologies, SRS, "stg.srs.com," September 28 1999.

11. NASA, "arise.jpl.nasa.gov," September 28 1999.

12. Ulvestad, J.S., Linfield, R.P. and Smith, J.G. "ARISE: A Space VLBI Mission Using and Inflatable Antenna Structure," *AIAA Paper 95-3794, AIAA 1995 Space Programs and Technologies Conference, Huntsville, Alabama* September 26-28 1995.

13. Engberg, R. and Lassiter, J. "Dynamic Testing of Inflatable Structures," *Journal of Sound and Vibration* June 1999.

14. Dover, ILC, "www.ilcdover.com," September 28 1999.

15. Sewall, J.L., Miserentino, R. and Pappa, R.S. *Vibration Studies of a Lightweight Three-Sided Membrane Suitable for Space Application*. Technical Paper 2095, NASA, 1983.

16. Greschik, G., Palisoc, A., Cassapakis, C., Veal, G. and Mikulas, M.M. "Approximating Paraboloids with Axisymmetric Pressurized Membranes," *AIAA 39th Structures, Structural Dynamics, and Materials Conference and Adaptive Structures Forum*, *AIAA 98-2102*:2772–2782 April 20-23 1998.

17. Wagner, J.W. *Optical Metrology of Adaptive Membrane Mirrors*. MS thesis, Air Force Institute of Technology, March 2000.

18. Rotgé, J.R., Marker, D.K., Carreras, R.A., Wiles, J.M. and Duneman, D. *Large Optically Flat Membrane Mirrors*. Final Report AFRL-DE-99-463, AFRL, July 1999. AFRL/DE.

19. May, C.A. and Jr., A. Wereta. *Process Identification Study for Space Cured Composite Structures*. NASA Contract Report 158942, NASA, September 1978.

20. Carreras, R.A., Marker, D.K., Rotgé, J.R., Wilkes, J.M. and Duneman, D. *Deployable Near-Net Shape Membrane Optics*. Final Report AFRL-DE-99-463, AFRL, July 1999. AFRL/DE.

21. Marker, D.K., Rotgé, J.R., Carreras, R.A., Duneman, D. and Wilkes, J.M. *Minimum Strain Requirements for Optical Membranes*. Final Report AFRL-DE-99-463, AFRL, July 1999. AFRL/DE.

22. Gierow, P.A., Paxton, J.P., Cost, T.L. and Hawk, C.W. "Material-Property Effects on a Thin-Film Solar Concentrator," *Journal of Spacecraft and Rockets*, *32*(4):697–702 July 1995.

23. Main, J.A., Carlin, R.A., Garcia, E., Peterson, S.W. and Strauss, A.M. "Dynamic Analysis of Space-Based Inflated Beam Structures," *Journal of the Acoustic Society of America*, *97*(2):1035–1045 February 1995.

24. Gruneisen, M.T., Wick, D.V., Martinez, T. and Wilkes, J.M. *Correction of Large Dynamic Aberrations by Real-Time Holography using Electro-Optical Devices and Nonlinear Optical Media*. Final Report AFRL-DE-99-463, AFRL, July 1999. AFRL/DE.

25. Wick, D.V., Martinez, T., Wood, M.V., Wilkes, J.M., Gruneisen, M.T., Berenberg, V.A., Vasil'ev, M.V., Onokhov, A.P. and Beresnev, L.A. *Deformed-Helix Ferroelectric Liquid-Crystal Spatial Light Modulator Demonstrating High Diffraction Efficiency and 370 Line Pairs Per Millimeter Resolution*. Final Report AFRL-DE-99-463, AFRL, July 1999. AFRL/DE.

26. Bailey, T., Gruzen, A. and Madden, P. *RCS/Piezoelectric Distributed Actuator Study*. Final Report AFAL-TR-88-038, AFAL, August 1988.

27. Sato, T., Ishida, H. and Ikeda, O. "Adaptive PVDF Piezoelectric Deformable Mirror System," *Applied Optics*, *19*(9):1430–1434 May 1980.

28. Utku, S., Kuo, C.P., Garba, J.A. and Wada, B.K. "Shape Control of Inflatable Reflectors," *Journal of Intelligent Material Systems and Structures*, *6* July 1995.

29. Xin, Y. and Xueye, W. "Novel Wavefront Sensor used in Adaptive Optics - Zernike Polynomials Coefficients Sensor," *Adaptive Optics in Astronomy*, *SPIE 2201*:539–548 1994.

30. Bishop, J.A. "Shape Correction of Initially Flat Inflated Membranes by a Genetic Algorithm," *AIAA Paper 98-1984* 1998.

31. Grossman, G. "Tension Element to Reduce Loads in Rim Support of Inflatable Reflector," *Journal of Aerospace Engineering*, *7*(2):129–142 April 1994.

32. Moore, J.D. and Bishop, J.A. "Evaluation of Catenary Suspension for Reducing Shape Errors in Inflated Solar Concentrators," *AIAA Paper 98-1985* 1998.

33. Wilkes, J.M., Jenkins, C.H., Marker, D.K., Carreras, R.A., Duneman, D.C. and Rotgé, J.R. *Concave Membrane Mirrors from Aspheric to Near-Parabolic*. Final Report AFRL-DE-99-463, AFRL, July 1999. AFRL/DE.

34. Greschik, G., Palisoc, A., Cassapakis, C., Veal, G. and Mikulas, M.M. "Sensitivity Study of Precision Pressurized Membrane Reflector Deformations," *AIAA Journal*, *39*(2):308–314 February 2001.

35. Eringen, A.C. "On the Non-Linear Vibration of Elastic Bars," *Quarterly Journal of Applied Mathematics*, *9*(4):361–369 1952.

36. Aravamudan, K.S. and Murthy, P.N. "Non-Linear Vibrations of Beams with Time-Dependent Boundary Conditions," *International Journal of Non-Linear Mechanics*, *8*:195–212 June 1973.

37. Crespo da Silva, M.R.M. and Glynn, C.C. "Non-Linear Flexural-Flexural-Torsional Dynamics of Inextensional Beams I. Equations of Motion," *Journal of Structural Mechanics*, *6*(4):437–448 1978.

38. Crespo da Silva, M.R.M. and Glynn, C.C. "Non-Linear Flexural-Flexural-Torsional Dynamics of Inextensional Beams I. Forced Motions," *Journal of Structural Mechanics*, *6*(4):449–461 1978.

39. Nayfeh, A.H. "Nonlinear transverse vibrations of beams with peoperties that vary along the length," *Journal of the Acoustical Society of America*, *53*(3):766–770 1973.

40. Steele, C.R., Balch, C.D., Jorgensen, G.J., Wendelin, T. and Lewandowski, A. *Membrane Dish Analysis: A Summary of Structural and Optical Analysis Capabilities*. Technical Paper 253-3432, NREL, 1991.

41. Mikulas, M.M. *Behavior of Doubly Curved Partly Wrinkled Membrane Structures Formed from an Initially Flat Membrane*. Dissertation, Virginia Polytechnic Institute, June 1970.

42. Kang, S. and Im, S. "Finite Element Analysis of Wrinkling Membranes," *Journal of Applied Mechanics*, *64*:263–269 June 1997.

43. Wilkes, J.M. *Applications of Power Series Solutions of Membrane Equilibrium Equations to the Optical Evaluation of Membrane Mirrors with Curvature*. Final Report AFRL-DE-PS-TR-1998-1069, AFRL, December 1999.

44. Marker, D.K., Jenkins, C.H. and Schoof, L. *On the Systematic "W" Profile Error in Uncompensated Isotropic Membrane Reflectors (PL 96-1035)*. Final Report AFRL-DE-99-463, AFRL, July 1999. AFRL/DE.

45. Jenkins, C.H., Wilkes, J.M. and Marker, D.K. "Improved Surface Accuracy of Precision Membrane Reflectors through Adaptive Rim Control," *AIAA Paper 98-1983* 1998.

46. Greschik, G., Mikulas, M.M. and Palisoc, A. "Approximations and Errors in Pressurized Axisymmetric Membrane Shape Predictions," *AIAA 39th Structures, Structural Dynamics, and Materials Conference and Adaptive Structures Forum, AIAA 98-2101*:2761–2771 April 20-23 1998.

47. Palisoc, A.L. and Huang, Y. "Design Tool for Inflatable Space Structures," *AIAA Paper 97-1378* 1997.

48. Greschik, G., Palisoc, A. and Mikulas, M.M. "Revisiting Hencky's Problem - Approximations in the Power Series Method," *25th Silver Jubilee Midwest Mechanics Conference* September 21-24 1997.

49. Hencky, H. "Uber den Spannungszustand in kreisrunder Platten mit verschwindender Biegungssteifigkeit," *Zeitschrift f́ur Mathematik und Physik*, *63*:311–317 1915.

50. Mohan, P. and Kapania, R.K. "Geometrically Nonlinear Analysis of Composite Plates and Shells Using a Flat Triangular Shell Element," *AIAA Paper 97-1233* 1997.

51. Karnaukhov, V.G., Kozlov, V.I. and Mikhailenko, V.V. "Finite Element Method in Problems of Thermoelectroviscoelasticity," *Prikladnaya Mekhanika (translated)*, *25*(2):19–28 February 1989.

52. Elsami, M.R., M.Shakeri, Ohadi, A.R. and Shiari, B. "Coupled Thermoelasticity of Shells of Revolution: Effect of Normal Stress and Coupling," *AIAA Journal*, *37*(4):496–504 April 1999.

53. Cady, W.G. *Piezoelectrity* (Revised Edition), *1*. Dover, 1964.

54. Tzou, H.S. and Tseng, C.I. *Distributed Dynamic Identification and Controls of Flexible Shells: Theory and Finite Element Development*. Technical Report AIAA 90-1069-CP, AIAA, 1990.

55. Salama, M., Kuo, C.P., Garba, J., Wada, B. and Thomas, M. "On-orbit Shape Correction of Inflatable Structures," *AIAA Paper 94-1771-CP* 1993.

56. Sun, W. "Modeling of Flexible Piezoelectric Laminates," *Smart Structures and Materials 1993 (Smart Structures and Intelligent Systems)*, *SPIE 1917*(1):497–507 February 1-4 1993.

57. Tzou, H.S. and Tseng, C.I. "Distributed Piezoelectric Sensor/Actuator Design for Dynamic Measurement/Control of Distributed Parameter Systems: A Piezoelectric Finite Element Approach," *Journal of the Sound and Vibration*, *138*(1):17–34 January 1990.

58. Tzou, H.S. and Zhong, J.P. "Electromechanics and Vibrations of Piezoelectric Shell Distributed Systems," *Journal of Vibrations and Acoustics*, *115*:506–517 September 1993.

59. Tzou, H.S. and Howard, R.V. "A Piezothermoelastic This Shell Theory Applied to Active Structures," *Journal of Vibrations and Acoustics*, *116*:295–302 July 1994.

60. Tzou, H.S., Bao, Y. and Ye, R. "A Theory on nonlinear piezothermoelastic shell laminates," *Smart Structures and Materials 1994 (Smart Structures and Intelligent Systems)*, *SPIE 2190*:206–214 February 14-16 1994.

61. Berdichevsky, V.L. "Variational-Asymptotic Method of Constructing a Theory of Shells," *PMM*, *43*(4):664–687 1979.

62. Cesnik, C.E.S., Sutyrin, V.G. and Hodges, D.H. "A Refined Composite Beam Theory Based on the Variational-Asymptotic Method," *AIAA Paper 93-1616-CP, AIAA 34th Structures, Structural Dynamics, and Materials Conference and Adaptive Structures Forum, Seattle, Washington*, 2710–2720 April 19-22 1993.

63. Cesnik, C.E.S. and Hodges, D.H. "Variational-Asymptotic Analysis of Initially Curved and Twisted Composite beams," *Mechanics Pan-America*, *46*(11):S211–S220 November 1993.

64. Lee, B.K., Sutyrin, V.G. and Hodges, D.H. "A Variable-Order Laminated Plate Theory Based on the Variational-Asymptotic Method," *AIAA 34th Structures, Structural Dynamics, and Materials Conference and Adaptive Structures Forum*, 2721–2732 April 19-22 1993.

65. Cook, R.D., Malkus, D.S. and Plesha, M.E. *Concepts and Applications of Finite Element Analysis*. John Wiley & Sons Inc., 1974.

66. Nayfeh, A.H. and Mook, D.T. *Nonlinear Oscillations*. John Wiley & Sons Inc., 1979.

67. Nayfeh, A.H. *Introduction to Perturbation Techniques*. John Wiley & Sons Inc., 1981.

68. Saada, A.S. *Elasticity Theory and Applications* (Second Edition). Krieger Publishing Company, 1993.

69. Nayfeh, A.H. *Problems in Perturbation*. John Wiley & Sons Inc., 1993.

70. Meirovitch, L. *Principles and Techniques of Vibrations*. Prentice Hall, 1997.

71. Malacara, D., Servín, M. and Malacara, Z. *Interferogram Analysis for Optical Testing*. Marcel Dekker, Inc., 1998.

Vita

Captain James W. Rogers Jr. was born in Denver, Colorado. He graduation from Regis Jesuit High School in 1980, enlisted in the United Stated Air Force in 1983 as an computer and electronics switching systems specialist and served one tour of duty at the PAVE PAWS early warning radar system at Beale AFB, California.

Selected for the Airmen's Education and Commissioning Program in 1987, he attended The Ohio State University in Columbus Ohio where graduated Cum Laude in 1990 with Bachelor Degrees in Aeronautical and Astronautical Engineering as well as Computer and Information Science before attending Officer Training School.

He was commissioned a second lieutenant in the United Stated Air Force in October 1990 and assigned to the 1st Satellite Control Squadron in support of the Global Positioning System (GPS) launch and anomaly resolution mission at Schriever AFB, Colorado where he served as a Planning and Analysis Officer, Crew Commander and Lead Engineer. In 1992 he was assigned to the 4th Space Operations Squadron at Schriever AFB to stand up the new Milstar mission support squadron where he served as Payload and Lead Engineer as well as Evaluator. During these assignments, he earned a Master's Degree in Aerospace Engineering from the University of Colorado.

In 1995 he attended the United Stated Air Force Test Pilot School at Edwards AFB, California and graduated with Class 95A. He was subsequently assigned to the 419th Flight Test Squadron at Edwards AFB as a B-1B/B-52H Flight Test Engineer, serving as Lead Test Conductor, Lead Test Director, Unit Test Safety Officer, Chief, Operations Engineering, and B-1B/UAV Flight Commander.

In 1998, he began the Doctor of Philosophy Degree program at the Air Force Institute of Technology. Upon graduation, he will be assigned to the Air Vehicles Directorate of the Air Force Research Laboratory at Wright-Patterson AFB, Ohio.

www.manaraa.com

NONPRINT FORM

1. Type of Product: CD-ROM	2. Operating System/Version: Windows 2000 Professional	3. New Product or Replacement: New	4. Type of File: Text

5. Language/Utility Program:
Matlab v6
Mathematica v4.1
MathCAD 2001
LaTeX 2e

6. # of Files/# of Products: 753/1	7. Character Set: Other:Both	8. Disk Capacity: 650 MB
	9. Compatibility: PC	10. Disk Size: CD-ROM

11. Title:
Modeling Axisymmetric Optical Precision Peizoelectric Membranes
(Dissertation+Worksheets+Code)(U)

12. Performing Organization:	13. Performing Report #: AFIT-DS-ENY-01-02	14. Contract #:
		15. Program Element #:

16. Sponsor/Monitor:	17. Sponsor/Monitor # Acronym: AFIT	19. Project #:
	18. Sponsor/Monitor #:	20. Task #:
		21. Work Unit #:

22. Date: October, 2001	23. Classification of Product: Unclassified
24. Security Classification Authority:	25. Declassification/Downgrade Schedule:

26. Distribution/Availability:
A   Approved for public release; distribution is unlimited.

Security Classification of this Page: **UNCLASSIFIED**

27. Abstract:
A laminate of piezoelectric polymer material can deform a membrane optical surface; however, modeling this system must be improved. Analytic solutions to the beam and axisymmetric membrane models are produced providing insight into resulting behavior of these materials. Based on these results a new mathematical methodology rooted in fundamental perturbation techniques was developed: The Method of Integral Multiple Scales (MIMS). MIMS allows selectable precision when applied to a special class of dynamic systems which can be represented through a Lagrangian. The method is able to integrate spatial and temporal multiple scales directly producing boundary layer solutions. This method is fully realized through the finite element approach and applied to nonlinear beam and axisymmetric circular membrane models.

28. Classification of Abstract:
Unclassified

29. Limitation of Abstract:
Unclassified Unlimited

30. Subject Terms:
Piezoelectricity;
Finite Element Analysis;
Asymptotic Series;
Deformable Mirrors;
Inflatable Structures (U)

30a. Classification of Subject Terms:
Unclassified

31. Required Peripherals:

32. # of Physical Records:

33. # of Logical Records:

34. # of Tracks:

35. Record Type:

36. Color:
Mixed

37. Recording System:

38. Recording Density:

39. Parity:

40. Playtime:

41. Playback Speed:

42. Video:
Yes

43. Text:
Yes

44. Still Photos:
Yes

45. Audio:
No

46. Other:

47. Documentation/Supplemental Information:

48. Point of Contact and Telephone Number:
Capt. James W. Rogers Jr.
2950 P St, Bldg 640
(937) 255-3636
jrogers@afit.edu

DTIC FORM 530   JUN 94   Security Classification of this Page: **UNCLASSIFIED**

1. REPORT DATE *(DD-MM-YYYY)* 29-10-2001	2. REPORT TYPE Doctoral Dissertation	3. DATES COVERED *(From - To)* Jan 2000-Oct 2001

4. TITLE AND SUBTITLE
Modeling Axisymmetric Optical Precision Piezoelectric Membranes

5a. CONTRACT NUMBER

5b. GRANT NUMBER

5c. PROGRAM ELEMENT NUMBER

6. AUTHOR(S)
Rogers, James, W., Jr., Captain, USAF

5d. PROJECT NUMBER
2001-003

5e. TASK NUMBER

5f. WORK UNIT NUMBER

7. PERFORMING ORGANIZATION NAME(S) AND ADDRESS(ES)
Air Force Institute of Technology
Graduate School of Engineering and Management (AFIT/EN)
2950 P Street, Building 640
WPAFB OH 45433-7765

8. PERFORMING ORGANIZATION REPORT NUMBER
AFIT/DS/ENY/01-02

9. SPONSORING/MONITORING AGENCY NAME(S) AND ADDRESS(ES)
AFOSR/NA
Attn: Mr. Daniel Segalman
801 N. Randolph St., Mailroom 732
Arlington VA 22203-1977

Phone: (703) 696-7259

10. SPONSOR/MONITOR'S ACRONYM(S)

11. SPONSOR/MONITOR'S REPORT NUMBER(S)

12. DISTRIBUTION/AVAILABILITY STATEMENT
APPROVED FOR PUBLIC RELEASE; DISTRIBUTION UNLIMITED

13. SUPPLEMENTARY NOTES

14. ABSTRACT
A laminate of piezoelectric polymer material can deform a membrane optical surface; however, modeling this system must be improved. Analytic solutions to the beam and axisymmetric membrane models are produced providing insight into resulting behavior of these materials. Based on these results a new mathematical methodology rooted in fundamental perturbation techniques was developed: The Method of Integral Multiple Scales (MIMS).
MIMS allows selectable precision when applied to a special class of dynamic systems which can be represented through a Lagrangian. This new method was first applied to a relatively simple linear beam problem for the purpose of illustration. The method is able to integrate spatial and temporal multiple scales directly producing boundary layer solutions. This method is fully realized through the finite element approach, where the solution was shown to be over three orders of magnitude more accurate than a standard finite element result. The finite element methodology is applied to nonlinear beam and axisymmetric circular membrane models producing insight for future design decisions. The results illustrate the capability of such an active membrane to modify a reflected wavefront and provide control for an inflatable optical reflector.

15. SUBJECT TERMS
Piezoelectricity, Finite Element Analysis, Asymptotic Series, Deformable Mirrors, Inflatable Structures

16. SECURITY CLASSIFICATION OF:			17. LIMITATION OF ABSTRACT	18. NUMBER OF PAGES	19a. NAME OF RESPONSIBLE PERSON
a. REPORT	b. ABSTRACT	c. THIS PAGE			Major Gregory S. Agnes, ENY
U	U	U	UU	188	19b. TELEPHONE NUMBER *(Include area code)* (937) 255-3636, ext. 4317

Standard Form 298 (Rev. 8/98)
Prescribed by ANSI Std. Z39.18